République Algérienne Démocratique et Populaire
Ministère de l'Enseignement Supérieur et de la Recherche Scientifique
Université 8 Mai 1945 Guelma

Faculté des Sciences et de la Technologie
Département de Génie des Procédés
Laboratoire des Silicates, Polymères et Nanocomposites (LSPN)

THÈSE

EN VUE DE L'OBTENTION DU DIPLOME DE DOCTORAT EN 3ème CYCLE

Domaine : Sciences et Technologie Filière : Génie des Procédés

Spécialité : Génie des Matériaux

Présentée par

TAIBI Ahmed

Intitulée

Elaboration and Characterization of Perovskite Piezoelectric Ceramics: $Ba_{(1-x)}Ca_xTiO_3$ and $(1-y)BiFeO_3$-$yBaTiO_3$

Soutenue le 12/07/2022 Devant le Jury composé de :

Mr AFFOUNE Abed Mohamed	Professeur	Univ. 8 Mai 1945 Guelma	Président
Mr CHAGHETMI Salem	Professeur	Univ. 8 Mai 1945 Guelma	Encadreur
Mr SATHA Hamid	Professeur	Univ. 8 Mai 1945 Guelma	Co-encadreur
Mr MERAZIG Hocine	Professeur	Univ. Constantine 1	Examinateur
Mr BOUDAREN Chawki	Professeur	Univ. Constantine 1	Examinateur
Mr BOUDINE Boubekeur	Professeur	Univ. Constantine 1	Examinateur

Année Universitaire : 2021/2022

الحمد لله كما ينبغي لجلال وجهه وعظيم سلطانه

Dedication

***To** my Parents for their unconditional love and encouragement all the way.*

***To** my Grandmother for her precious prayers and constant care.*

***To** my Wife for her love and faith in me.*

***To** my dear Siblings and Friends.*

Acknowledgements

In light of this work, I would first like to thank **Allah Almighty** for all the wonders He does in my life and for giving me courage, strength, and most importantly, patience to complete this modest scientific contribution.

I would like to express my gratitude to my thesis supervisor, **Prof. CHAGUETMI Salem**, for providing guidance and feedback throughout this research. I would also like to thank my thesis co-supervisor, **Prof. SATHA Hamid,** for his useful suggestions and supervision.

I wish to acknowledge the help provided by the technical and support staff at the **Process Engineering Department of the University of Guelma**. I also express my sincere thanks to all the **LSPN laboratory staff**, especially to **Dr. LAYACHI Abdelheq**, **Dr. LOUAER Ali** and **Dr. MAKHLOUF Azzedine** for their kind and constant support.

I am deeply thankful to **Prof. PÉREZ-MAQUEDA Luis Allan** of the **Institute of Materials Science of Seville** (**ICMS**) for offering deep insight into this work with his immense knowledge and plentiful experience.

I would like to sincerely thank all the members of the group "**Reactividad de Solidos**" of the **Institute of Materials Science of Seville** (**ICMS**) for their valuable contribution and assistance at every stage of this research project, as well as for their friendly attitude.

I am very grateful to the **Ministry of Higher Education and Scientific Research** (**MESRS**) for the PhD scholarship, without which this work would not have been possible, to cover all my study and living expenses in Seville, Spain.

I would like to express my thanks to **Prof. AFFOUNE Abed Mohamed** for having accepted to chair the defense jury. I would also like to express my deep gratitude to the members of the jury: **Prof. MERAZIG Hocine**, **Prof. BOUDAREN Chawki** and **Prof. BOUDINE Boubekeur**, for having accepted to examine this modest work.

Thanks to all who helped me in any way during these years of research and study.

I cannot conclude without thanking all my **Teachers, Professors and Colleagues**.

Abstract

The Pb-free piezoceramics are currently considered as an alternative to Pb-based ceramics due to the harmful effects of lead on the environment and human health. In this thesis, two families of Pb-free piezoelectric ceramics were studied, including $Ba_{(1-x)}Ca_xTiO_3$ (BCT) and (1-y)$BiFeO_3$-y$BaTiO_3$ (BFO-BT).

In the first part, the incorporation mechanism of Ca into $BaTiO_3$ were investigated using differential scanning calorimetry (DSC) technique at multiple heating rates. The DSC and the X-ray diffraction technique (XRD) has demonstrated the complete incorporation of Ca into $BaTiO_3$ structure. Incorporation kinetics was analyzed by Freidman (FR), Ozawa-Flynn-Wall (OFW) and Kissinger-Akahira-Sunose (KAS) isoconversional methods. The results indicate that the incorporation process was carried out through a single-step. The kinetic parameters, i.e. Activation energy (E_a), preexponential factor (A) and the kinetic model ($f(\alpha)$), were determined through the combined kinetic analysis method. The BCT ceramic samples were then synthesized using the conventional solid-state reaction method in order to study the effect of Ca doping on the structural, microstructural and electrical properties of $BaTiO_3$. Different characterization techniques, such as XRD, Raman, SEM and electrical measurements, were used in order to study the influence of Ca on the properties of $BaTiO_3$.

In the second part, the (1-y)$BiFeO_3$-y$BaTiO_3$ (BFO-BT) ferroelectric ceramic was prepared by Reactive Flash Sintering (RFS). This preparation technique combines synthesis and sintering in a single Flash experiment. The starting oxides reacted during the flash to produce a stoichiometric well-sintered solid solution at a temperature of 858 °C by applying a modest field of 35 V cm^{-1}. The process takes place in a matter of seconds, which allows obtaining a pure perovskite structure without secondary phases. X-ray diffraction (XRD) results show the mixture of rhombohedral and pseudocubic phases expected for a composition that lies within a morphotropic phase boundary (MPB) region. The microstructure exhibits a peculiar bimodal grain size distribution that determines the electrical properties. As compared to previous results, flash-prepared 0.67$BiFeO_3$-0.33$BaTiO_3$ (BFO-33BT) evidences smaller grain size as well as slightly lower remanent polarization (P_r) and smaller coercive field (E_c) under similar electric fields. It is also demonstrated that the preparation by RFS provides benefits regarding electrical energy consumption.

Keywords: Piezoelectric ceramics, $BaTiO_3$, Incorporation mechanism, Solid-state reaction, Kinetic parameters, $BiFeO_3$-$BaTiO_3$, Flash sintering.

Résumé

Les céramiques piézoélectriques sans plomb sont actuellement considérées comme une alternative aux céramiques à base de Plomb en raison des effets nocifs du plomb sur l'environnement et la santé humaine. Dans cette thèse, deux familles de céramiques piézoélectriques sans Plomb ont été étudiées, notamment $Ba_{(1-x)}Ca_xTiO_3$ (BCT) et (1-y)$BiFeO_3$-y$BaTiO_3$ (BFO-BT).

Dans la première partie, le mécanisme d'incorporation du Ca dans le $BaTiO_3$ a été étudié en utilisant l'analyse calorimétrique différentielle (DSC) à plusieurs vitesses de chauffage. La technique DSC et la technique de diffraction des rayons X (DRX) ont démontré l'incorporation complète du Ca dans la structure du $BaTiO_3$. La cinétique d'incorporation a été analysée par les méthodes isoconversionnelles de Freidman (Fr), Ozawa-Flynn-Wall (OFW) et Kissinger-Akahira-Sunose (KAS). Les résultats indiquent que le processus d'incorporation s'est déroulé en une seule étape. Les paramètres cinétiques, à savoir l'énergie d'activation (E_a), le facteur pré-exponentiel (A) et le modèle cinétique (f(α)), ont été déterminés par la méthode d'analyse cinétique combinée. Les échantillons de céramique BCT ont ensuite été synthétisés en utilisant la méthode de préparation conventionnelle à l'état solide afin d'étudier l'effet du dopage au Ca sur les propriétés structurelles, microstructurales et électriques du $BaTiO_3$. Différentes techniques de caractérisation, telles que DRX, Raman, Microscope Electronique à Balayage (MEB) et les mesures électriques, ont été utilisées afin d'étudier l'influence du dopage par Ca sur les propriétés du $BaTiO_3$.

Dans la deuxième partie, la céramique piézoélectrique (1-y)$BiFeO_3$-y$BaTiO_3$ (BFO-BT) a été préparée par Frittage Flash Réactif (RFS). Cette technique de préparation combine la synthèse et le frittage dans une seule expérience Flash. Les oxydes de départ ont réagi pendant le flash pour produire une solution solide stœchiométrique bien frittée à une température de 858 °C en appliquant un champ modeste de 35 V cm^{-1}. Le processus se déroule en quelques secondes, ce qui permet d'obtenir une structure pérovskite pure sans phases secondaires. Les résultats de la diffraction des rayons X (XRD) montrent un mélange de deux phases, rhomboédriques et pseudocubiques, attendu pour une composition qui se trouve dans la zone morphotropique. La microstructure présente une distribution bimodale particulière de la taille des grains qui détermine les propriétés électriques. En comparaison avec les résultats précédents, le 0,67$BiFeO_3$-0,33$BaTiO_3$ (BFO-33BT) préparé par flash présente une taille de grain plus petite, ainsi qu'une polarisation rémanente (P_r) légèrement inférieure et un champ coercitif (E_c) plus faible sous des champs électriques similaires. Il a été également démontré que la préparation par RFS présente des avantages en matière de consommation d'énergie électrique.

Mots clés : Céramiques piézoélectriques, $BaTiO_3$, Mécanisme d'incorporation, Réaction à l'état solide, Paramètres cinétiques, $BiFeO_3$-$BaTiO_3$, Frittage flash.

الملخص

حاليا يعتبر السيراميك الكهروضغطي الخالي من الرصاص بديلاً للسيراميك الذي يحتوي على الرصاص بسبب الآثار الضارة للرصاص على البيئة وعلى صحة الإنسان. في هذه الأطروحة، تمت دراسة عائلتين من السيراميك الكهروضغطي الخالي من الرصاص، على وجه الخصوص $Ba_{(1-x)}Ca_xTiO_3$ (BCT) و $(1-y)BiFeO_3$-$yBaTiO_3$ (BFO-BT).

في الجزء الأول من الاطروحة، تمت دراسة آلية دمج الكالسيوم في $BaTiO_3$ باستخدام المسعر الحراري التفاضلي (DSC) بسرعات تسخين متعددة. أظهرت تقنية DSC وتقنية حيود الأشعة السينية (XRD) الإدماج الكامل للكالسيوم في $BaTiO_3$. تم تحليل حركيات التأسيس من خلال الطرق المتساوية لكل من Freidman (FR) ، Ozawa-Flynn-Wall (OFW) و Kissinger-Akahira-Sunose (KAS). تشير النتائج إلى أن عملية الدمج تمت في خطوة واحدة. تم تحديد المعلمات الحركية، وهي طاقة التنشيط (Ea)، والمعامل الأسي (A) والنموذج الحركي ($f(\alpha)$)، من خلال طريقة التحليل الحركي المشترك. تم بعد ذلك تصنيع عينات السيراميك BCT باستخدام طريقة التفاعل في الحالة الصلبة لدراسة تأثير دمج Ca على الخصائص التركيبية، البنية الدقيقة والكهربائية لـ $BaTiO_3$. تم استخدام تقنيات معاينة مختلفة، مثل DRX ومطياف رامان Raman spectroscopy والمكروسكوب الالكتروني (SEM) والقياسات الكهربائية، لدراسة تأثير دمج Ca على خصائص $BaTiO_3$.

في الجزء الثاني من الاطروحة، تم دراسة تحضير السيراميك الكهرضغطي ذو الصيغة $(1-y)BiFeO_3$-$yBaTiO_3$ (BFO-BT) بواسطة تقنية تكثيف الفلاش التفاعلي (RFS). تجمع تقنية التحضير هذه بين التفاعل والتكثيف في تجربة فلاش واحدة. تفاعلت المركبات الاولية أثناء الوميض لإنتاج سيراميك صلب متكافئ جيد التكلس عند درجة حرارة 858 درجة مئوية عن طريق تطبيق توتر كهربائي متواضع في حدود $35\ V\ cm^{-1}$. تتم العملية في ثوانٍ، مما ينتج عنه بنية بيروفسكايت نقية. تُظهر نتائج حيود الأشعة السينية (XRD) مزيجًا من مرحلتين، معينية الوجوه Rhombohedral وشبه مكعبة Pseudocubic، مثلما كان متوقعا في البداية. تعرض البنية المجهرية توزيعًا ثنائي النسق لحجم الحبوب والذي يحدد الخصائص الكهربائية. بالمقارنة مع النتائج السابقة، التحضير بواسطة RFS ينتج عنه حجم حبيبات أصغر، بالإضافة إلى الاستقطاب Pr منخفض قليلاً والمجال القسري E_c أصغر تحت توترات كهربائية مماثلة. كما تبين أن التحضير بواسطة RFS له مزايا من حيث استهلاك الطاقة الكهربائية.

كلمات مفتاحية: سيراميك كهرضغطي، $BaTiO_3$، آلية التأسيس، تفاعل الحالة الصلبة، المعلمات الحركية، $BiFeO_3$-$BaTiO_3$، تلبيد فلاش

Table of Contents

Chapter II. Experimental procedures and characterization techniques

Chapter III. Study of the Incorporation Mechanism of Ca into $BaTiO_3$

Chapter IV. Structural, Microstructural and Electrical Properties of BCT Piezoelectric Ceramics

Nomenclature and Acronyms

a	*Lattice constant length (Å)*
A	*Pre-exponential factor (S^{-1})*
b	*Lattice constant length (Å)*
BCT	*Barium calcium titanate*
BCZT	*Barium calcium zirconate titanate*
BT	*Barium titanate*
BFO-BT	*$BiFeO_3$-$BaTiO_3$*
BZT	*Barium zirconate titanate*
c	*Lattice constant length (Å)*
C	*Capacitance (F)*
CM	*Conventional method*
d_{33}	*Piezoelectric charge coefficient*
DSC	*Differential scanning calorimetry*
E	*Electric field ($V\ m^{-1}$)*
E_a	*Activation energy ($j\ mol^{-1}$)*
E_c	*Coercive field ($V\ m^{-1}$)*
ECAS	*Elctric current assisted sintering*
ε'	*Dielectric constant*
ε_0	*Vacuum permittivity ($F\ m^{-1}$)*
ε_r	*Relative permittivity*
EDS	*Energy-dispersive X-ray spectroscopy*
FR	*Friedman*
I	*Current intensity (A)*
KAS	*Kissinger-Akahira-Sunose*
KNN	*$(K_{0.5}Na_{0.5})NbO_3$*
MPB	*Morphotropic phase boundary*
NBT	*$(Na_{1/2}Bi_{1/2})TiO_3$*
OFW	*Ozawa-Flynn-Wall*
PC	*Pseudo-cubic*
P_r	*Remanent polarization ($C\ m^{-2}$)*
PVA	*Polyvinyl alcohol*
PZT	*Lead zirconate titanate*
R	*Universal gas constant ($J\ K^{-1}mol^{-1}$)*
SEM	*Scanning electron microscopy*
T	*Temperature (°C or K)*
tanδ	*Dielectric loss*
RFS	*Reactive Flash Sintering*
T_c	*Curie temperature (°C or K)*
TGA	*Thermogravimetric analysis*
XRD	*X-ray diffraction*

List of Tables

List of Figures

General Introduction

Piezoelectric ceramics (also known as piezoceramics) are used in a variety of applications including transducers, actuators, sensors, multilayer capacitors, and ferroelectric memory devices (**Berlincourt, 1998**). Some piezoelectric perovskite materials with the general chemical formula $PbZr_{1-x}Ti_xO_3$ (PZT) are widely used today due to their high piezoelectric properties and Curie temperature (T_c ~ 400 °C), that allows their effective use at very high temperatures. Furthermore, PZTs are simple to process using traditional ceramic processes (solid-state reaction, conventional sintering), making it possible to manufacture and produce large pieces in a short period of time and at a low cost (if, for example, the control of partial volatilization of lead is ignored during high-temperature sintering). PZTs have various uses since they are relatively easy to manufacture and quite adjustable in terms of usage features due to multiple doping possibilities and sintering aids (**Tiwari, Babu and Choudhary, 2021**).

However, the toxic nature of lead (Pb) is a major concern during lead mining as well as during lead product manufacturing, use, and disposal (**Bell and Deubzer, 2018**). Lead is a cumulative toxin that is generally harmful to human health and therefore can affect a variety of human physiological systems. Lead is found in all parts of the body including the bones, brain, kidneys, and liver. It is stored in bones and teeth where it accumulates over time. Further to that, inflammation is considered to be one of the primary processes causing lead's harmful effects on the respiratory, cardiovascular, neurological, digestive, and urinary systems (**Boskabady *et al.*, 2018**). From the foregoing, it is clear that the use of lead in the production of piezoelectric ceramics has significant impacts on the environment and human health. As a result, many legislations (**Bell and Deubzer, 2018**) such as REACH (Registration, Evaluation, Authorization and Restriction of Chemicals) and RoHS (Restriction of Use of Certain Hazardous Substances) have been introduced in order to reduce the amount of lead used in electronic devices, creating a strong incentive to develop lead-free piezoceramic.

In the past two decades, researchers focused on Pb-free piezoceramics based on $BaTiO_3$ (BT) and $BiFeO_3$ (BFO) with the aim of improving their properties, understanding the mechanism of their formation and looking for new energy-efficient processing methods in order to prepare such materials (**Wu, 2020**). Each of these Pb-free piezoceramics has strengths and weaknesses. Pure BT generally presents a high dielectric constant but exhibits low Curie temperature (T_c ~120 °C) and low piezoelectric coefficient (d_{33} ~ 190 pC/N). Doped BT ceramics is a potential tunable material with improved piezoelectric and ferroelectric properties that could be a suitable alternative for PZT (**Acosta *et al.*, 2017**).

On the other hand, Pure BFO has a very high Curie temperature (T_c ~ 830 °C) as well as an attractive polarization (P_s ~ 100 μC/cm^2) but the high leakage current and the difficulty of preparation caused by its very narrow thermal stability range, limit its practical applications in devices. Doping is an effective strategy to improve the electrical properties and to increase the stability of BFO (**Wu *et al.*, 2016**).

Among the BT based piezoceramics, The pseudobinary ceramic composition $xBa_{0.7}Ca_{0.3}TiO_3$-$(1-x)BaTi_{0.8}Zr_{0.2}O_3$ (named BCT-BZT or BCZT) has been reported to reach high piezoelectric coefficient value (d_{33}~ 620 pC/N) when x=0.5 due to the presence of a MPB (**Liu and Ren, 2009**). BCZT can be prepared by mixing $Ba_{1-y}Ca_yTiO_3$ (BCT) and $BaTi_{1-z}Zr_zO_3$ (BZT) in the solid-state, which requires substitution of Ca and Zr at the Ba and Ti-site, respectively. BCT is also an interesting piezoceramic (d_{33}=180-310 pC/N) because of structural changes caused by Ca substitution in $BaTiO_3$ (**Fu *et al.*, 2008**). Therefore, a detailed understanding of the mechanism of Ca incorporation into $BaTiO_3$ in the solid-state reaction is required to allow an in-depth study of the preparation and properties of the BCT and BCZT piezoceramics.

Regarding the BFO-based piezoceramics, $BiFeO_3$-$BaTiO_3$ (BFO-BT) based materials are potential candidates for high temperature applications, with some authors reporting good piezoelectric characteristics and high temperature reliability (**Zhou *et al.*, 2012; Wei *et al.*, 2013; Wang *et al.*, 2019; Chen *et al.*, 2020; Xun *et al.*, 2021**). BFO-BT ceramics are considered to have a MPB like PZT. However, some different crystal structure results have been reported, implying that different factors such as dopants, sintering conditions, quenching, and processing methods influence the assembly of the phase (**Wang *et al.*, 2018**). Dense BFO-BT piezoceramics are synthesized in two steps, including preparation and sintering of BFO-BT powders. Both steps need high temperatures and long treatment times, which are high energy consuming. Under such conditions, it is difficult to prepare dense and stoichiometric BFO-BT ceramics due to high Bi volatilization and Fe^{3+} reduction that lead to the formation of impurities such as $Bi_2Fe_4O_9$, $Bi_{25}FeO_{39}$, or Bi_2O_3 (**Pabst *et al.*, 2007; Zheng *et al.*, 2014; Cheng *et al.*, 2018; Xun *et al.*, 2021**). Thus, other techniques to prepare dense and stoichiometric BFO-BT ceramics are required.

The framework of this thesis is therefore situated in the context presented above, where most of the research on piezoceramics is turned towards the study of Pb-free materials. This project focuses on two interesting Pb-free piezoceramics: $BaTiO_3$ and $BiFeO_3$-based materials.

The objectives of this thesis revolve around two main axes. The first focuses on the kinetics analysis of Ca incorporation into $BaTiO_3$ using Differential Scanning Calorimetry (DSC) as well as studying the effect of Ca substitution on the structural, microstructural, and electrical properties of $Ba_{(1-x)}Ca_xTiO_3$ (BCT). The second axis focuses on the synthesis and densification of $(1-y)BiFeO_3$-$yBaTiO_3$ (abbreviated as BFO-BT) ceramics in a single step using Reactive Flash Sintering (RFS).

This manuscript consists of 5 chapters:

- **In the first chapter** (**Chapter I**), a brief review of piezoelectric materials with perovskite structure is presented. The two sintering techniques used in this work are detailed. The last part of this chapter is devoted to the description of the theoretical basis of the kinetics of the solid-state reaction using DSC.

- **Chapter II** deals with the different experimental procedures and characterization techniques used in this study.

- **The third chapter** (**Chapter III**) focuses on solid-state kinetic analysis of Ca incorporation into $BaTiO_3$ using the DSC technique. The kinetic parameters are determined and tested successfully using the different kinetic methods.

- **Chapter IV** investigates the effect of Ca doping on the structural, microstructural and electrical properties of BCT ceramics.

- **The last chapter** (**Chapter V**) deals with the preparation of $0.67BiFeO_3$-$0.33BaTiO_3$ (BFO-33BT) piezoelectric ceramic by Reactive Flash Sintering (RFS) for the first time. The adjustment of the experimental flash conditions as well as the study of the structural, microstructural and electrical properties of the optimal flash sample are also covered in this chapter.

Chapter I

Literature Review

I.1. Introduction

In this chapter, an introduction is given to the theoretical backgrounds on ferroelectric and piezoelectric materials and their sintering techniques. The theoretical fundamentals of the kinetic analysis of solid-state reactions are also presented in this chapter.

I.2. Fundamentals of Ferroelectrics

I.2.1. Dielectrics

A dielectric is an electrical insulator or a non-conductive of electricity. When an electric field is applied to an insulating medium, positive charges are moved in the direction of the electric field while negative charges are pushed in the opposite direction, resulting in polarization. The polarization of a dielectric substance,$\vec{P}$ is proportional to the strength of the electric field, $\vec{E}$ and can be calculated as follows:

$$\vec{P} = \varepsilon_0 \chi_e \vec{E} \quad \text{(I.1)}$$

where χ_e denotes dielectric susceptibility and ε_0 denotes vacuum permittivity ($\varepsilon_0 = 8.84 * 10^{-12}$ F m^{-1}).

A medium's susceptibility is proportional to its relative permittivity ε_r, which is written as:

$$\varepsilon_r = 1 + \chi_e \quad \text{(I.2)}$$

The entire surface charge density is caused by the applied electric field in the material and it is calculated using the dielectric displacement given as:

$$\vec{D} = \varepsilon_0 \vec{E} + \vec{P} = \varepsilon_0 (1 + \chi_e) \vec{E} = \varepsilon_0 \varepsilon_r \vec{E} \quad \text{(I.3)}$$

When an atom is subjected to a time-harmonic electric field, the relative permittivity of the medium is defined by a complex frequency-dependent quantity defined as:

$$\varepsilon_r(\omega) = \varepsilon_r'(\omega) - j\varepsilon_r''(\omega) \quad \text{(I.4)}$$

where ε_r' denotes the real part, also known as the dielectric constant. ε_r'' is the imaginary part, refers to the dielectric loss factor. The loss tangent (tanδ) is represented by the ratio $\varepsilon_r''/\varepsilon_r'$.

I.2.2. Piezoelectricity

The piezoelectric effect is the result of an electromechanical coupling, i.e., an interdependence of electrical and mechanical properties in the material considered. A deformation under mechanical stress of a piezoelectric material result in the appearance of an electrical potential difference, and conversely, the application of a voltage causes the deformation of the material (**Figure I.1**).

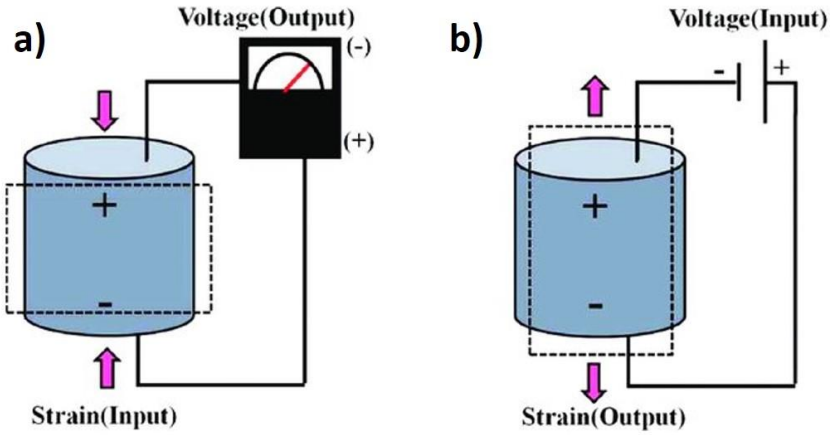

Figure I.1. Piezoelectric effects: a) direct and b) converse.

The phenomenon of piezoelectricity results from a coupling between electrical quantities such as the electric field $\vec{E}$ and the electric displacement $\vec{D}$ and mechanical quantities such as the tensors of stress T and strain S. The relations of proportionality that link them, in the case of an isotropic material, can be written in a simplified way:

For the direct effect: $D_i = d_{ikl}T_{kl}$ (I.5)

For the converse effect: $S_{ij} = d_{kij}E_k$ (I.6)

Following these two relationships, linear constitutive equations of piezoelectricity are given:

$$\begin{cases} D_i = d_{ikl}T_{kl} + \varepsilon_{ik}^{T}E_k \\ S_{ij} = S_{ijkl}^{E}T_{kl} + d_{kij}E_k \end{cases} \quad \text{(I.7)}$$

Not all crystals have the necessary characteristics to exhibit piezoelectric properties. The first condition is to be an electrical insulator, so that there is no moving charge at the macroscopic scale that could compensate for the displacement of charges by distortion of the crystal lattice. The crystallographic structure should not have a center of symmetry. At the atomic scale, the piezoelectricity arises from a differentiation between the barycenter of positive and negative charges (**Figure I.2**), which is impossible in the case of a centrosymmetric structure.

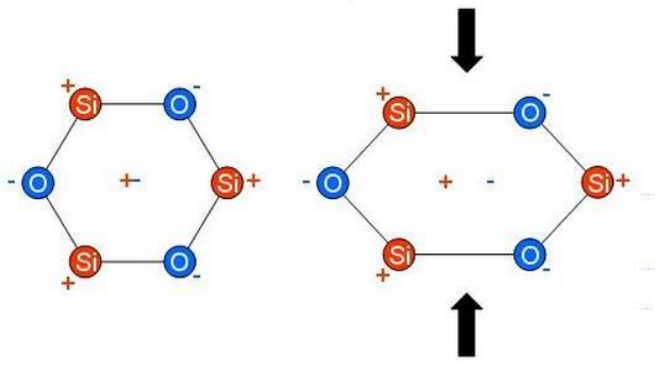

Figure I.2. Piezoelectric effect at the atomic scale in the case of quartz.

Among the 32 existing crystalline classes, 21 are non-centrosymmetric, 20 of which demonstrate a piezoelectric character (**Figure I.3**). Of these 20 classes, 10 are said to be pyroelectric, i.e. they have a spontaneous polarization that varies with temperature.

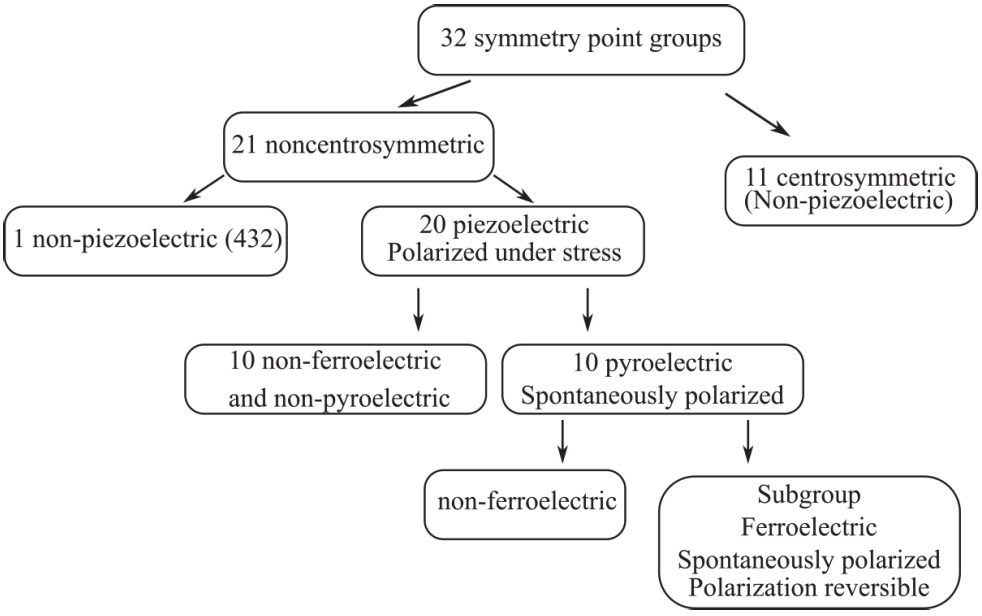

Figure I.3. Distribution of crystalline classes according to certain properties of materials.

I.2.3. Ferroelectricity

The ferroelectric materials are the last particular subcategory of pyroelectric materials. In ferroelectrics, the polarization direction can be reversed under the effect of an external electric field (**Rabe *et al.*, 2007**). These materials can be recognized by the appearance of a hysteresis loop during a voltage sweep (**Figure I.4**). This phenomenon is explained by local polarization fluctuations within the crystal lattice.

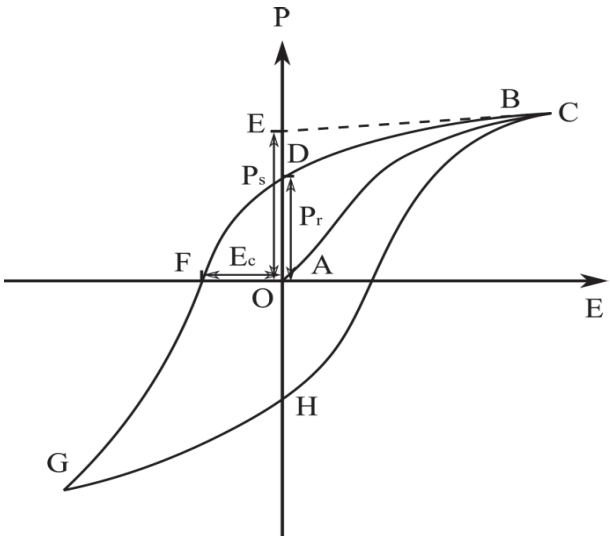

Figure I.4. Hysteresis cycle of a ferroelectric material (**Rabe *et al.*, 2007**).

In the ferroelectric state, the unit cell is not perfect but slightly deformed. This distortion is at the origin of the appearance of dipoles by shifting the barycenter of the positive and negative charges (**Figure I.5**), creating a global polarization of the unit cell. The distortion of the unit cell can only be done along particular directions, resulting in specific polarization directions.

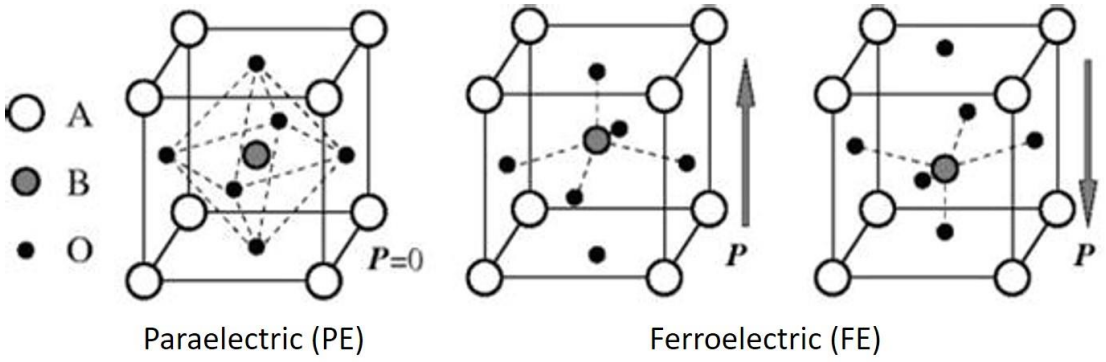

Figure I.5. Paraelectric (PE) and ferroelectric (FE) phases in perovskites (**Rabe *et al.*, 2007**).

Within the same crystallite, not all the dipoles are oriented in the same direction but they are distributed in polarization zones, called ferroelectric domains, separated by domain walls. In the case of a crystallite that has not been subjected to any external electric field, during and since its formation, the random orientation of the domains gives it a zero global polarization ($P_r = 0$) (**Figure I.6 (a)**). When a ferroelectric crystallite is subjected to an electric field, the domain walls move. The domains oriented in the direction of the field expand at the expense of the others (**Figure I.6 (b)**).

The ease of reorienting of the domains depends on their polarization angle with respect to the applied field. A 180° inversion of a domain is done without deformation of the elementary unit cell, unlike other slower reorientations. This explains the polarization shift when the domains are aligned to the external electric field, creating a response marked by the formation of a hysteresis cycle.

After this orientation step and in the absence of an external field, the polarization of crystallites equilibrates to a value called remanent polarization (P_r). To reverse the polarization of a crystallite, a minimum external field is necessary, called coercive field (E_c).

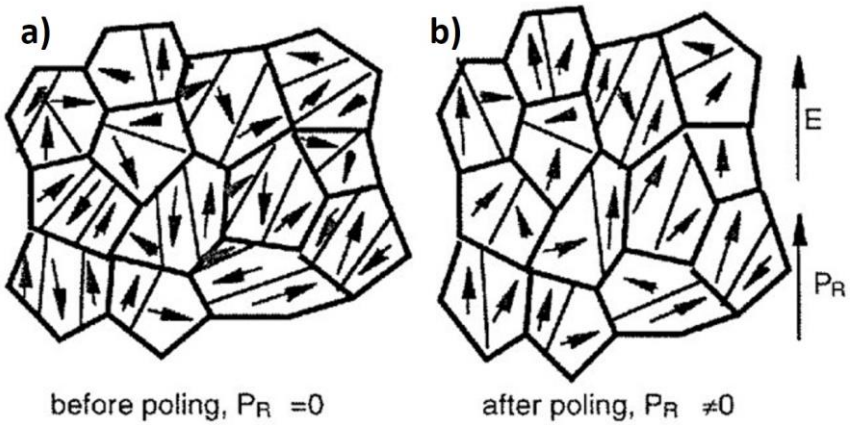

Figure I.6. Ferroelectric materials: a) before polarization and b) after polarization.

I.2.3.1. Phase Transitions in Ferroelectrics

A ferroelectric material has two states depending on its temperature: ferroelectric or paraelectric. The transition between these two states is done at a certain temperature, called Curie temperature (T_c). Below this temperature, the material is ferroelectric, and above it undergoes a structural transition and becomes paraelectric, losing its ferroelectric properties (**Figure I.7**). We can say that the increase in temperature induces a relaxation of the unit cell, which loses its distortion and becomes centrosymmetric.

The Curie temperature is an important parameter for comparing the piezoelectric properties of materials. In particular, it is at this value that the dielectric permittivity of materials is maximum. However, a Curie temperature too low can be prohibitive depending on the application.

It should be noted that this phenomenon is also observed on non-ferroelectric and non-piezoelectric materials, marked by transition temperatures modifying their piezoelectric properties.

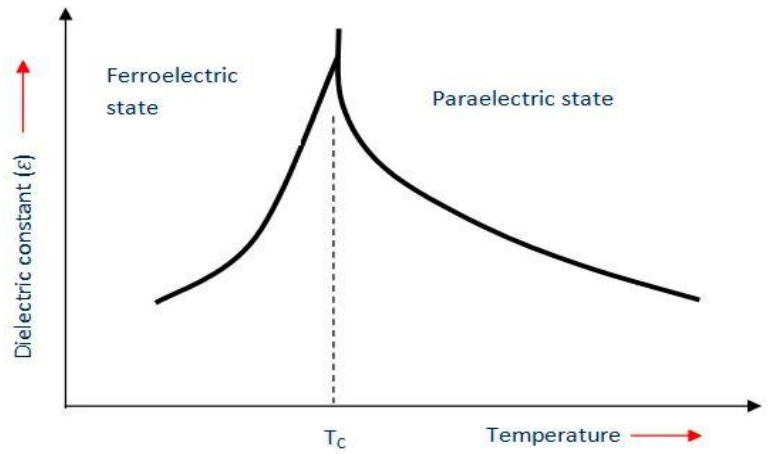

Figure I.7. Ferroelectric to Paraelectric phase transition (**Manavalan, 2005**).

I.3. Fundamentals of Ferroelectric Perovskites

Perovskite was originally the name given to the mineral $CaTiO_3$ discovered by Lev Aleksevich Von Perovski. Because the crystal lattice organization of calcium titanate was found to be identical to that of many other minerals, the name perovskite was chosen to designate this crystal lattice organization.

The perovskite structure minerals are the most abundant on earth. The lower mantle, for example, is abundant in it, largely in the form of silicate perovskite. Natural perovskites already exist before the start of their synthesis. A large number of them have shown interesting properties, and their wide and varied range of potential applications makes them of great industrial interest (**Rabe *et al.*, 2007**).

I.3.1. Perovskite Crystal Structure

Ionic compound of formula ABO_3, its structure is arranged in BO_6 octahedrons linked by their vertices. The cation A, of larger ionic radius, is positioned in the dodecahedral sites, i.e. between the octahedrons (**Figure I.8**).

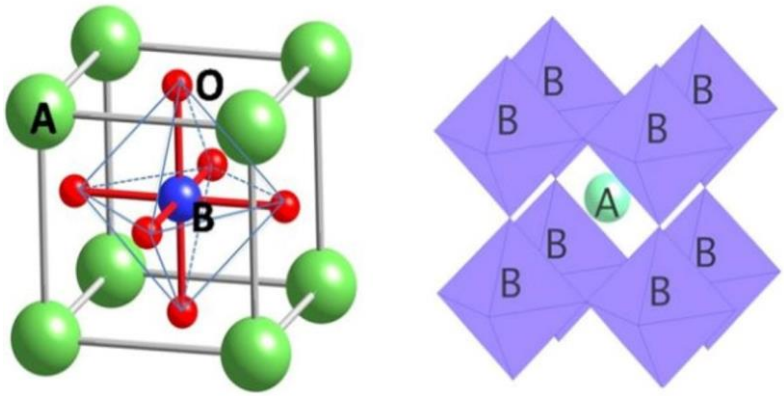

Figure I.8. The perovskite structure (**Fu and Itoh, 2011**).

The interactions between the oxygens and the cations A and B are not equivalent: the B-O bond is mostly covalent in nature, whereas the A-O bond has a more ionic character. The thermodynamic stability of the perovskite lattice comes from the balance between the coulombic forces of the chemical bonds, favoring the ferroelectric states, and the strong short-range repulsions favoring the cubic structure. The Goldschmidt tolerance factor, called t, estimates the difference between real and ideal structures (**Goldschmidt, 1926**):

$$t = \frac{R_A + R_O}{\sqrt{2}(R_B + R_O)} \qquad \text{(I.8)}$$

where R_A, R_B and R_O are respectively the ionic radius of the A, B and O-site cations. In practice, the perovskite structure is stable for $0.8 < t < 1.2$. The case t = 1 corresponds to the perfect stacking, with a cubic perovskite structure of symmetry $P3\bar{m}3$. Otherwise, values that are slightly lower or higher result in rhombohedral or tetragonal distortion, respectively.

I.3.2. The PZT Solid Solution

Lead zirconate titanate (PZT) is the most common lead based piezoelectric materials. PZTs are currently the widely used material in industry (representing 60% of piezoelectric materials). The chemistry and properties of PZTs have been extensively studied (**Tiwari, Babu and Choudhary, 2021**).

PZT ($PbZr_xTi_{1-x}O_3$) is a solid solution of $PbZrO_3$ (rhombohedral (R3c or R3m), antiferroelectric) and $PbTiO_3$ (tetragonal (P4mm), ferroelectric). PZT has a Curie temperature (T_c) of about 400°C. Cubic at temperatures above its T_c, and it takes the structure of its majority component below T_c (tetragonal if Ti > Zr and rhombohedral in the opposite case (**Figure I.9**). It is at the boundary of these two phases that the MPB is located, and more precisely at x=0.48.

Among the lead zirconate titanate compositions, the $PbZr_{0.48}Ti_{0.52}O_3$ stereochemistry shows the best piezoelectric and ferroelectric properties. In addition, it is from this composition that commercial piezoelectric components are manufactured, often also doped with other elements, such as calcium or lanthanum, to improve the properties according to the targeted application (**Tiwari, Babu and Choudhary, 2021**).

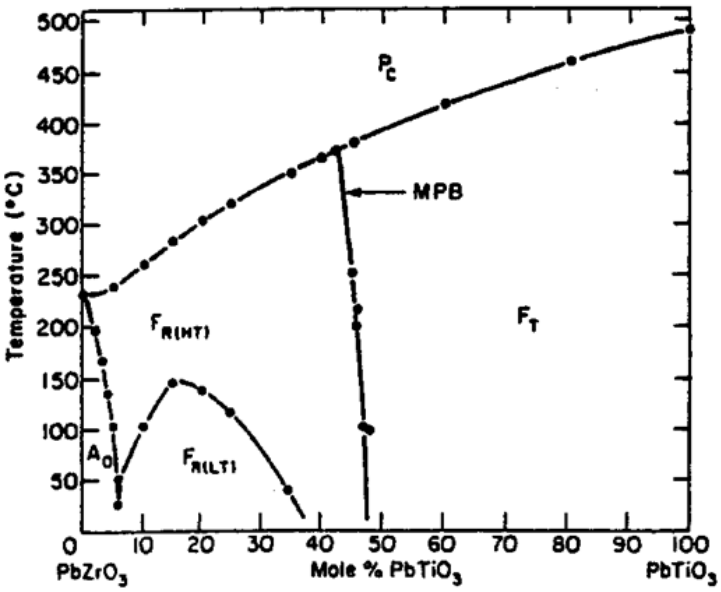

Figure I.9. PZT solid solution phase diagram (**Panda and Sahoo, 2015**).

Despite its scientific advantages and proven performance, PZT is a lead-based compound, a material known for its health and environmental dangers. Lead is especially volatile when employed in its oxide form, which causes issues not only during the manufacturing of PZT, but also during its recycling. The effects on humans have long been known as lead poisoning. The degradation of the enzymatic process and the intellectual quotient are examples of lead's influence on the organism, which is manifested by serious symptoms that harm the physical integrity of the humans. This is why, since the early 2000s, research on lead-free piezoelectric materials has exploded. The objective is to find a harmless material and whose performance, particularly electromechanical performance, is comparable to that of standard PZT.

I.3.3. Lead-Free Piezoelectric Materials

There are several lead-free piezoelectric material families available today: $BaTiO_3$ (BT), $K_{0.5}Na_{0.5}NbO_3$ (KNN), $Bi_{0.5}Na_{0.5}TiO_3$ (BNT), and $BiFeO_3$ (BFO) lead-free piezoelectric ceramics. These materials crystallize in the perovskite lattice. Based on statistical data from publications since 2004, as shown in **Figure I.10**, the rate of growth in research of lead-free piezoelectric ceramics has been observed.

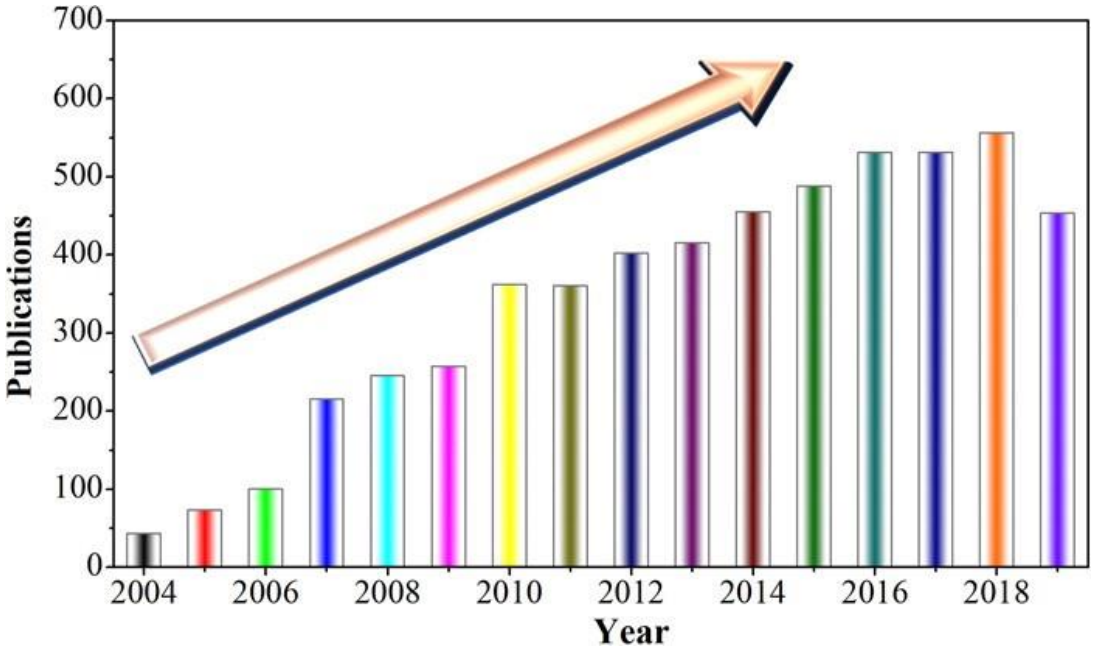

Figure I.10. Published articles on Pb-free piezoelectric materials (**Wu, 2020**).

This work focuses on piezoelectric ceramics based on $BaTiO_3$ and $BiFeO_3$. Although these compounds were discovered and investigated many years ago, in 1950 for $BaTiO_3$ and 1960s–1970s for $BiFeO_3$ (**Srihari, Vinayakumar and Nagaraja, 2020**), interest in them has only increased in the past fifteen years, in response to legislative restrictions on lead.

I.3.3.1. Barium Titanate, $BaTiO_3$

Barium titanate is used in the capacitor industry for its very interesting properties, namely a very high dielectric constant and high-quality factor. It is the first ferroelectric and piezoelectric oxide with a perovskite structure to be discovered. Since the 1940s, this material has been thoroughly investigated (**Kanzig, 2011**).

Similar to PZT, $BaTiO_3$ has an ABO_3 structure and its crystal structure changes with temperature (**Figure I.11**). Below -90 °C, barium titanate is in the rhombohedral phase. The unit cell deforms to adopt the orthorhombic structure in the -90 to 5 °C temperature range. Above 5 °C, $BaTiO_3$ has a tetragonal structure and exhibits spontaneous polarization, piezoelectricity, and ferroelectricity (**Bechmann, 1956; Shao *et al.*, 2003**). From about 125 °C, barium titanate shows a cubic paraelectric phase.

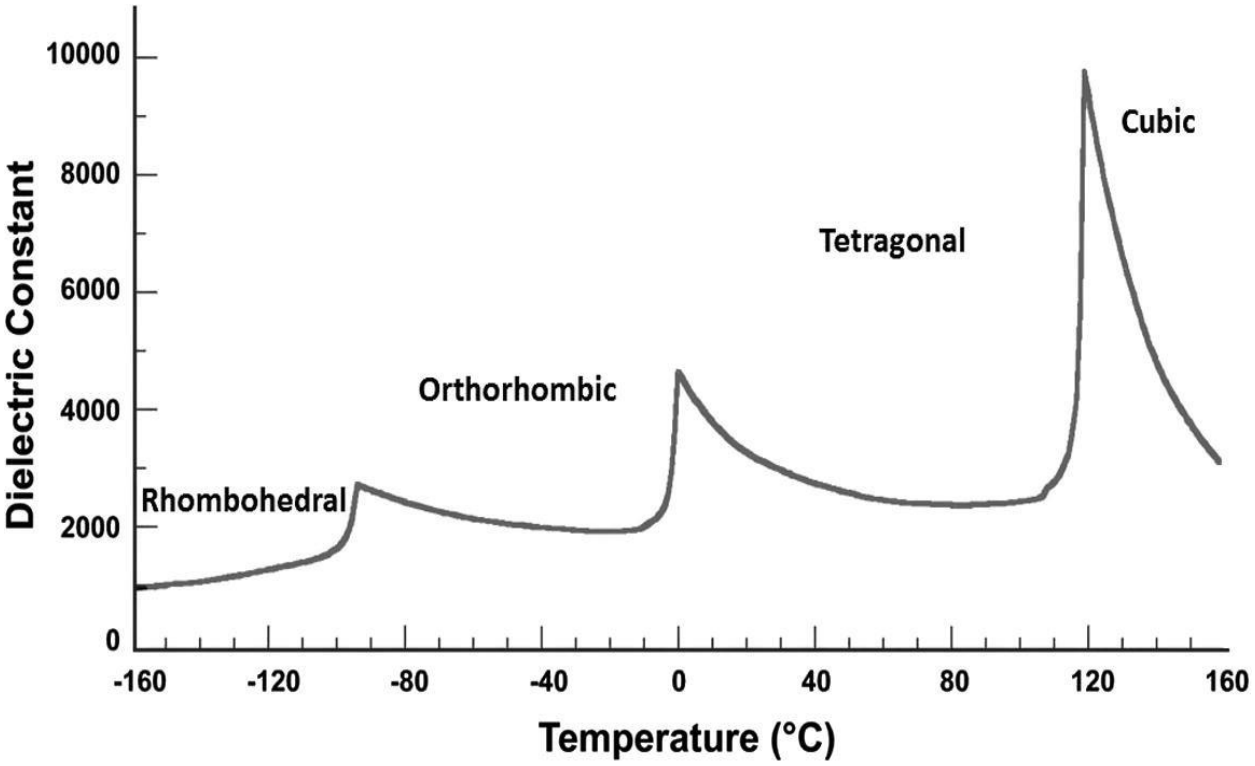

Figure I.11. Phase transition temperatures of $BaTiO_3$ visualized by permittivity measurement.

However, the low Curie temperature of BT limits its usage in some applications. In terms of piezoelectric characteristics, barium titanate demonstrates a good electromechanical coupling factor ($k_p \approx 0.50$) and a piezoelectric constant $d_{33} \approx 190$ pC/N. However, the piezoelectric performance is inferior to that of PZT, which is a barrier for applications such as sensors and actuators.

Chemical modification is the most frequently used method for adjusting a material's electrical properties (dielectric, piezoelectric, ferroelectric, strain, etc.), and it includes chemical substitution, addition of oxides, compounds, and so on. Chemical substitution, when combined with ion substitution or doping to replace matrix ions, can induce lattice distortion (or oxygen octahedra tilts), the formation of defects, element enrichment, and other effects. These cause changes in local chemical homogeneity, grain size, and phase structure, as well as secondary phase formation, all of which have a significant effect on electrical properties. Chemical substitution in $BaTiO_3$ perovskite mainly involves the replacement of cations at the Ba^{2+}/Ti^{4+} site or both of them (**Shao *et al.*, 2003**).

Because of the similarity of ion valence and ionic radius, Ca^{2+} is the most commonly used cation for A (Ba^{2+})-site substitution. Moreover, the addition of Ca^{2+} can stabilize the ferroelectric phases (**Figure I.12**), resulting in the shift of T_{R-O} and T_{O-T} to low temperatures, and It also helps to keep the T_c unchanged (**Huang *et al.*, 2017; Shu, Reed and Button, 2018**). This demonstrates that Ca^{2+} substitution can improve the stability of the tetragonal ferroelectric phase.

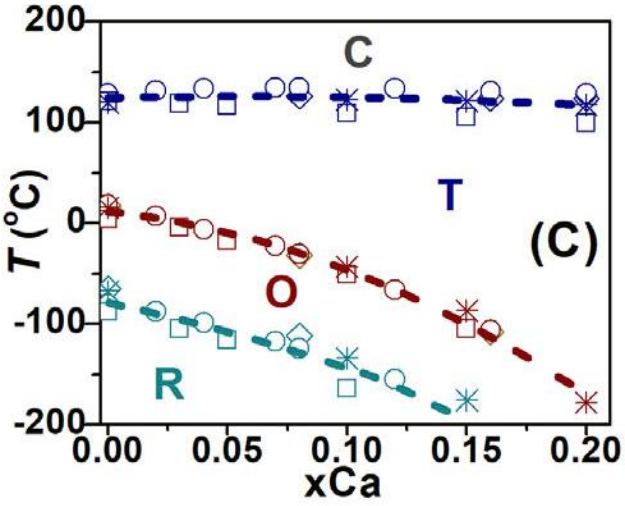

Figure I.12. Phase diagram of Ca-doped BT ceramics (**Huang *et al.*, 2017**).

- **$(Ba_{1-x}Ca_x)(Zr_yTi_{1-y})O_3$ (BCZT) Solid Solution**

Interest in $BaTiO_3$ has grown strongly in the last decade with the discovery of the $(Ba_{1-x}Ca_x)(Zr_yTi_{1-y})O_3$ (BCZT) solid solution with high piezoelectric constant. Indeed, Liu et al. (**Liu and Ren, 2009**) have published in 2009 a solid solution, $x(Ba_{0.7}Ca_{0.3})TiO_3$-$(1-x)Ba(Ti_{0.8}Zr_{0.2})O_3$, whose piezoelectric constant reaches more than 600 pC/N when x = 0.5. They attribute the increase in piezoelectric properties to the presence of a morphotropic phase between rhombohedral and tetragonal phases. This morphotropic zone would thus be similar to PZT and would end in a triple point between the rhombohedral, tetragonal, and cubic paraelectric phases.

However, except in the case of PZT, this morphotropic line is not vertical, implying that the piezoelectric properties vary significantly with temperature (**Bao *et al.*, 2010; Zhang *et al.*, 2014**).

The morphotropic zone of the BCZT has received greater attention recently. In fact, the appearance of rhombohedral, tetragonal, and cubic phases is exceptional for a $BaTiO_3$-based material. Keeble et al (**Keeble *et al.*, 2013**), for example, re-examined the phase diagram of BCTZ from a crystallographic point of view. They discovered an orthorhombic phase between the rhombohedral and tetragonal phases. The rhombohedral-orthorhombic and orthorhombic-tetragonal phase transitions involve a dielectric constant variation in temperature that is too small to detect. This explains that the previous authors could not detect it. **Figure I.13** shows the orthorhombic phase that has been added to the BCTZ phase diagram, where the orthorhombic phase represented in rose between the rhombohedral phase in blue and the tetragonal phase in green.

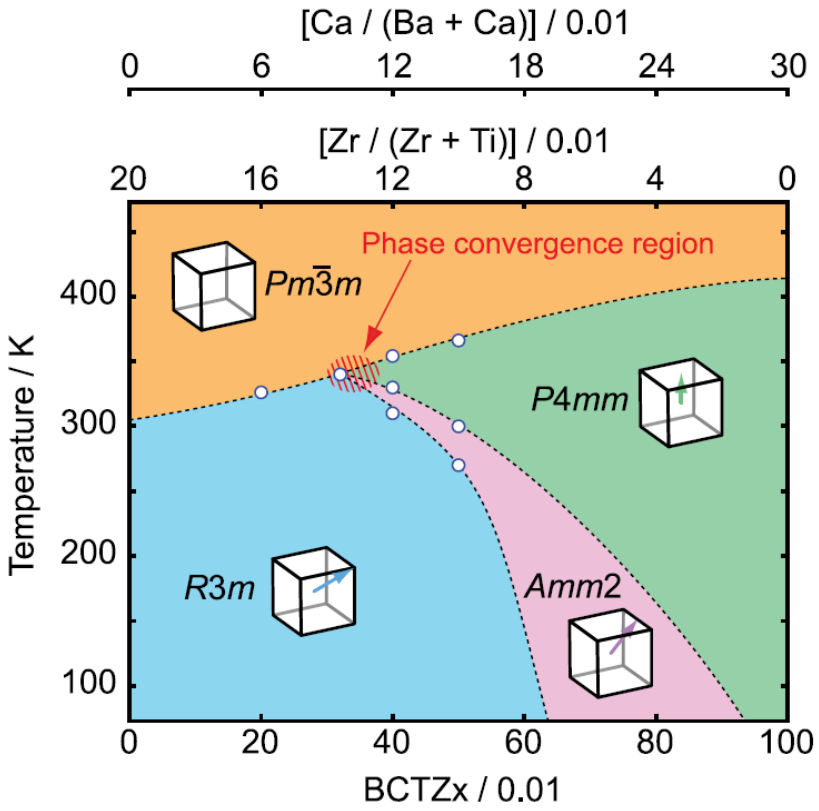

Figure I.13. Phase diagram of the solid solution $x(Ba_{0,7}Ca_{0,3})TiO_3 - (1\text{-}x)Ba(Ti_{0,8}\,Zr_{0,2})O_3$ (**Keeble *et al.*, 2013**).

I.3.3.2. Bismuth Ferrite, $BiFeO_3$

Since the discovery of spontaneous polarization of more than 150 µC cm^{-2} in 2003, $BiFeO_3$ (abbreviated as BFO) has received increasing attention (**Wang *et al.*, 2003**).

$BiFeO_3$ is synthesized from stoichiometric amounts of iron oxide (Fe_2O_3) and bismuth oxide (Bi_2O_3), and it can decompose again under certain conditions (temperature, pressure, etc.) according to the following reaction (**Palai *et al.*, 2008**):

$$2BiFeO_3 \rightarrow Fe_2O_3 + Bi_2O_3 \qquad (I.9)$$

Palai et al. (**Palai *et al.*, 2008**) studied the phase diagram of BFO. The authors highlight the presence of three phases as a function of temperature, denoted as α, β, and γ (**Figure I.14**). From room temperature to 825°C, the rhombohedral α phase is predominant. The β phase forms at temperatures ranging from 825°C to 925 °C, but its internal symmetry has not yet been formally defined. Above 925°C, the γ phase with a cubic structure appears. This corresponds to the phase with the highest symmetry of the $BiFeO_3$.

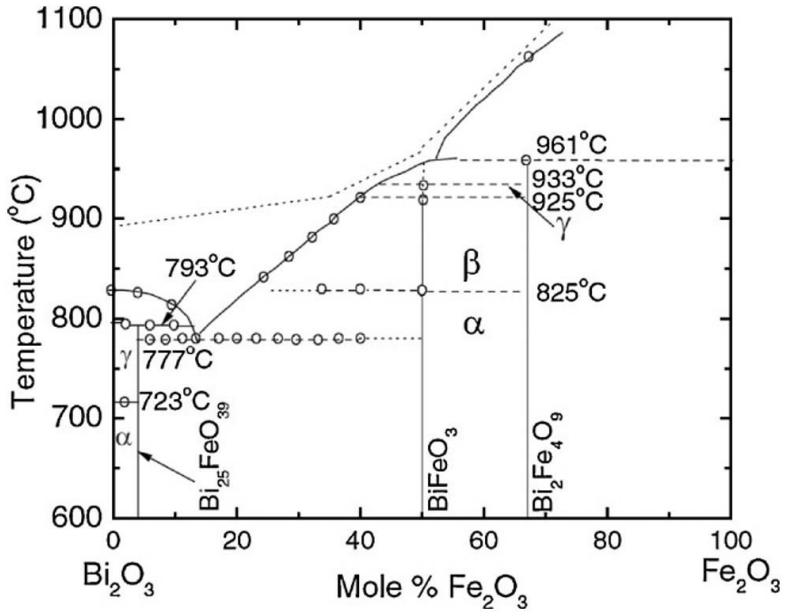

Figure I.14. Bi_2O_3–Fe_2O_3 phase diagram (**Palai *et al.*, 2008**).

At room temperature, bulk $BiFeO_3$ crystallizes in a rhombohedral crystal structure with space group R3c. This α phase was first described in 1971 by Moreau et al. (**Moreau *et al.*, 1971**) and has for lattice parameters a_{Rh} = 5.5638 Å and α_{Rh} = 59.42°. It is therefore often more correct to describe the structure as a deformed perovskite, in this case a pseudocubic lattice with parameters a_{ps} = 3.9684 Å and angles α_{ps} = 89.495° and $\beta_{ps} = \gamma_{ps}$ = 90.505°. In this case the ferroelectric polarization develops along the $[111]_{ps}$ direction due to the displacement and rotation, in the opposite direction, of the FeO_6 octahedra around this axis (**Kubel and Schmid, 1990**). Finally, the structure of $BiFeO_3$ can be represented in a hexagonal lattice, with the $[001]_{hexa}$ axis parallel to the $[111]_{ps}$ axis (diagonals of the perovskite unit cube). In this lattice, the unit cell parameters are $\mathbf{a}_{hexa}$ = 5.5879 Å and $\mathbf{c}_{hexa}$ = 13.8670 Å (**Moreau *et al.*, 1971; Palewicz *et al.*, 2007; Chen *et al.*, 2008**).

For its ferroelectric and piezoelectric properties, bismuth ferrite is used in a various application, including actuators, sensors, and energy storage devices. It has a high Curie temperature of 810°C and a strong electrical polarization (100 μC cm^{-2}) at room temperature (**Wu *et al.*, 2016**).

- **$BiFeO_3$-$BaTiO_3$ Solid Solution**

Materials based on (1-x)$BiFeO_3$-x$BaTiO_3$ (BFO-xBT) are promising candidate for lead-free piezoelectrics. At room temperature, $BiFeO_3$ is rhombohedral with high T_c, while $BaTiO_3$ is tetragonal. In 1999, Kumar et al (**Kumar, Srinivas and Suryanarayana, 1999**) have investigated the variation of the lattice parameters of the BFO-BT binary system with BFO content, as shown in **Figure I.15 (a)**. It can be seen that as the BFO content decreases, the structure gradually transfers from rhombohedral to cubic phase and then to the tetragonal phase. Thus, with BFO concentrations of 6 % and 67 %, respectively, the BFO-xBT system has cubic-tetragonal and rhombohedral-cubic phase boundaries. Leontsev et al. (**Leontsev and Eitel, 2009**) colleagues make several changes to Mahesh' phase diagram based on dielectric properties and DSC results, as illustrated in **Figure I.15 (b)**. It was found that a pseudo-cubic phase exists in the composition range of x ~ 0.25-0.4. The absence of splitting peaks in the XRD pattern identifies the cubic phase of the BFO-BT system, whereas the XRD simply reflects the average structure of the crystal. When Transmission Electron Microscopy (TEM) and ferroelectric property analysis are combined, it is clear that this average cubic structure is not completely symmetrical. Moreover, extensive research efforts have been committed for improving the piezoelectric properties of the BFO-BT system (**Wei *et al.*, 2013; Hwan Lee *et al.*, 2015; Kim *et al.*, 2017; Habib *et al.*, 2020; Wang *et al.*, 2022**). For example, water-quenched modified BFO-BT ceramics exhibit a high piezoelectric coefficient while maintaining a high Curie temperature comparable to lead-based ceramics (**Hwan Lee *et al.*, 2015**). It should be noted that the BFO-BT system with a pseudo-cubic structure commonly exhibits high electrostrain and polarization response in the presence of an electric field. This feature shows that the BFO-BT system has a wide range of applications in electrostrain and energy storage fields.

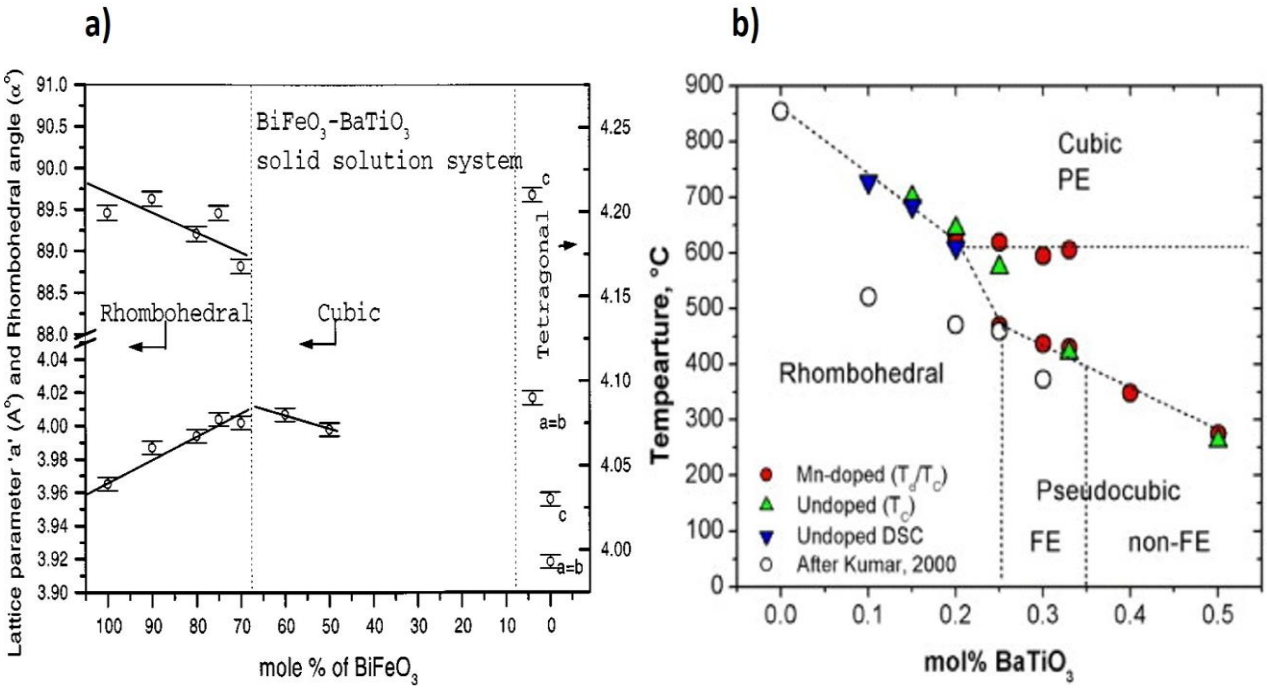

Figure I.15. a) Variation of lattice parameters for the BFO-BT system (**Kumar, Srinivas and Suryanarayana, 1999**); b) Revised phase diagram for the BFO-BT system (**Leontsev and Eitel, 2009**).

I.4. Sintering of Ceramics Materials

Sintering is a Physicochemical process that consists in transforming a compact of powders into a consolidated and coherent material under the action of heat. In this study, conventional solid-state sintering and flash sintering were used as sintering processes.

I.4.1. Conventional Solid-State Sintering

Conventional solid-state sintering is a thermal treatment carried out at a temperature below the melting temperature of the main components of the material, which allows the generation of bonds between the particles by material diffusion (**Shi, 1999**). This sintering is generally accompanied by a linear shrinkage compared to the green sample (elimination of porosity) and thus densification of the material.

From an experimental point of view, the conventional sintering cycle generally includes a heating period to the desired sintering temperature, then an isothermal period, and finally cooling. The heating and cooling rates must be controlled to avoid cracking the material.

I.4.1.1. Sintering Driving Force

The thermodynamic origin of sintering is the reduction of the global free energy of the system, which is mainly the total interfacial energy in a powder compact. This energy results from the contribution of the solid-gas interfaces, surface area A_{SG}, and the surface tension γ_{SG} and the contribution of the solid-solid interfaces at the grain boundaries, the area A_{SS} and the surface tension γ_{SS}. The variation of the free energy of the system during the sintering is given by the following relation(**Searcy, 1985; Bernache-Assollant and Bonnet, 2005**):

$$\Delta G = \gamma_{SS}\Delta A_{SS} + \gamma_{SG}\Delta A_{SG} \qquad \text{(I.10)}$$

In a single-phase system, the solid-gas interfaces are more energetic than the solid-solid interfaces. Two solutions are possible to lower the interfacial energy in a ceramic:

- Reducing the area of solid-gas interfaces in favor of lower energy solid-solid interfaces. This evolution occurs by welding the grains together (creation of grain boundaries).
- Decreasing the area of the solid-gas interfaces using a medium magnification of the grains (and thus the decrease in the number of grains).

Locally, the transport of the material is directly related to the curvatures of the surfaces. Laplace's law gives the pressure difference between two phases separated by a surface curve:

$$\Delta P = P_1 - P_2 = \gamma\left(\frac{1}{r'} + \frac{1}{r''}\right) \qquad \text{(I.11)}$$

In this expression, r' and r'' are the principal radii of curvature of the interface at a given point and γ is the surface tension of this interface. The pressure differences lead in the vicinity of concave and convex surfaces to gap concentrations, respectively higher and lower than equilibrium concentrations near a flat surface. The resulting concentration gradients can thus be considered as local driving forces for sintering.

I.4.1.2. Sintering Stages

The solid-state sintering process is performed in three main stages: initial, intermediate, and final stage (**Figure I.16**) (**Randall, 1996**).

- **Initial Stage:** it describes the transformation of the raw material (assembly of compacted grains, of weak compactness) into a material that presents a certain mechanical behavior.

During this stage, the surface diffusion leads to the consolidation of the compact with the formation of solid necks at the level of the joints of grains. This phenomenon ends at about 65-70% of relative density.

- **Intermediate Stage:** This is the largest part of the densification process. It corresponds to the progressive elimination of the open porosity. It is accompanied by densification and leads to the creation of pores trapped in the material (closed porosity).
- **Final Stage:** It takes place from the relative densities of about 92%. This stage leads to the complete elimination of the closed porosity. The densification is slowed down while the grain size becomes important.

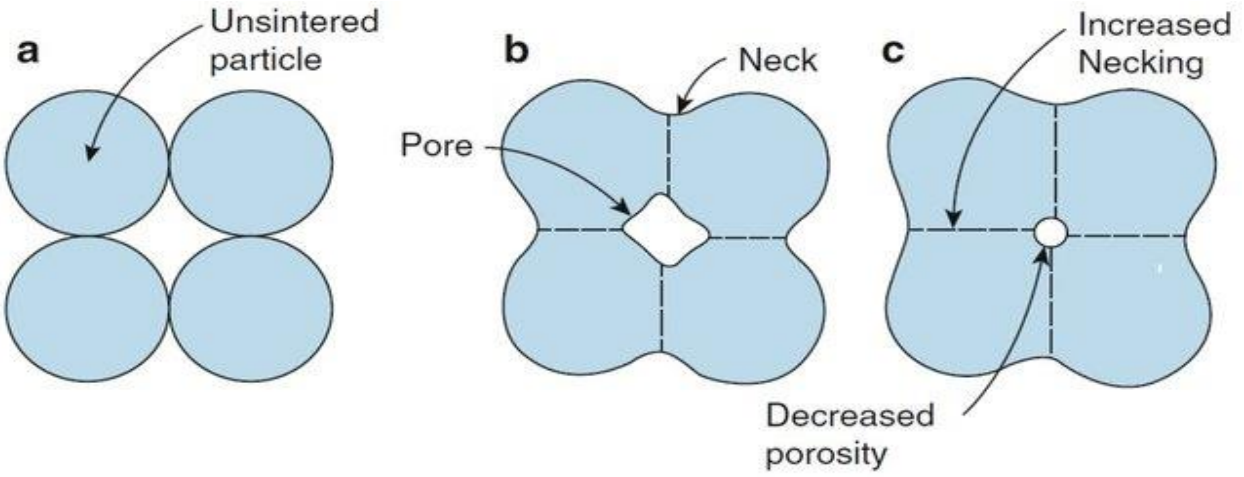

Figure I.16. Conventional solid-state sintering stages: a) initial, b) intermediate, and c) final stage.

I.4.2. Flash Sintering

New heating techniques have been proposed in the literature to accelerate the densification kinetics by reducing the sintering temperature and the cycle time. Some of these techniques are based on the use of an electric current or field to activate the sintering process. The most developed is the ECAS (Electric Current Activated/Assisted Sintering) technique also known as Spark Plasma Sintering (SPS). This process allows the rapid densification of a powder confined in a matrix by heating the whole (powder + matrix) by the passage of a current (direct, pulsed, or alternating) and by applying uniaxial pressure (**Grasso, Sakka and Maizza, 2009; Orrù *et al.*, 2009**). The speed and efficiency of this technique come from the direct heating of the powder by the Joule effect (fast densification) and the application of a charge. The characteristic time of SPS sintering is from a few minutes to a few tens of minutes.

Another sintering technique based on the use of current, called flash sintering, has also appeared in recent years. Like SPS, flash sintering can be classified as electrically assisted or activated sintering process (ECAS). This new sintering technique was discovered by Cologna et al (**Cologna, Rashkova and Raj, 2010**) and it allows a dramatic reduction in sintering time and temperature.

I.4.2.1. Flash Sintering Principle

Flash sintering consists of heating a raw compact, placed between two electrodes, in a furnace and applying a direct (DC) or alternating current (AC) (**Figure I.17**). Under these conditions, an electric current flow through the sample allowing its heating and densification in a few seconds and at a much lower temperature than in conventional sintering. It is the rapidity of sintering that led Cologna et al. (**Cologna, Rashkova and Raj, 2010**) to name this technique "Flash sintering". The originality of this technique lies in the fact that neither a uniaxial pressure nor a matrix enveloping the powder is necessary. The implementation of this sintering process is very simple and economical. The setup is mainly composed of a furnace and a power supply.

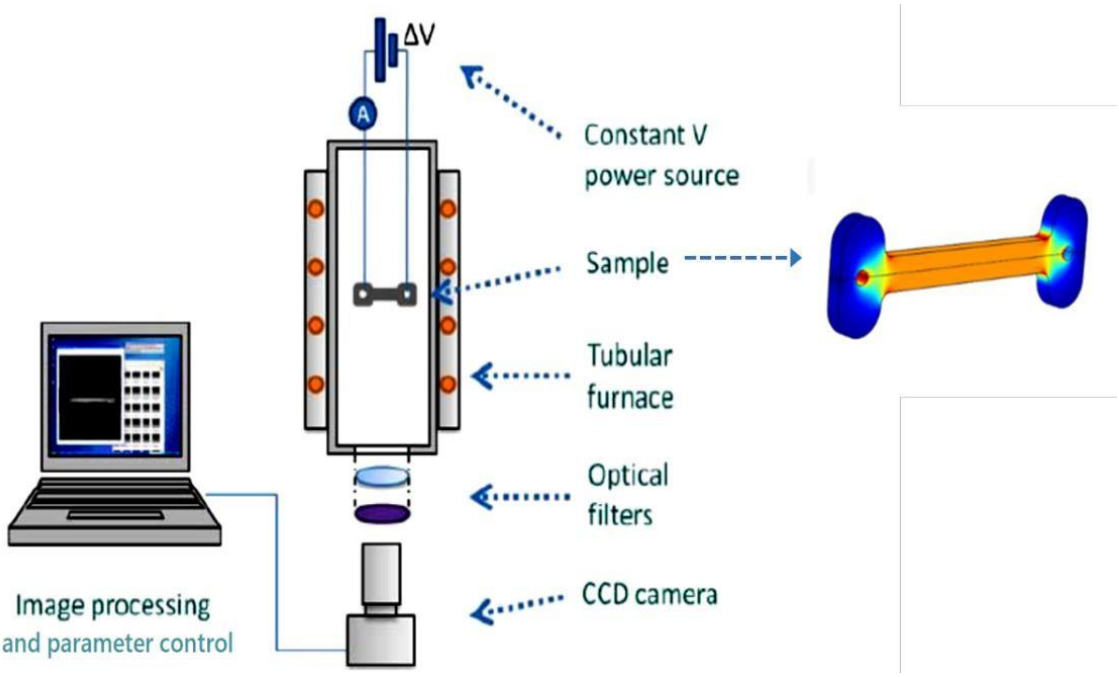

Figure I.17. Flash sintering principle (**Cologna, Francis and Raj, 2011**)

I.4.2.2. Joule Heating During Flash Sintering

Several studies have linked flash sintering behavior to Joule heating. Joule heating is a physical effect that occurs when current flows through a green body, producing thermal energy.

The green body, in particular, heats up quickly due to Joule heating, which is proportional to the square of the current in an ohmic regime. Joule heating can speed up the movement of ceramic grains and increases densification because the diffusivity of ceramic particles increases exponentially with temperature (**Dancer, 2016**). Based on this mechanism, the following relationship between ceramic sintering rate and temperature can be constructed:

$$log_{10}\frac{Rate_2}{Rate_1} = \frac{Q}{2.3R}\left(\frac{1}{T_2} - \frac{1}{T_1}\right) \qquad \text{(I.12)}$$

where $Rate_1$ and $Rate_2$ are respectively the densification rates without and with an applied electric field. Q is the sintering activation energy, and T_1 and T_2 are the furnace and grain temperatures, respectively.

I.4.2.3. Flash Sintering of Ceramics

The first work on flash sintering of ceramics, published in 2010 by Cologna et al (**Cologna, Rashkova and Raj, 2010**), was carried out on yttria-stabilized zirconia (YSZ) in the shape of a dog bone. it shows that 3 mol% yttria-stabilized zirconia (3YSZ) can be sintered to full density at ~850°C in a few seconds, by the application of a DC electrical field. Compared to conventional sintering, the same material (3YSZ) requires several hours at 1450°C to complete the sintering process.

The flash sintering process has been successfully used for a wide range of oxide ceramics: Zirconia (Cologna, Rashkova and Raj, 2010b; Cologna, Prette and Raj, 2011; Qin *et al.*, 2016; Ren, Liu and Wang, 2020; Campos *et al.*, 2021), Silicon carbide **(Zapata-Solvas *et al.*, 2013**), Boron carbide (**Rosenberger, Brennan and Fry, 2021**), Titanium oxide (**Zhang, Nie and Luo, 2016; Yoon *et al.*, 2018; Yang *et al.*, 2022**), Zinc oxide (Schmerbauch *et al.*, 2014; Wang *et al.*, 2019; Zhou, Li, Huang, *et al.*, 2021), strontium titanate (**Karakuscu *et al.*, 2012**), barium titanate (**Shi *et al.*, 2019; Zhu *et al.*, 2021**), potassium niobate (**Shomrat *et al.*, 2015**), bismuth ferrite (**Perez-Maqueda *et al.*, 2017**). Recently, the flash sintering process has been used not only to densify materials, but also to induce the reaction and synthesis of materials (**Gil-González *et al.*, 2018**). This technique, called "Reactive Flash Sintering" (RFS), has been massively applied in recent years for the fabrication of a single and multi-phase ceramic oxides (**Avila and Raj, 2019; Jia *et al.*, 2019; Yoon *et al.*, 2019, 2020; Wu *et al.*, 2020; Avila *et al.*, 2021**).

I.4.2.4. Flash Sintering Stages

The evolution of the current density as a function of time (**Figure I.18**) allows us to distinguish three stages that characterize flash sintering (**Zhou, Li, Zhu, *et al.*, 2021**).

- **Stage I: incubation**

This is the period during which the evolution of the current density is very low. This period is characterized by a time called incubation time. The incubation stage is explained by Joule heating and the formation of oxygen vacancies in the oxides.

- **Stage II: sintering stage**

After the incubation period, the current density through the sample increases rapidly and is accompanied by very rapid densification of the sample. This increase in current corresponds to a peak in the electrical power dissipated in the sample which could cause damage to the flash setup or even damage to the sample. For these reasons, the current density must be limited to a maximum value that we will call I_{max}.

- **Stage III: stable stage**

The current density is kept constant during a well-defined period (in seconds) called time under constant current. During this period, the value of the electric field becomes lower than the one initially fixed and the densification of the sample continues until the voltage is switched off.

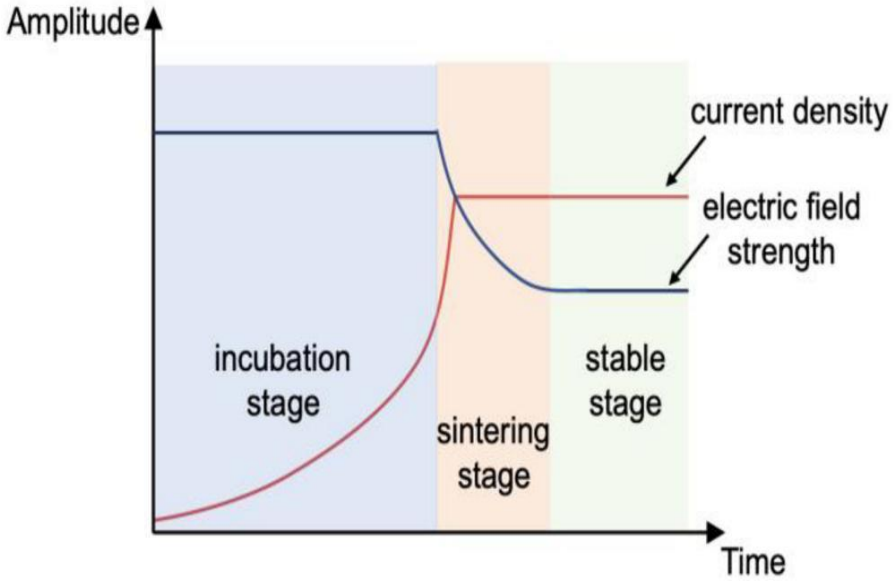

Figure I.18. Flash sintering stages (**Zhou, Li, Zhu, *et al.*, 2021**).

I.4.2.5. Stoichiometry Variations Due to Volatile Compounds Losses

It is preferable to use the flash sintering technique for the synthesis of complicated compounds that contain volatile elements since flash sintering operates at lower temperatures, which helps to prevent volatilization of low volatile oxide compounds or melting samples with low melting temperature.

Shomrat et al. (**Shomrat *et al.*, 2015**) have noted one of the advantages of flash sintering over conventional solid-state sintering with regard to the preparation of potassium niobate ($KNbO_3$) ceramics. The problem in $KNbO_3$ (KN) synthesis arises from potassium oxide (K_2O) volatilization above 800 °C, which does not maintain stable the stoichiometry of KN. Flückiger et al. (**Flückiger and Arend, 1978**) demonstrated that the weight loss of the KN sample, due to K_2O evaporation, increases with temperature.

Compared with other ceramic powders that can be fully sintered using the solid-state sintering method, the use of flash sintering on this compound reduces the volatility of K_2O, resulting in high-density ceramics due to the fast-sintering process and a stoichiometric K/Nb ratio that remains constant throughout the process.

I.5. Theoretical Backgrounds of Kinetic Analysis

Kinetic analysis is widely employed as an approach for the study of many technologically important transformations in solids such as oxidation, melting, sublimation, degradation and thermal crystallization. The kinetic analysis of solid-state reactions helps to provide the essential kinetic parameters in order to model and optimize the processes at an industrial scale **(Brown *et al.*, 2000)**. However, the study of kinetics in solid phase is quite different from that in liquid or gas phase. In solids, the mobility of molecules is reduced. The same constituents can have a different close environment because they occupy different positions within the structure of the solid (or because of the presence of imperfections). Thus, the reactivity of identical constituents can vary within the solid and over time. Some of them can be destabilized, which leads to a modification of their reaction capacity. The kinetic study in solid phase becomes more complex **(Brown, Dollimore and Galwey, 1980)**.

I.5.1. DSC Kinetics

The determination of a reaction mechanism in solid phase is delicate, especially if one relies only on kinetic observations. Nevertheless, it is always possible to determine effective kinetic constants of the overall process and to extract Arrhenius parameters.

The rate of conversion is generally described by the equation:

$$\frac{d\alpha}{dt} = k(T)\, f(\alpha) \qquad \text{(I.13)}$$

Where t is time, T is temperature, α is the extent of conversion, f(α) is the kinetic model, and k(T) the Arrhenius rate coefficient.

The extent of conversion, α, is defined as a ratio of the volume of the current crystallized phase to the total volume of crystallized phase. When the progress is measured as heat change by DSC, the extent of conversion α is calculated as a ratio of the current heat change, ΔH, to the total heat, ΔH_{tot}, using the following equation:

$$\alpha = \frac{\int_{t_0}^{t} (dH/dt)dt}{\int_{t_0}^{t_f} (dH/dt)dt} = \frac{\Delta H}{\Delta H_{tot}} \qquad \text{(I.14)}$$

where t_0 and t_f respectively reflect the initial and final time of the DSC peak, and dH/dt the heat flow measured by DSC (**Figure I.19**).

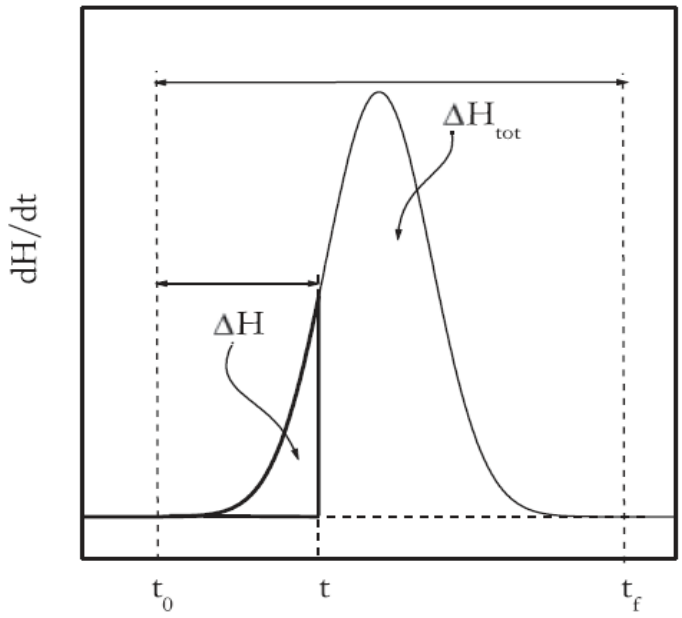

Figure I.19. Calculation of the extent of conversion from DSC curve **(Vyazovkin, 2015).**

According to the empirical law of Arrhenius, K(T) is defined as follows:

$$k(T) = A\, e^{(-E_a/RT)} \qquad \text{(I.15)}$$

Where, A is the pre-exponential factor (min^{-1}), E_a is the activation energy (kJ/mol) and R the universal gas constant.

Combining **Eqs (I.13)** and. **(I.15)**, gives the fundamental kinetic equation in **Eq. (I.16)** that describe the DSC results:

$$\frac{d\alpha}{dt} = A\, e^{(-E_a/RT)} f(\alpha) \qquad \text{(I.16)}$$

The Arrhenius parameters (A and E_a) and the kinetic model f(α) are called the kinetic parameters (triplet). These parameters allow to entirely describe the kinetics of a reaction.

For non-isothermal DSC experiments at linear heating rate, β = dT/dt, **Eq (I.16)** can be expanded to:

$$\frac{d\alpha}{dT} = \frac{A}{\beta}\, e^{(-E_a/RT)} f(\alpha) \qquad \text{(I.17)}$$

Nearly all the thermal analysis methods start from the fundamental differential kinetic **Eqs (I.16)** and **(I.17)** or the integral forms of them as given below:

$$g(\alpha) = \int_0^{\alpha} \frac{1}{f(\alpha)} d\alpha = \frac{A}{\beta} \int_0^{T} \exp\left(-\frac{E}{RT}\right) dT \qquad \text{(I.18)}$$

where g(α) is the integral form of f(α). The kinetic model f(α) describes the shape of α curve as a function of time. The most common f(α) kinetic models are listed in **Table I.1**. These models are constructed by considering a certain evolutionary process in the solid. For example, the kinetic model of Avrami-Erofeev describes an evolution process by multiple nucleations. It takes into account the fact that developed nucleation zones can merge or even, that a developed nucleation zone can eliminate a nucleation site. A number of kinetic models are described in detail by Brown et al (**Brown, Dollimore and Galwey, 1980**).

Table I.1. Solid-state Kinetic models with their corresponding f(α) functions **(Hatakeyama, Quinn and Wiley, 1999; Vyazovkin, 2015)**.

Kinetic model	**Code**	**f(α)**
Reaction-order		
First order	F1	$(1 - \alpha)$
Second order	F2	$(1 - \alpha)^2$
Phase boundary		
Contracting cylinder	R2	$2(1 - \alpha)^{1/2}$
Contracting sphere	R3	$3(1 - \alpha)^{2/3}$
Nucleation and growth (Avrami-Erofeev)		
Two-dimensional nucleation	A2	$2(1 - \alpha)[-\ln(1 - \alpha)]^{1/2}$
Three-dimensional nucleation	A3	$3(1 - \alpha)[-\ln(1 - \alpha)]^{2/3}$
Four-dimensional nucleation	A4	$4(1 - \alpha)[-\ln(1 - \alpha)]^{3/4}$
Diffusion		
One-dimensional diffusion	D1	$1/2\alpha$
Two-dimensional diffusion	D2	$[-\ln(1 - \alpha)]^{-1}$
Three-dimensional diffusion	D3	$3/2(1 - \alpha)^{2/3}[1-(1 - \alpha)^{1/3}]^{-1}$

I.5.2. Activation Energy Determination Using Isoconversional Methods

Isoconversional methods are methods based on the principle that is at a certain extent of conversion α, the solid state reaction rate depends only on temperature **(Vyazovkin and Sbirrazzuoli, 2006)**. Taking the logarithmic derivative of the general kinetic equation (**Eq (I.13)**), at a constant α, we obtain the equation:

$$\left[\frac{\partial \ln\left(\frac{d\alpha}{dt}\right)}{\partial T^{-1}}\right] = \left[\frac{\partial \ln \mathrm{k}(T)}{\partial T^{-1}}\right] + \left[\frac{\partial \ln f(\alpha)}{\partial T^{-1}}\right] \qquad \text{(I.19)}$$

Note that at a given α, f(a) remains constant and the second term on the right-hand side of the above equation is zero. Thus,

$$\left[\frac{\partial \ln\left(\frac{d\alpha}{dt}\right)}{\partial T^{-1}}\right] = -\frac{E_\alpha}{R} \qquad \text{(I.20)}$$

According to this equation, the activation energy can therefore be determined without any prior estimation or determination of the kinetic model of the reaction, which gives these methods the name of "Model-Free" methods.

In order to determine the activation energy E_a, the experimental tests must be performed using a series of 3-5 runs at different heating rates. **Figure I.20** illustrates the idea of determining the isoconversional rate from two nonisothermal runs conducted at the heating rates β1 and β2. It is recommended to evaluate the activation energy in the conversion α range from 0.1-0.9 with a step-size of 0.05 **(Vyazovkin *et al.*, 2011)**. The variation of the activation energy E_a as a function of α allows the detection of the nature of the process. If E_a is constant, the process studied is most likely simple and takes place in a single step **(Boonchom, 2008; Janković, Mentus and Jelić, 2009; Louaer *et al.*, 2019; Taibi *et al.*, 2019)**. While a variation of more than 10% reflects a complex process **(Gao and Dollimore, 1993; Vlaev, Nikolova and Gospodinov, 2004; Janković, Mentus and Jelić, 2009)**.

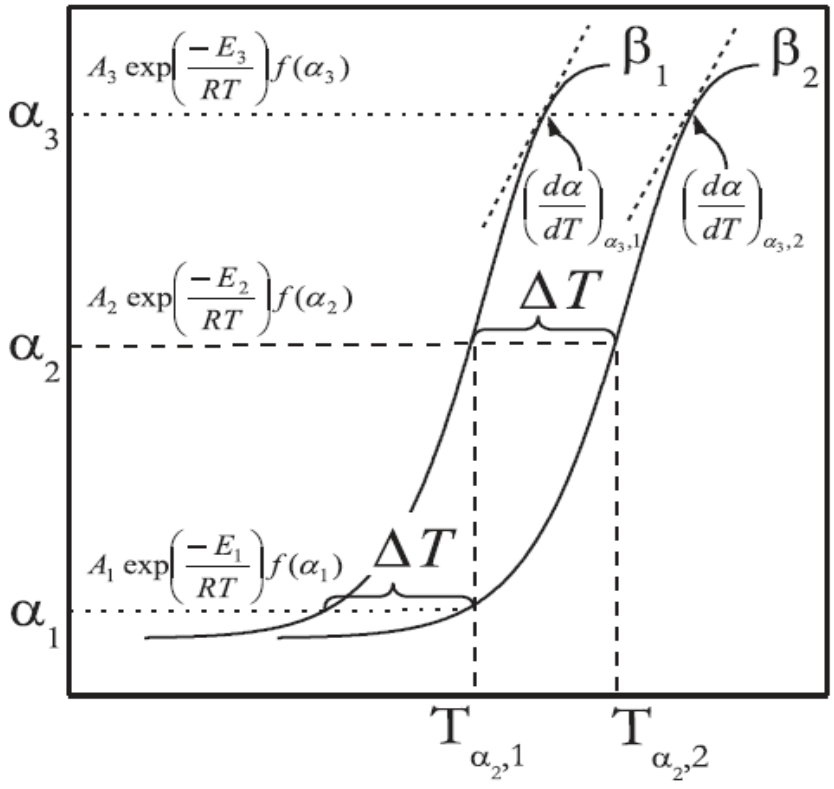

Figure I.20. Diagram representing the individual rate equations associated with different values of conversion α and temperature intervals ΔT **(Vyazovkin and Sbirrazzuoli, 2006)**.

Many methods have been developed based on the isoconversional principle. The most popular methods are: Freidman, Kissinger-Akahira-Sunose (KAS) and Ozawa-Flynn-Wall (OFW) Isoconversional methods.

I.5.2.1. Friedman (FR) method

Friedman (FR) method **(Friedman, 1964)** start directly from **Eq (I.17)** by taking logarithms of both sides under different heating rates:

$$\ln\left(\beta_i \frac{d\alpha}{dT}\right)_{\alpha,i} = ln[f(\alpha)A] - \frac{E_\alpha}{RT_{\alpha,i}} \qquad \text{(I.21)}$$

I.5.2.2. Kissinger-Akahira-Sunose (KAS) method

Kissinger-Akahira-Sunose (KAS) method **(Kissinger, 1956; Akahira and Sunose, 1971)** linearizes **Eq (I.18)** to obtain the following expression:

$$ln\left(\frac{\beta_i}{T_{\alpha,i}^2}\right) = ln\frac{AR}{Eg(\alpha)} - \left(\frac{E_\alpha}{RT_\alpha}\right) \qquad \text{(I.22)}$$

I.5.2.3. Ozawa-Flynn-Wall (OFW) method

The Ozawa-Flynn-Wall (OFW) method **(Flynn and Wall, 1966; OzawaTakeo, 2006)** starts from **Eq (I.18)** and employs the Doyle approximation **(Doyle, 1961, 1962, 1965)** for the integral of temperature to yield,

$$\ln(\beta_i) = ln\frac{AE}{Rg(\alpha)} - 5.331 - 1.052\left(\frac{E_\alpha}{RT_\alpha}\right) \qquad \text{(I.23)}$$

I.5.3. Determination of kinetic parameters

The kinetic parameters (triplets), including activation energy (E_a), pre-exponential factor (A) and kinetic model (f(α)) of each individual process, should be determined for a complete kinetic description of the overall reaction. It is recommended to use an isoconversional (model-free) method first, which state that at constant extent of conversion the reaction rate is only a function of the temperature, to obtain the dependence of the activation energy on the extent of conversion. Application of the isoconversional method yields direct, model-free estimates of E_a, but the other two components of the kinetic triplet are still needed to fully model a reaction **(Vyazovkin *et al.*, 2011)**. Many methods have been developed based on the fundamental kinetic equation **(Eq (I.16))** to determine the kinetic parameters. The most popular methods are the Combined Kinetic Analysis and the Master plots methods.

I.5.3.1. Combined Kinetic Analysis Method

In order to obtain the kinetic parameters (f(α), E_a and A) of solid state reaction, the combined kinetic analysis method (**Pérez-Maqueda *et al.*, 2002; Pérez-Maqueda, Criado and Málek, 2003; Pérez-Maqueda, Criado and Sánchez-Jiménez, 2006; Sánchez-Jiménez *et al.*, 2009**) is commonly applied. This method is mainly based on the general kinetic equation for solid-state reactions (**Eq (I.16)**). Entering logarithms into **Eq (I.16)**, Reorganizing terms, the basic equation for the combined kinetic analysis method is obtained:

$$\ln\left(\frac{d\alpha/dt}{f(\alpha)}\right) = ln(A) - \frac{E_a}{RT} \qquad \text{(I.24)}$$

Fitting a standard linear model requires substituting various tabulated reaction models for f(α) (**Table I.1**) and selecting the one that gives the best fit.

I.5.3.2. Master plots Method

According to this method, the experimental master plot curves at different heating rates were compared with some of the most widely used solid-state kinetic models. After normalization at α = 0.5, the differential master plot equation can be expressed in the following form (**Criado, Málek and Ortega, 1989; Francisco J. Gotor *et al.*, 2000; Sánchez-Jiménez *et al.*, 2010, 2013**):

$$\frac{f(\alpha)}{f(0.5)} = \frac{d\alpha/dt}{(d\alpha/dt)_{0.5}} \frac{\exp(E_a/RT)}{\exp(E_a/RT_{0.5})} \qquad \text{(I.25)}$$

Where $T_{0.5}$, $(d\alpha/dt)_{0.5}$ and f(0.5) represent the reaction temperature, the reaction rate and the differential function of the reaction model, respectively, when α = 0.5. The experimental master plot values can be obtained for each value of α from the right-hand side of **Eq (I.25)**, using the average E_a value calculated by isoconversional method.

I.6. Conclusion

In this chapter, a brief review of piezoelectric materials with perovskite structure has been presented. The two sintering techniques used in this work, namely conventional solid-state sintering and flash sintering, were also detailed. The last part of this chapter was devoted to the description of the theoretical basis of the solid-state reaction kinetics by DSC.

Chapter II

Experimental Procedures and Characterization Techniques

II.1. Introduction

In this chapter, the various experimental approaches employed throughout this work are described in depth. It mainly concerns the preparation processes of BCT and BFO-BT polycrystalline ceramics, as well as structural, microstructural and electrical characterization techniques. The kinetic analysis procedure followed to study the calcium incorporation mechanism into $BaTiO_3$ was also described in details.

II.2. Preparation of Ceramics

In this work, the two systems investigated are barium calcium titanate ($Ba_{(1-x)}Ca_xTiO_3$) (BCT) and bismuth ferrite-barium titanate ($(1-y)BiFeO_3$-$yBaTiO_3$) (BFO-BT).

II.2.1. $Ba_{(1-x)}Ca_xTiO_3$

The first system investigated is barium calcium titanate ($Ba_{(1-x)}Ca_xTiO_3$) (BCT). The maximum level of Ca^{2+} substitution will certainly depend on the solubility limit of Ca^{2+} in $BaTiO_3$. The Ca^{2+} molar fraction (x = 15%) was chosen in this work since it is located within the range of the solubility limit of Ca^{2+} in BT that has been reported in previous studies (**Mitsui and Westphal, 1961; Schultheiß *et al.*, 2017; Zhou *et al.*, 2017; Chawla *et al.*, 2018**). Above the solubility, an insolubility region extends to 90 mol% of $CaTiO_3$, and by adding more $CaTiO_3$ (> 90 mol%), orthorhombic $CaTiO_3$ based solid solutions were formed.

II.2.1.1. Conventional Solid-State Processing Route

BCT solid solutions were prepared following the conventional solid-state synthesis route from oxide and carbonate precursor powders (**Table II.1**). The XRD patterns of the starting precursors used for the preparation of BCT are displayed in **Figure II.1**. The diffraction patterns of each sample can be indexed to $BaCO_3$ (**JCPDS#45-1471**), TiO_2 with anatase structure (**JCPDS#78-2486**) and $CaCO_3$ (**JCPDS#85-1108**).

Table II.1. Commercially available oxides and carbonates used for the synthesis of BCT.

Material	**Chemical Formula**	**Purity (%)**	**Supplier**
Barium carbonate	$BaCO_3$	≥ 98.5	Fluka Chemika
Calcium carbonate	$CaCO_3$	≥ 99	Merck EMSURE
Titanium (IV) oxide, anatase	TiO_2	≥ 99	Riedel-de Haen

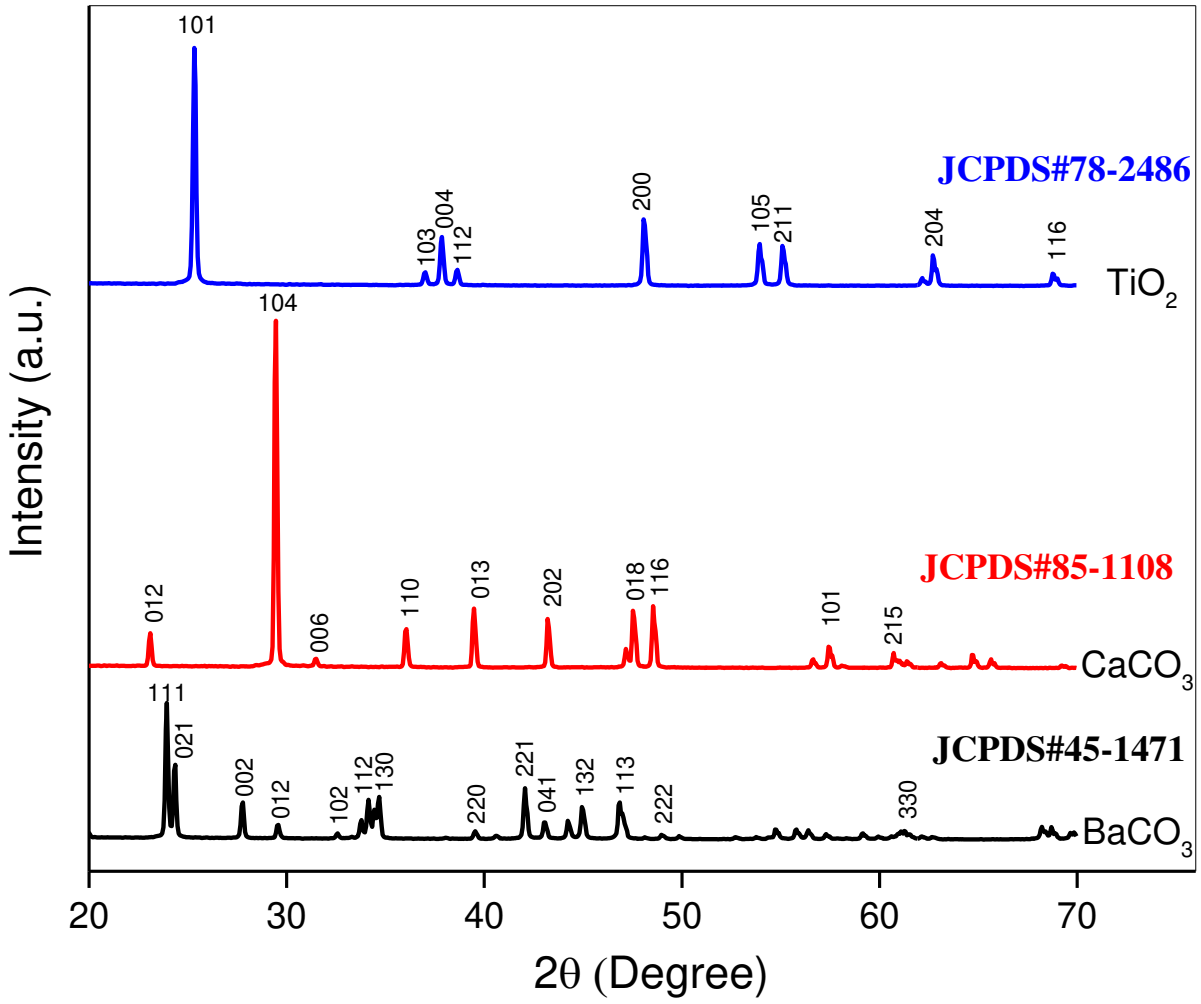

Figure II.1. XRD patterns of the starting precursors used for the preparation of the BCT system.

Figure II.2 presents the protocol for BCT preparation using the conventional solid-state synthesis method. This protocol is consistent with what has been reported in previous works (**Chen *et al.*, 2015; Sahoo *et al.*, 2019; Rashwan *et al.*, 2021**).

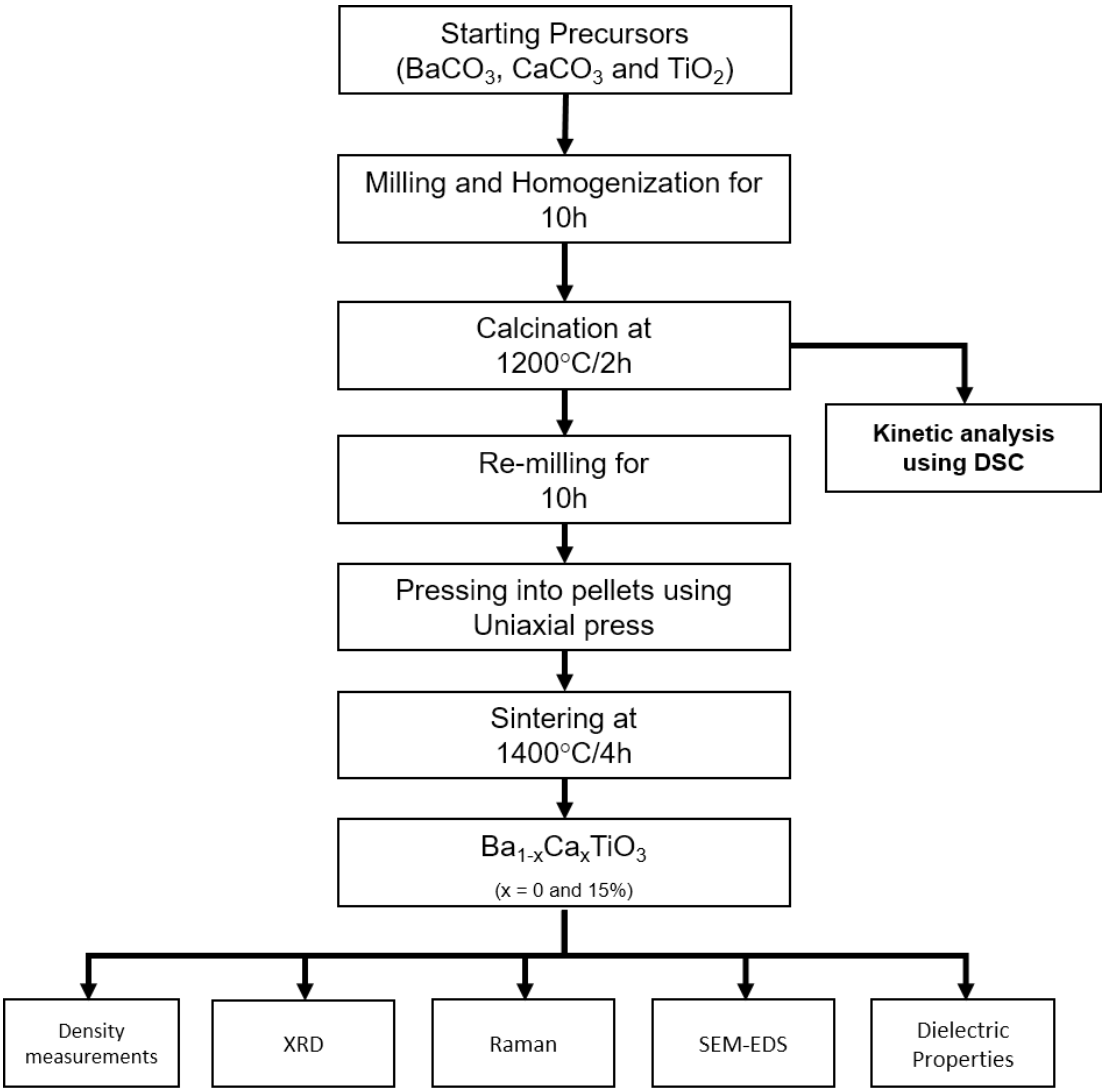

Figure II.2. Experimental procedure and characterization techniques for BCT ceramics.

Stoichiometric amounts of $BaCO_3$, $CaCO_3$, and anatase-TiO_2 were used for the preparation of $Ba_{1-x}Ca_xTiO_3$ (x = 0 and x = 0.15) solid solutions. First, the starting precursors were weighed and mixed in an agate mortar for 2 hours using ethanol as a milling medium. The obtained mixture (around 8 gr of powders) was mechanically treated for 8h in a Retsch PM100 planetary ball mill with 160 g of hardened stainless-steel balls (4.5 mm of diameter) to make the mixture fine and homogeneous and thus increasing their reactivity.

After milling, the recovered powders were dried and sieved. Part of the milled powders was used for kinetic analysis of Ca incorporation into $BaTiO_3$ and the rest was calcined in a muffle furnace at 1200 °C for 2 h under air with a heating rate of 5 °C/min. The perovskite phase is formed according to the equation: $BaCO_3 + TiO_2 \rightarrow BaTiO_3 + CO_2$ (Basic chemical reaction without dopant). The powders obtained are then re-milled under the same conditions. Once the milling is finished, the powders were dried and sieved again.

- **Pressing (Forming) and Sintering**

To perform the pressing (forming), 4 wt% polyvinyl alcohol (PVA) was added and mixed with the calcined powders as a binding agent to allow the formed pellets to maintain their cohesion during and after the pressing. The powder was formed into pellets using a uniaxial hydraulic press with a 6 mm diameter steel die and a pressure of 6 t cm^{-2}.

The formed granules are then transferred for sintering. Sintering is an essential step that allows the consolidation of the pellets with the help of heat. This consolidation allows the transfer from a powdery part to a coherent material (densification). The pellets were placed on a rectangular alumina crucible. The sintering thermal profile used is depicted in **Figures II.3**. The first step performed at 600 °C allows the decomposition of the PVA binder. The second step corresponds to the sintering temperature (1400°C) and it is maintained for 4 hours. At the end of the sintering process, dense electroceramics are obtained which can be transferred to the characterization step.

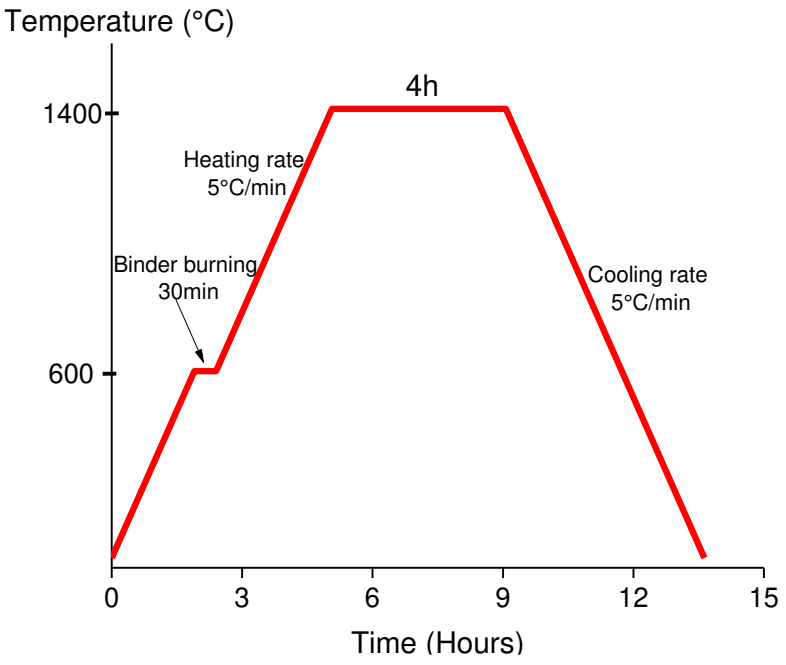

Figure II.3. BCT solid-state sintering cycle.

II.2.1.2. Kinetic Analysis Using DSC

As observed in previous works on the kinetics study of solid state reactions (**Joraid, 2007; Orava *et al.*, 2012; Ghaderi *et al.*, 2016; Mohamed *et al.*, 2018; Louaer *et al.*, 2019; Bezerra and Cabral, 2021**), the Differential Scanning Calorimetry (DSC) was used to study the reaction mechanism of the different solid transformations and calculate the main parameters. The equipment used was a TGA/DSC NETZSCH STA 449 F3 Jupiter simultaneous thermal analyzer, programmed at a continuous nitrogen flow of 20 ml/min to make the atmosphere inert.

The DSC measurement principle is displayed in **Figure II.4**. The samples were placed in a DSC crucible. The crucibles are heated from room temperature to 1000 °C. Simultaneously, the BCT mixture was calcined at various temperatures (600-1000 °C) in order to analyze the phase evolution of BCT using XRD.

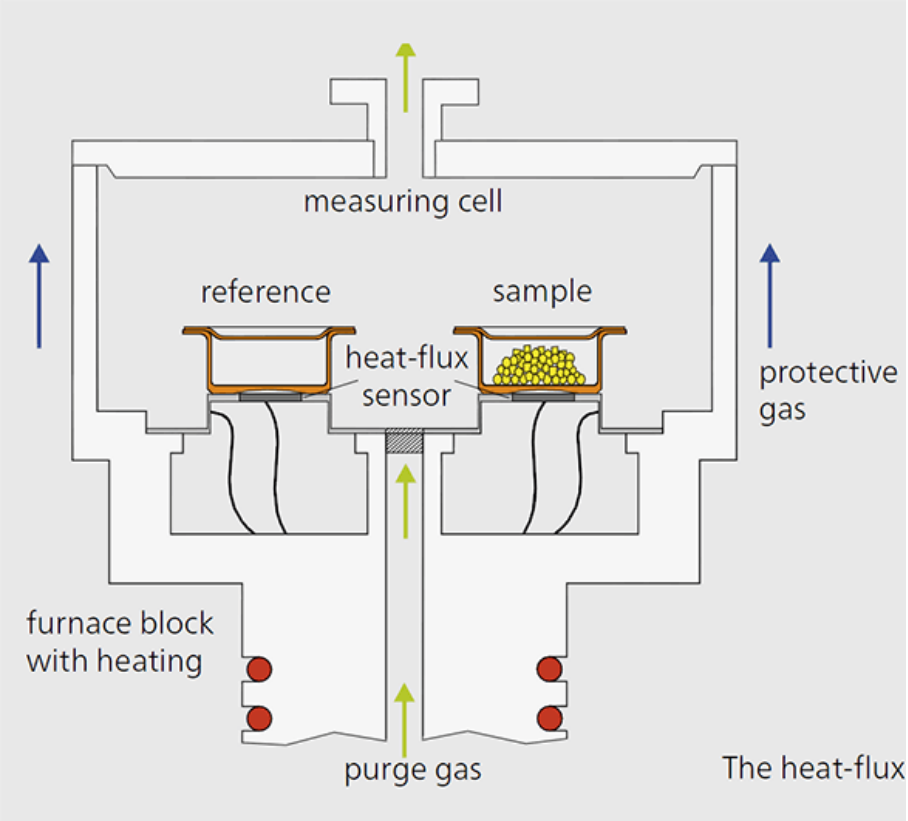

Figure II.4. DSC measurement principle.

Kinetic modeling is a mathematical procedure that allows giving an adequate explanation to experimental data. In the case of a thermal analysis, the complexity of the mechanisms involved makes the modeling difficult and delicate and requires a judicious procedure. The flowchart below (**Figure II.5**) presents the procedure followed in this thesis. The calculation and simulation were performed using Microsoft Excel 2013 and Origin lab 2015.

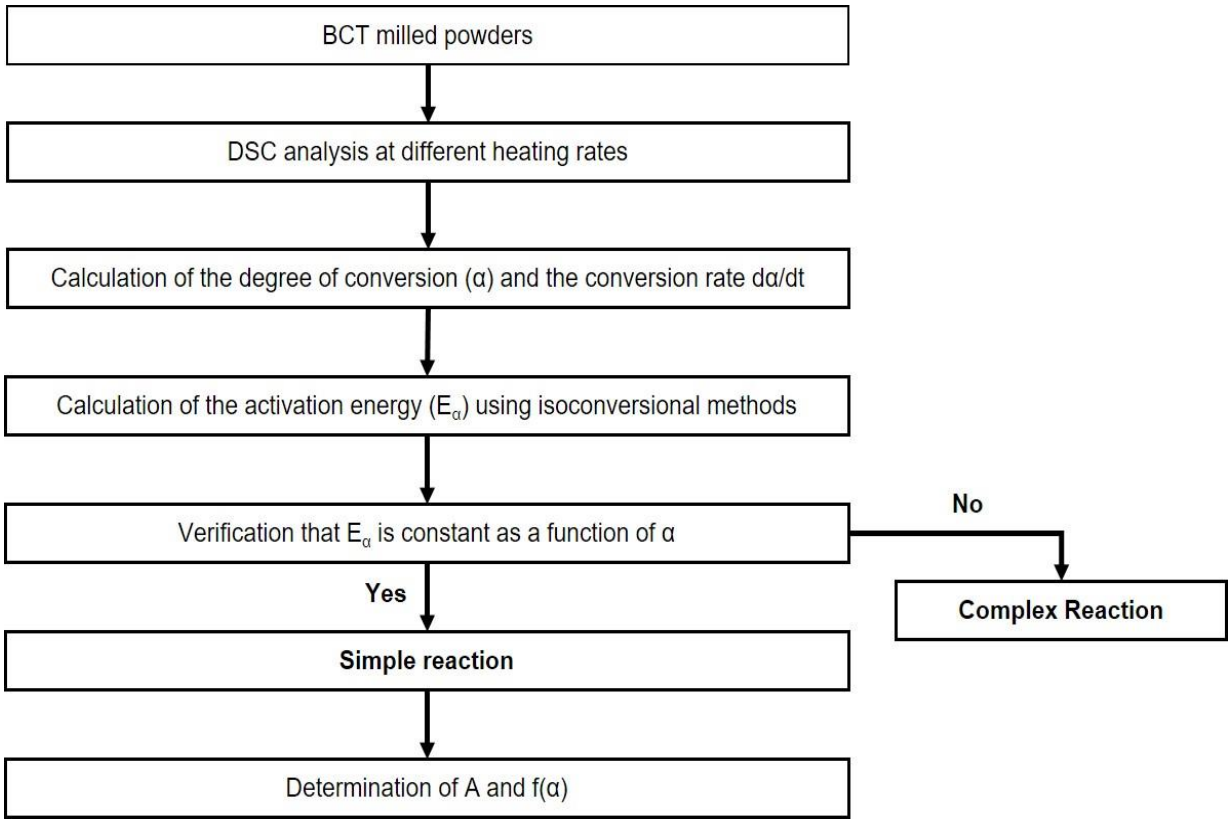

Figure II.5. Kinetic Analysis procedure followed to study the Ca incorporation mechanism.

II.2.2. (1-y)$BiFeO_3$-y$BaTiO_3$

II.2.2.1. Reactive Flash Sintering Technique

The preparation of piezoelectric ceramics based on bismuth ferrite-barium titanate, 0.67$BiFeO_3$-0.33$BaTiO_3$ (BFO-33BT), was also investigated in this work for the first time in the literature by the reactive flash sintering (RFS) method. Bi_2O_3, Fe_2O_3 and $BaTiO_3$ were used as raw materials for the preparation of BFO-BT, as specified in **Table II.2**. The XRD patterns of the starting precursors used for the preparation of BFO-BT are displayed in **Figure II.6**. The diffraction patterns of each sample can be indexed to Bi_2O_3 (**JCPDS #71-0465**), Fe_2O_3 (**JCPDS # 24-0072**) and $BaTiO_3$ (**JCPDS #31–0174**).

Table II.2. Commercially available oxides used for the synthesis of BFO-33BT.

Material	**Chemical Formula**	**Purity (%)**	**Supplier**
Bismuth (III) oxide	Bi_2O_3	≥ 99.9	Sigma-Aldrich
Iron(III) oxide	Fe_2O_3	≥ 99	Sigma-Aldrich
Barium titanate	$BaTiO_3$	≥ 99	Sigma-Aldrich

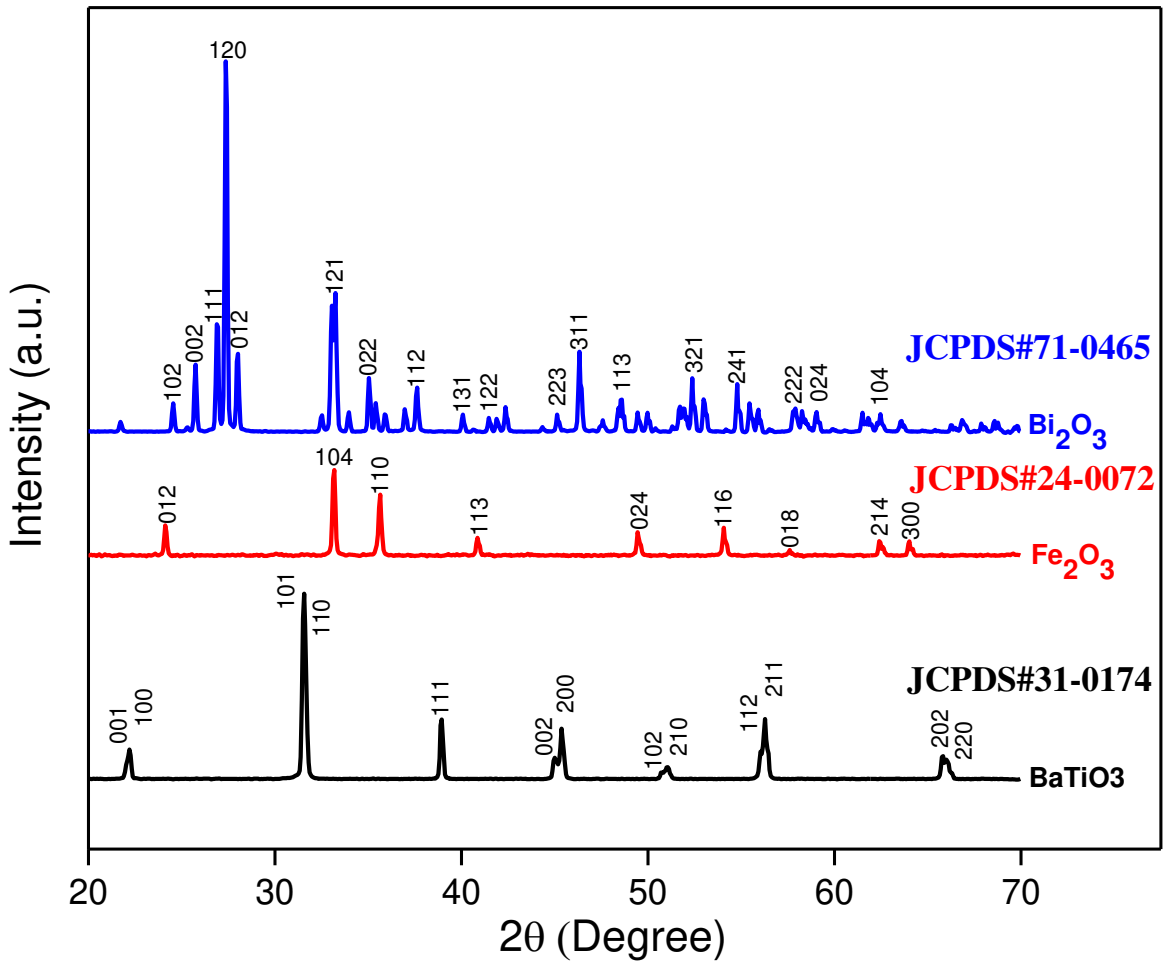

Figure II.6. XRD patterns of the starting precursors used for the preparation of the BFO-BT system.

The protocol of the preparation of BFO-33BT by reactive flash sintering technique is presented in **Figure II.7**. This preparation protocol shows its effectiveness in the preparation of many families of piezoelectric ceramics by reactive flash sintering technique such as bismuth ferrite ($BiFeO_3$) (**Gil-González *et al.*, 2018**), lead zirconate titanate (PZT) (**Jia *et al.*, 2019**), potassium sodium niobate (KNN) (**Wu *et al.*, 2020**), barium titanate ($BaTiO_3$) (**Zhu *et al.*, 2021**) and bismuth sodium titanate (BNT) (**An *et al.*, 2021**).

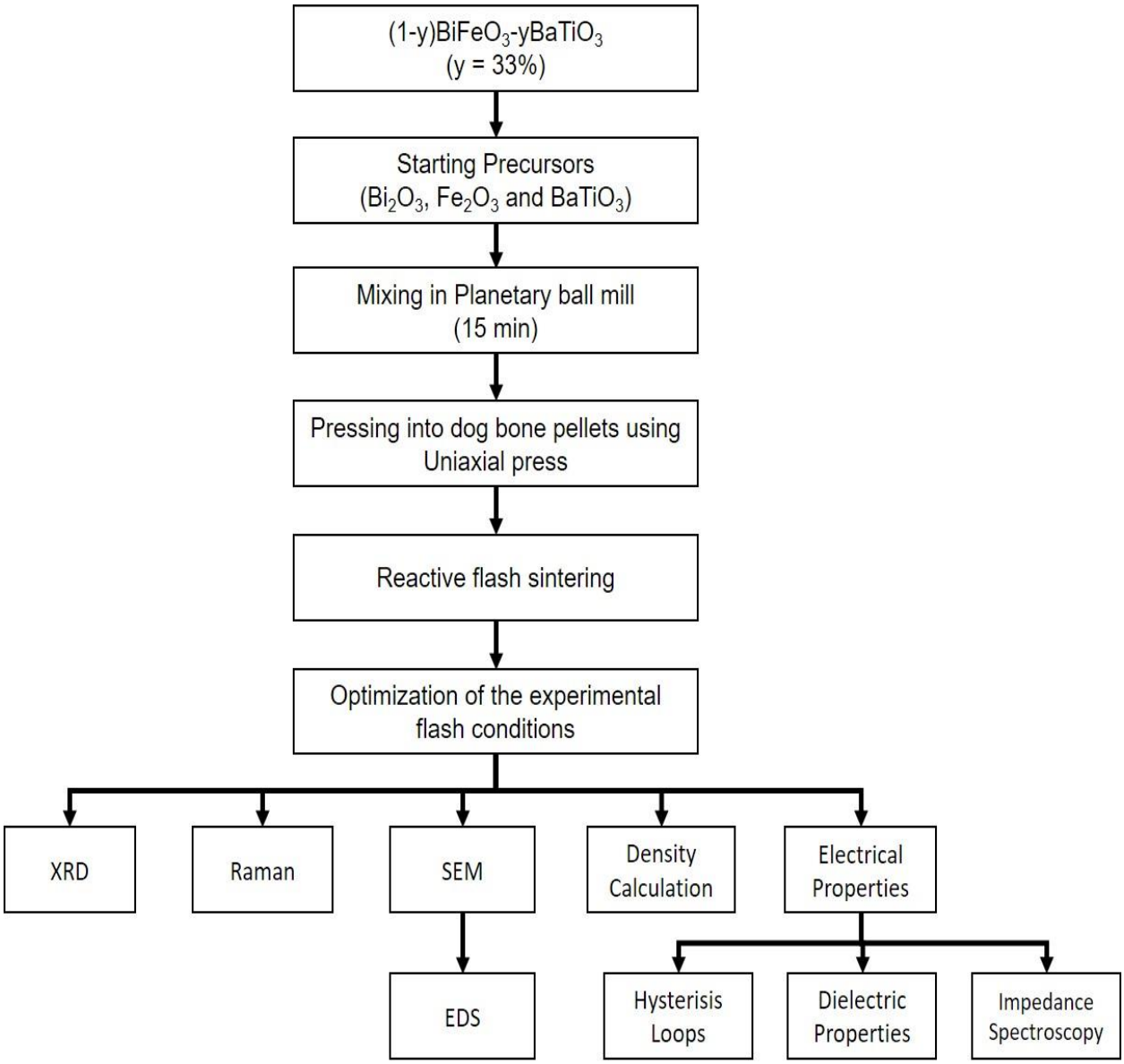

Figure II.7. Experimental procedure and characterization techniques for BFO-BT ceramics.

Stoichiometric amounts of Bi_2O_3, Fe_2O_3 and tetragonal $BaTiO_3$ were used for the preparation of (1-y)$BiFeO_3$-y$BaTiO_3$ (y=0.33) ceramics. First, the starting precursors were weighed and mixed for 15 minutes in a planetary ball mill with the objective of obtaining a homogeneous mixture. Approximately 900 mg of the powder mixture were pressed into dog-bone shaped specimens under a pressure of 500 MPa. In order to provide good contact sample electrodes, platinum paste was added into the holes of the handles of the green-body dog-bones.

The flash sintering setup used in this work is shown in **Figure II.8**. This experimental setup mainly consists of a horizontal tubular furnace allowing the heating of an internal alumina tube. The sample to be densified is placed between two platinum electrodes inside this alumina tube. The temperature of the sample was measured using a K type thermocouple placed near the sample.

The furnace temperature was linearly increased at 5 ºC min^{-1} up to the flash event. The DC electric field was applied through the two platinum wires using a 1500 W DC power supply (EA-PSI 9750–06 DT) and was maintained constant up to the point of the flash event, which was signaled by a non-linear rise in conductivity. Current and voltage input signals were recorded during the flash experiments using a Keithley 2110 multimeter. The power supply was switched from the voltage-controlled mode to current-controlled mode when the current reached the preset limit and as a result, the flash sintering event get started. The flash event was held for 30 s and the adjustment of the experimental flash conditions (applied electric field (E) and current density limit (I)) was carried out according to the protocol described in the previous work of Gil-González et al. (**Gil-González *et al.*, 2020**). This is mainly based on the selection of a working interval for the realization of the flash experiments, i.e. applied electric field (in our case E = 30-60 V cm^{-1}) and applied electric current limit (I_{max}=40-80 mA mm^{-2}), and to perform several experiments combining the values of E and I within the working interval. The selection of the optimal flash conditions is mainly based on the results obtained from the density measurements and XRD results.

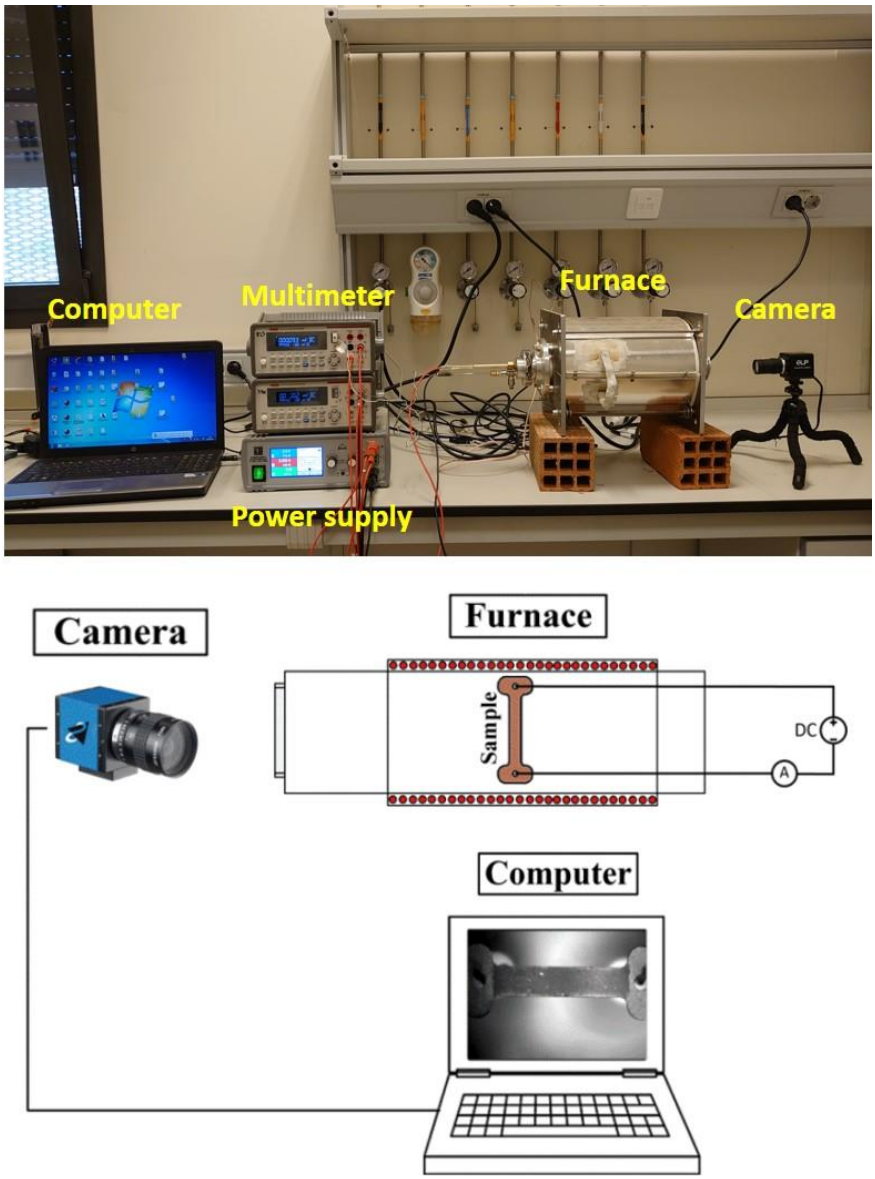

Figure II.8. Flash sintering setup and scheme.

II.2.2.2. Energy Consumption Analysis

The power analyzer PPA 1500 (Newtons4th Ltd. (N4L)), was used to measure the power consumed by the furnace during the preparation of BFO-33BT by RFS and conventional preparation method (CM). For both methods, the preparation were performed in temperature programmed tube furnace, with a heating rate of 5 °C/min.

In order to compare the energy consumption in RFS experiment with that of the conventional method, the electrical energy consumed in both processing methods was calculated. For the calculation of the electric energy, W, the following equations were used (**Eq (II.1 and II.2**)):

$$P = \frac{dW}{dt} \quad \text{(II.1)}$$

$$W = \int_{t_0}^{t} P.dt \quad \text{(II.2)}$$

where P and W respectively reflect the electric power (W) and energy (J) and t is the preparation time (s).

II.3. Density measurements

II.3.1. Archimedes' Density

The density of the ceramic samples was measured based on Archimedes' principle. An object immersed in a liquid is exposed to three forces, its weight, tension and Archimedes up-thrust. The upwards force is equal to the weight of the liquid displaced by the object. Therefore, by weighing ceramic material twice in air and then fully immersed in a known density liquid (**Figure II.9**), the density can be estimated using the following relation **Eq (II.3)**:

$$\rho_m = \frac{A}{A-B}\,\rho_L \quad \text{(II.3)}$$

where ρ_m, ρ_L, A and B are measured density of a sample, density of liquid (in our case is water), weight of a sample in air and weight of a sample in water, respectively.

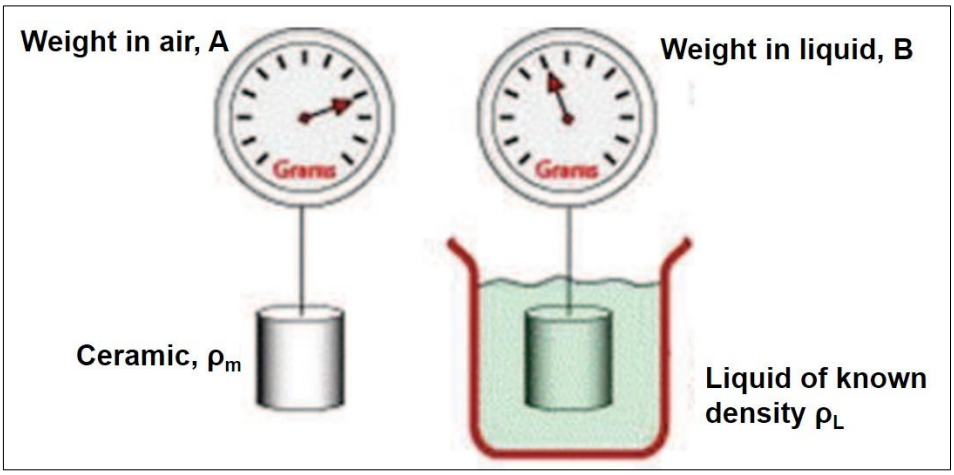

Figure II.9. Schematic presentation of the Archimedes' principle.

II.3.2. Theoretical Density

The theoretical density (ρ_{th}) of the prepared ceramic samples was calculated from the parameters extracted from the XRD data according to the following expression **Eq (II.4)**:

$$\rho_{th} = \frac{M \times Z}{V_{cell} \times N_a} \quad \text{(II.4)}$$

where M, Z, V_{cell} and N_a are the molecular weight of the ceramic system, number of formula units per unit cell, volume of unit cell, and Avogadro's number ($N_a = 6.023*10^{23}$), respectively.

II.3.3. Relative Density

The ratio between the measured density and the theoretical density is called relative density. It can be used to determine the degree of densification of ceramic materials. The following equation (**Eq (II.5)**) was used to calculate the relative density:

$$\rho_r = \frac{\rho_m}{\rho_{th}} \text{ x } 100 \qquad \text{(II.5)}$$

where ρ_r is relative density and ρ_m and ρ_{th} are respectively the measured and theoretical density.

II.4. Structural and microstructural analysis

II.4.1. X-Ray Diffraction (XRD)

X-ray diffraction is used to analyze, in a non-destructive way, the crystallographic structure of materials. It helps to check the proper formation of the perovskite phase and to study the crystal phases formed after sintering.

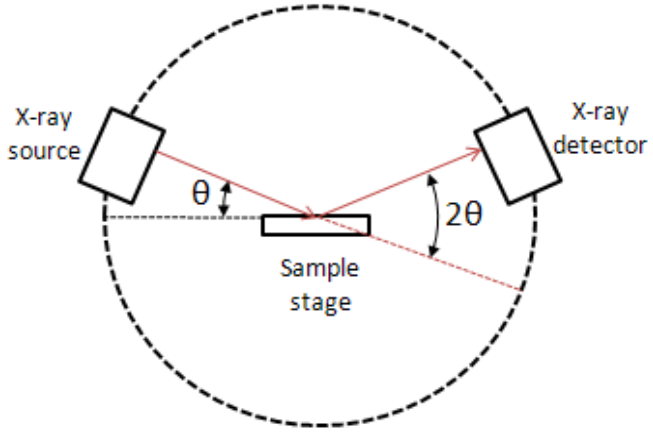

Figure II.10. Descriptive diagram of the X-ray diffractometer working principle.

For the study of the crystallographic structure and phase purity of our ceramic samples, a Rigaku MiniFlex 600 X-ray diffractometer was used, generating CuK_α radiation ($\lambda = 1.540530$ Å) and powered by a generator programmed at 40 kV and 15 mA. The working conditions were typically a scan rate of 0.02°/s in the 15°–70° 2θ range. In a normal scanning mode, the x-ray beam falls at an angle θ with the lattice planes and then is diffracted at an angle 2θ with the incident direction (**Figure II.10**). Finally, the intensity of the diffracted beam is recorded as a function of 2θ.

II.4.2. Raman Spectroscopy

Raman spectroscopy is a method to characterize the molecular composition and structure of materials. Raman scattering results from the interaction of light and matter and allows access to molecular and crystal vibrations (phonons). The «Raman» technique consists in focusing (with a lens) a monochromatic light beam on the sample to be studied and to analyze the scattered light. Excitation of light may use monochromatic ultraviolet (UV), visible (Vis) and near infrared (NIR) radiation (**Dukor, 2006**). The big part of the incident photons is transmitted, reflected or absorbed and a much smaller fraction is scattered at the same frequency ν_0 as the incident radiation, it is the Rayleigh scattering (elastic scattering) or with change of frequency, it is the Raman scattering (inelastic scattering) (**Figure II.11**).

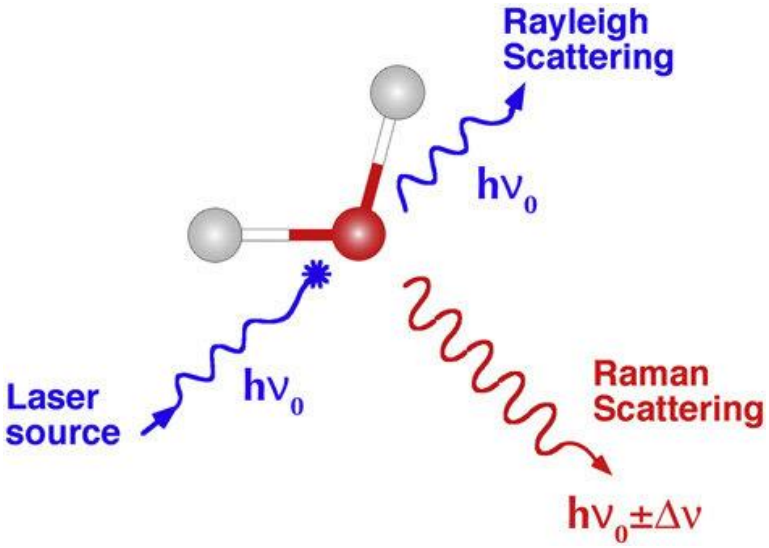

Figure II.11. A simple schematic of the different scattering and fluorescence processes: Rayleigh scattering (blue) and anti-Stokes Raman scattering (red) (**Marcelli *et al.*, 2012**).

During our study, we used a Horiba Jobin-Yvon LabRam HR800 Raman spectrometer available in the ICMS (Institute of Materials Science of Seville-Spain), which allows the obtaining of high-resolution spectra. The Raman spectrometer working principle is displayed in **Figure II.12.**

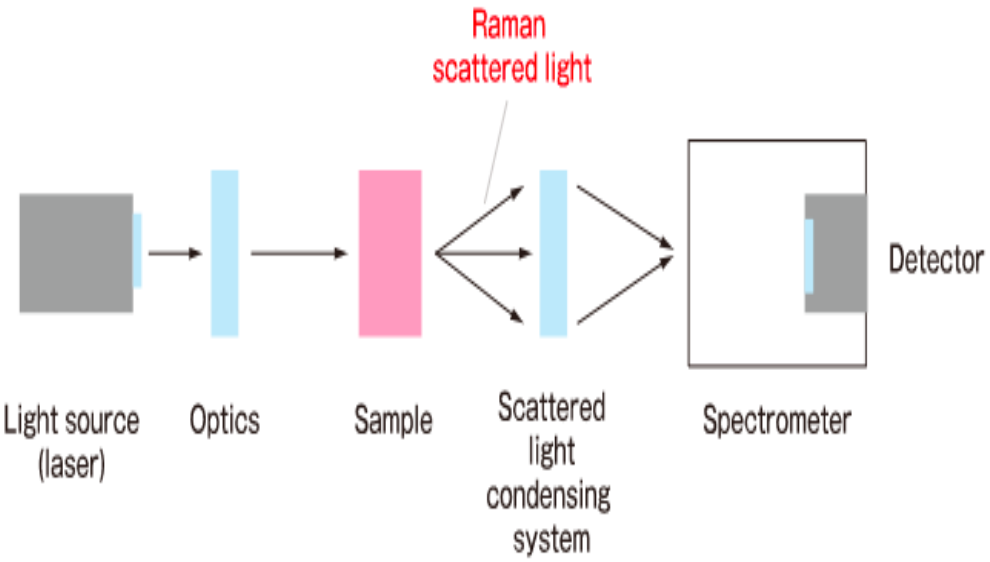

Figure II.12. Schematic of Raman spectrometer working principle.

To excite the sample, laser radiation was used. In this work, green laser excitation (wavelength = 532 nm) was used because it is one of the most commonly used laser types for inorganic materials and Raman resonance experiments.

II.4.3. Scanning Electron Microscopy (SEM)

In the study of ceramics, the microstructure is a key element that allows a better understanding of the various parameters influencing the properties of the material. To observe this, the ceramic samples are first polished and then a thermal quenching is performed at a temperature equal to about 90% of the sintering temperature to ambient air. This step reveals the microstructure by cracking the grain boundaries due to the internal mechanical stresses undergone by the ceramic during the sudden temperature change.

The microstructure is observed by scanning electron microscope (Hitachi S-4800), equipped with an energy dispersive X-ray spectrometer (EDS). This imaging technique consists in scanning the surface of the sample by a beam of electrons focused on it. The electrons then interact with the atoms of the surface, which allows the emission of different particles depending on the nature of the interaction. We can then distinguish, according to their energy, the back scattering electrons (BSE), the secondary electrons (SE) and characteristic X-ray as shown in **Figure II.13**. The different photographs were then obtained by using either the back scattering electrons, which correspond to the electrons of the incident beam having interacted elastically with the sample, or the secondary electrons, products of the inelastic interaction of the electrons of the incident beam with the sample.

After the ejection of a secondary electron, the matter returns to its equilibrium state by emission of a photon X. These photons are characteristic of each element and can be detected by an EDS detector. This technique is the Energy Dispersive X-ray spectrometry (EDS) and allows an analysis of the different chemical elements present in the sample.

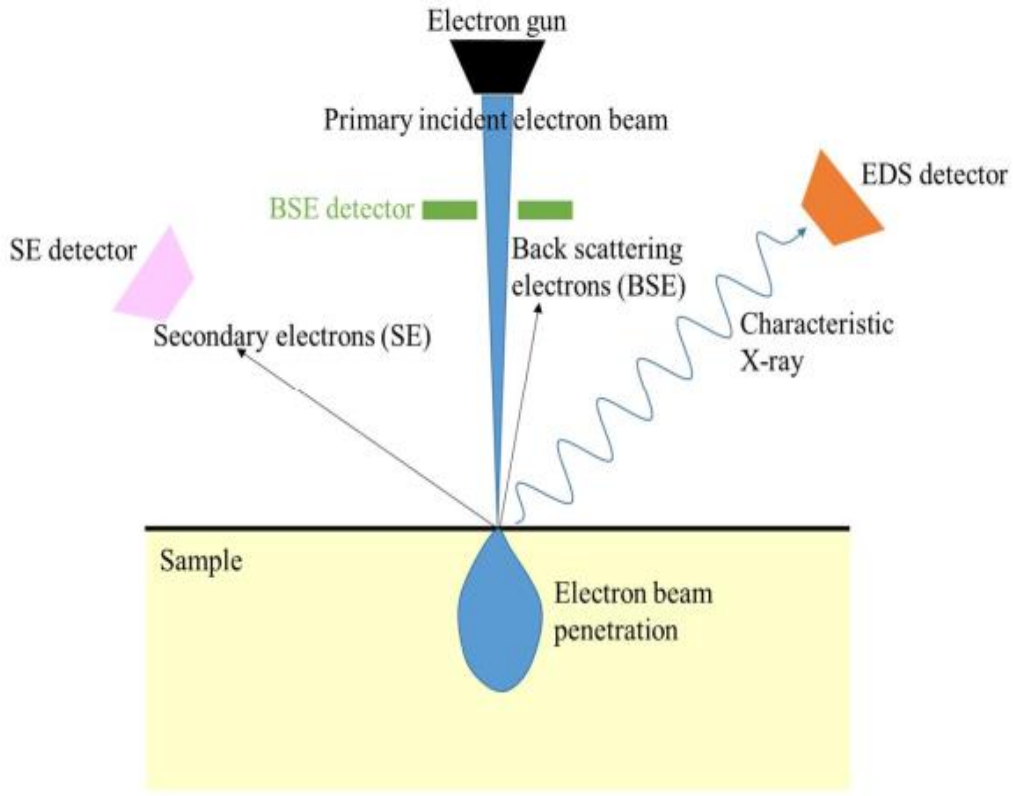

Figure II.13. Schematic diagram of the working principle of a Scanning Electron Microscope.

II.5. Electrical Measurements

II.5.1. Dielectric Permittivity (ε') and Dielectric Loss (tanδ)

In order to be able to measure the electrical properties of the sintered pellets, the latter were coated on both sides with silver paste and then fired at 550 °C for 10 minutes. The schematic diagram for the dielectric measurement of the ceramic pellets is shown in **Figure II.14**. The dielectric properties were measured from 100 Hz to 1 MHz using an Agilent E4980A Precision LCR Meter (L = Inductance, C = Capacitance, and R = Resistance). The silver-coated ceramic samples were placed in a tube furnace as presented in **Figure II.18**. The LCR meter and the temperature controller were connected to the computer in order to automate the measurement and to record the temperature inside the furnace.

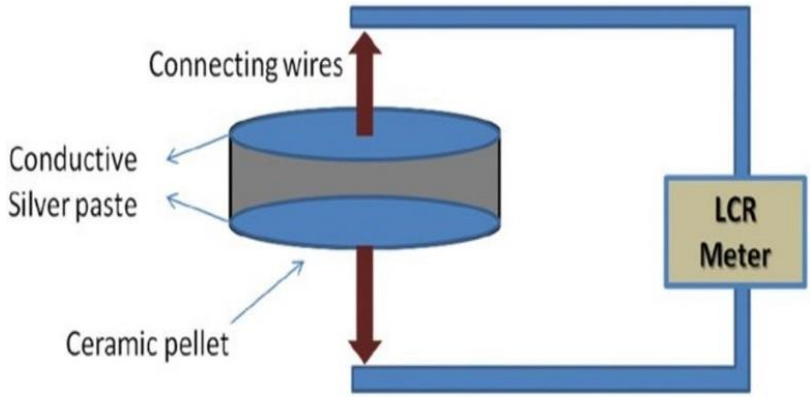

Figure II.14. Schematic diagram of the pellet for dielectric measurements.

The measured values are the temperature of the furnace, the capacitance (C_p) as well as the dielectric loss (tanδ) at 100 Hz, 1 KHz, 10 KHz, 20 KHz, 100 KHz and 1 MHz. The C_p and tanδ values were measured in the temperature range of 30-160 °C for the BCT samples and in the temperature range of 30-600 °C for the BFO-BT sample with a furnace heating rate of 5 °C/min. Using the measured values of C_p, it is possible to calculate the relative permittivity ε' according to the following formula (**Coelho and Aladenize, 1993**):

$$\varepsilon' = \frac{C_p * d}{\varepsilon_0 * A} \qquad \text{(II.6)}$$

where ε_0 is the permittivity of vacuum ($8.84 * 10^{-12}$ F m^{-1}), d the thickness of the sample and A is the surface of the electrode.

The thermal evolution of the dielectric permittivity exhibits a discontinuity at T_C that practically results in maximum in the paraelectric domain. The dielectric constant (ε') follows a Curie-Weiss law of the following form:

$$\frac{1}{\varepsilon'} = \frac{T - T_0}{C_w} \qquad \text{(II.7)}$$

where T_0 denotes the Curie-Weiss temperature and C_w is the Curie-Weiss constant.

The Curie-Weiss temperature can be determined by plotting the inverse of the dielectric permittivity (1/ ε') versus temperature. It is reported that the values of T_C-T_0 reflect phase transition order, namely T_C-T_0 > 0 indicates a first-order transition where the thermal variation of the permittivity is discontinuous, while T_C-T_0=0 belongs to a second-order transition characterized by continuous thermal variations of the permittivity.

The modified Curie-Weiss law is an empirical expression proposed by K. Uchino and Nomura (**Uchino and Nomura, 2011**) to characterize also the dielectric dispersion and diffusivity of the phase transition in complex ferroelectric materials. It is written in the following form:

$$\frac{1}{\varepsilon'} - \frac{1}{\varepsilon'_{max}} = \frac{(T-T_{max})^{\gamma}}{C'_w} \qquad 1 < \gamma < 2 \qquad \text{(II.8)}$$

where γ is the diffuseness constant, C'_w is the modified Curie-Weiss constant and T_{max} is the temperature corresponding to the ε'_{max}. The phase transition's characteristics are determined by γ values. γ=1 denotes a "normal" ferroelectric phase transition, whereas γ=2 denotes a "complete" diffuse phase transition (DPT).

II.5.2. Impedance spectroscopy (IS)

Impedance spectroscopy (IS) is generally used to characterize dielectric materials. This technique consists in applying to the terminals of a material an alternative voltage in a wide range of frequency. Through the resulting current, the impedance of the sample is deduced. The results can be analyzed according to four complex formalisms: the impedance Z^*, the electric modulus M^*, the permittivity ε^* and the admittance Y^* given by the following expressions (**Macdonald, 1992; Sinclair and West, 1998**):

$$Z^* = Z' - jZ' \qquad \text{(II.9)}$$

$$\left.\begin{aligned} M^* &= j\omega C_0 Z^* = j\omega C_0 (Z' - jZ'') = \omega C_0 Z'' + j\omega C_0 Z' \\ M' &= \omega C_0 Z'' \\ M'' &= \omega C_0 Z' \\ C_0 &= \varepsilon_0 \frac{A}{d} \end{aligned}\right\} \qquad \text{(II.10)}$$

$$\left.\begin{aligned} \varepsilon^* &= \frac{1}{M^*} = \frac{1}{M' + jM''} = \frac{1}{\omega C_0} * \frac{Z'' - jZ'}{(z')^2 + (Z'')^2} \\ \varepsilon' &= \frac{1}{\omega C_0} * \frac{Z''}{(z')^2 + (Z'')^2} \\ \varepsilon'' &= \frac{1}{\omega C_0} * \frac{Z'}{(z')^2 + (Z'')^2} \end{aligned}\right\} \qquad \text{(II.11)}$$

$$\left.\begin{aligned} Y^* &= \frac{1}{Z^*} = \frac{1}{Z' - jZ''} = \frac{Z' + jZ''}{(Z')^2 + (Z'')^2} \\ Y' &= \frac{Z'}{(Z')^2 + (Z'')^2} \\ Y'' &= \frac{Z''}{(Z')^2 + (Z'')^2} \end{aligned}\right\} \qquad \text{(II.12)}$$

where (Z", M", ε", Y") and (Z', M', ε', Y') are imaginary and real components, $j = \sqrt{-1}$, ω and C_0 represent the angular frequency (rad.s^{-1}) and the capacitance of the sample with no material between the plates, respectively.

In order to analyze and better interpret the experimental results, it is necessary to have an equivalent circuit model showing a realistic representation of the electrical properties. In the ideal case of a homogeneous material and neglecting the effects of electrodes, a parallel RC circuit can model the electrical properties. The total impedance is:

$$Z^*(\omega) = \frac{R}{(1+ R^2C^2\omega^2)} - j\left[\frac{R^2C\omega}{(1+ R^2C^2\omega^2)}\right] \qquad \text{(II.13)}$$

The Nyquist diagram, which plots the imaginary part $Z'' = Im(Z^*(\omega))$ against the real part $Z' = Re(Z^*(\omega))$ of the complex impedance, is the most commonly used graphical representation (**Schmidt, 2007**). The Nyquist representation and the Z"/M" vs Log (f) spectroscopic graph of a parallel RC circuit are shown in **Figure II.15** and **Figure II.16**.

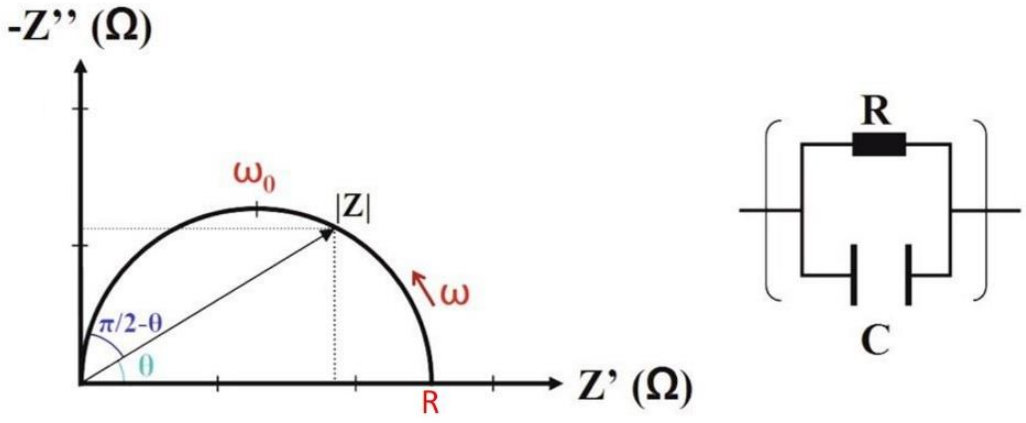

Figure II.15. Nyquist representation of a parallel RC circuit.

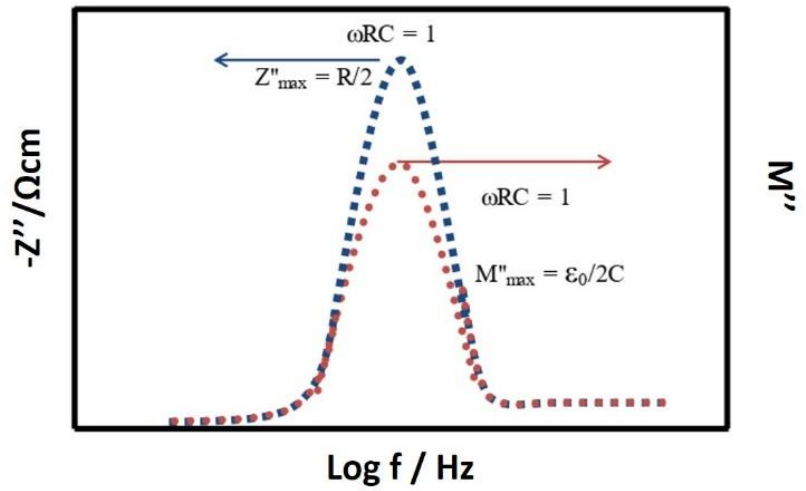

Figure II.16. Z" and M" spectroscopic graphs of imaginary impedance components

The frequency variation of the complex impedance is presented as a semicircle in the Nyquist plane. Since the imaginary part is always negative (**Eq (II.13)**), we represent the impedance's imaginary part as (-Z") for simplicity. Different values appear on this diagram:

- The intersection of the semicircle with the real axis gives the value of the model resistance:

$$\lim_{\omega\to\infty}[Z'(\omega)] = 0 \quad \text{et} \quad \lim_{\omega\to 0}[Z'(\omega)] = R \qquad \text{(II.14)}$$

- The modulus |Z| of the complex impedance is obtained by connecting the origin to any point of the circle.
- The frequency f_0 (or pulsation ω_0) at the maximum of the imaginary part of the complex impedance is an important characteristic and corresponds to the relaxation time of the dipole τ, expressed by the relation:

$$\tau = \frac{1}{2\pi f_0} = \frac{1}{\omega_0} \qquad \text{(II.15)}$$

A more complex circuit consisting of two parallel RC elements in series is usually used for an inhomogeneous material that contains grain and grain boundary impedances, as shown in **Figure II.17**.

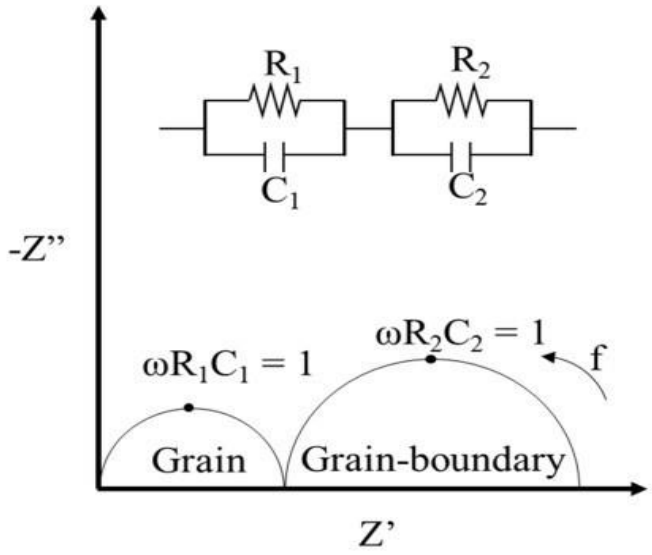

Figure II.17. Possible equivalent circuit of the dielectric consisting of two types of components and the complex impedance plot.

where R_1 and C_1 are the grain's resistance and capacitance, respectively, and R_2 and C_2 are the grain-boundary resistance and capacitance, respectively.

Temperature-dependent impedance measurements can be used to calculate the activation energy for conduction in each electro-active region of a sample. The conductivity values (σ) (obtained from Z* plot intercepts) for each electro-active region at different temperatures can be plotted in conventional Arrhenius format:

$$\sigma = \sigma_0 \, e^{\left(-\frac{E_a}{K_b T}\right)} \qquad \text{(II.16)}$$

where σ_0, E_a and K_b are respectively the pre-exponential factor, activation energy, and Boltzman constant ($8.617343*10^{-5}$ eV K^{-1}). Using logarithms and rearranging the **Eq** (**II.16**):

$$\log(\sigma) = \log(\sigma_0) - \frac{E_a}{K_b T} \qquad \text{(II.17)}$$

The slope of the log (σ) versus 1/T plot can be used to calculate the E_a for conduction for each electro-active region of the samples.

In this work, data are presented in several ways, as Z" vs Z', Z"/M" vs log (f), and log C' vs log (f). The Impedance Analyzer (PMS 1735 Newtons4th Ltd, Loughborough (UK)) was used to measure the impedance of sintered pellets, over a frequency range from 100 Hz to 1 MHz, using an AC measuring voltage of 0.1 V and a 360–440 °C temperature range. The measurements were made while taking into account the blank capacitance and the overall geometry of the pellets, which had previously been silver-coated on both sides. **Figure II.18** shows the setup employed to carry out the measurements.

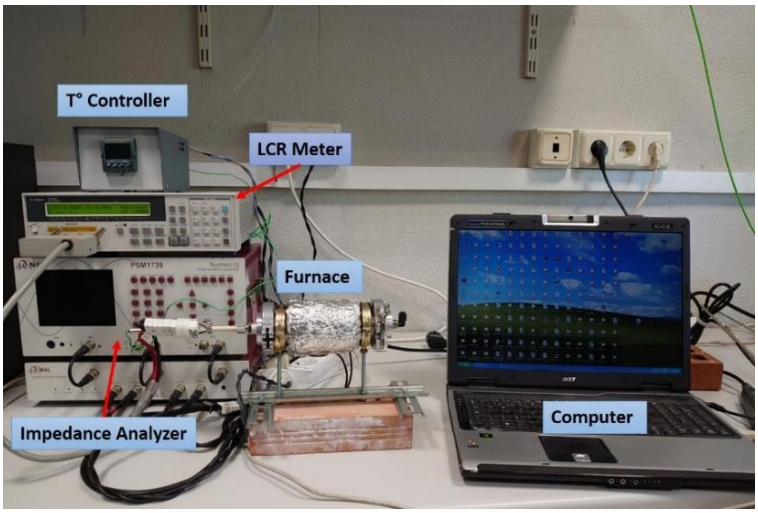

Figure II.18. Dielectric characterization and impedance analysis setup.

II.6. Ferroelectric and Piezoelectric Properties

II.6.1. Ferroelectric Hysteresis Measurements

The ferroelectric and piezoelectric properties of the BFO-BT ceramic sample were measured at room temperature in collaboration with the group of Caracterització elèctrica de materials i dispositius (CEMAD) of the Universitat Politècnica de Catalunya (Barcelona, Spain). Electric field-induced polarization (P-E) hysteresis loops were measured in a typical Sawyer-Tower configuration (**Figure II.19**) by applying a sinusoidal electric field of amplitude of 60 kV cm^{-1} at a frequency of 1 Hz, using a Hewlett-Packard 33120A signal generator and a Trek 663 signal amplifier, at room temperature. The electric field-induced macroscopic strain was measured by adding a WayCon inductive position transducer conditioning with a Solartron OD5 Module to the P-E setup.

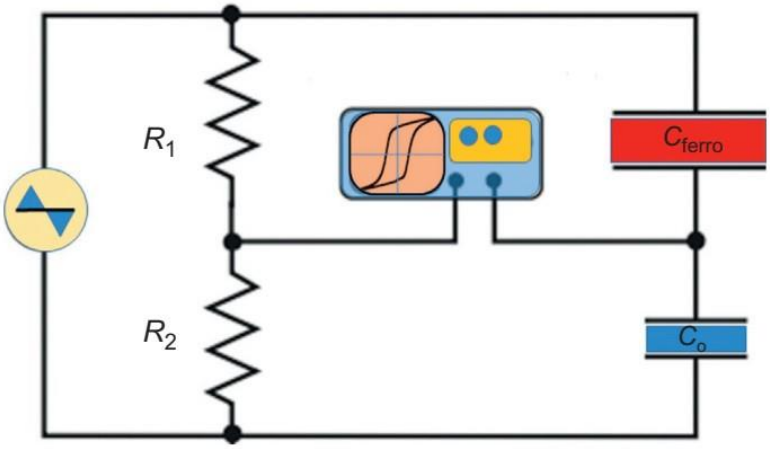

Figure II.19. Sawyer-Tower circuit for the measurement of P-E loops (**Gupta, 2021**).

The sample, which is placed between two electrodes, is assimilated as a plane capacitor of capacity (C_{ferro}). This "capacitor" is connected in parallel with a reference capacitor of known capacity C_0 (with $C_0 >> C_{ferro}$). The voltage across a plane capacitor is given by:

$$V = \frac{Q}{C} \quad \text{(II.18)}$$

The charge stored by two capacitors connected in series is identical:

$$Q = C_0 * V_0 = C_{\text{ferro}} * V_{\text{ferro}} \quad \text{(II.19)}$$

In addition, the total charge density D for a ferroelectric medium is given by:

$$D = \varepsilon_0 E + P \quad \text{(II.20)}$$

where P is the material polarization, E is the electric field, and ε_0 is the dielectric permittivity of vacuum ($8.84 * 10^{-12}$ F m^{-1}). From the point of view of orders of magnitude, $\varepsilon_0 E$ is negligible compared to P. Therefore, the total charge density can be written as follows:

$$P \approx D = \frac{Q}{A} \quad \text{(II.21)}$$

where A is the area of the measured ferroelectric sample. Thus, the polarization can be written as follows:

$$P = \frac{C_0 * V_0}{A} = \frac{C_{\text{ferro}} * V_{\text{ferro}}}{A} \quad \text{(II.22)}$$

The parameters C_0 and A being known, the measurement of the voltage V_0 gives access to the polarization.

Furthermore, since $C_0 >> C_{\text{ferro}} \Rightarrow V_0 << V_{\text{ferro}} \Rightarrow$ the voltage across the ferroelectric material is much larger than the voltage across the capacitor C_0, i.e. that it is of the same order of magnitude as the total voltage:

$$V = V_0 + V_{\text{ferro}} \approx V_{\text{ferro}} \quad \text{(II.23)}$$

This is why, when the voltage V is swept from V_{max} to $V_{min} = -V_{max}$, it can be considered that V_{ferro} sweeps the same range of values. The measured polarization value is represented by a hysteresis cycle for ferroelectric materials.

In practice, the charge Q that is proportional to the polarization is established by integrating the switching current I that flows through the measured ferroelectric sample.

$$P = \frac{Q}{A} = \frac{1}{A}\int_{t_1}^{t_2} I dt \quad \text{(II.24)}$$

II.6.2. Piezoelectric Property Measurements

To analyze the piezoelectric properties, the samples were subjected to a DC electric field of 60 kV cm^{-1} and then poled in a silicone bath at 80 °C for 30 minutes and subsequently aged for two days before measurements were taken in order to prevent the influence of aging processes (**IEEE Standard on Piezoelectricity, 1988**). A d_{33} PiezoMeter (PM3500, KFC Technologies, Inc., USA) was used to determine the piezoelectric constant d_{33} at room temperature. The working principle of a quasi-static d_{33} meter is presented in **Figure II.20**.

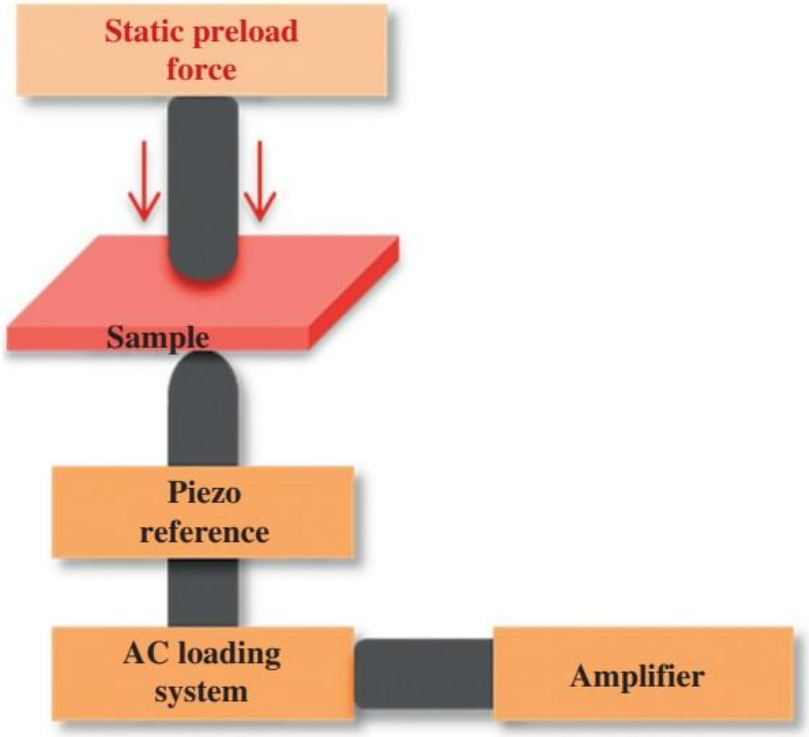

Figure II.20. The working principle of a quasi-static d_{33} meter.

The following expression was used to calculate the d_{33} of the BFO-BT ceramic sample:

$$d_{33} = -\frac{C_S V}{F} \qquad \text{(II.25)}$$

where C_s, F and V are the sample capacitance, applied force and response voltage, respectively. C_s is defined as:

$$C_s = \frac{\int_A \varepsilon_{33} dA}{d} \qquad \text{(II.26)}$$

where A is the sample's area, d and ε_{33} are respectively its thickness and permittivity.

II.7. Conclusion

This chapter describes in detail the various preparation and characterization techniques for BCT and BFO-BT piezoelectric ceramic materials. It outlines the various techniques employed during this project. First, the processing methods used in this thesis to prepare BCT and BFO-BT ceramic materials were presented, namely the conventional solid-state processing method (for BCT) and the flash sintering technique (for BFO-BT). The kinetic analysis method used to investigate the mechanism of Ca incorporation in BCT was also described. The techniques used for structural and microstructural characterization, such as DRX, Raman, SEM, EDS…, were then explained. Finally, all the experimental techniques and setups used to perform the electrical characterization, i.e. dielectric, piezoelectric and ferroelectric properties, of the prepared ceramic samples were presented.

In the following chapters, we will present the various results obtained using these experimental methods and characterization techniques.

Chapter III

Study of the Incorporation Mechanism of Ca into $BaTiO_3$

III.1. Introduction

As stated in section **I.3.3.1**, the A-site partial substitution of $BaTiO_3$ has been widely employed, not only for stabilizing the tetragonal (T) phase but also for improving the electrical properties of $BaTiO_3$. The partial substitution of Ba^{2+} with alkaline earth cations, such as Ca^{2+}, leads to the formation of barium calcium titanate, $Ba_{1-x}Ca_xTiO_3$ (BCT), solid solution. BCT solid solutions have received extensive attention as a lead-free ferroelectric material. The calcium incorporation leads to a modest change in Curie temperature (T_c). In contrast, it improves the stability of the piezoelectric properties (**Zhu, Zhang and Chen, 2013**). In BCT system, the piezoelectric coefficient has been enhanced from 190 up to 310 pC/N (**Fu, Itoh and Koshihara, 2008**). Furthermore, the incorporation of Ca^{2+} into BT decreases the probability of the formation of undesirable non-ferroelectric hexagonal phase (**Mazon *et al.*, 2005**). These properties make BCT a very suitable and promising compound for various commercial applications, such as multi-layer ceramic capacitors (MLCCs) and electro-optical devices (**Yoon and BurtrandI.Lee, 2002; Motta *et al.*, 2010**). Many studies have been found in the literature on the effect of Ca addition in $BaTiO_3$ on the electrical properties of $BaTiO_3$ such as dielectric, piezoelectric and ferroelectric properties (**Araújo *et al.*, 2014; Al-Taie, Al-Shakarchi and Kamel, 2018; Ahmadi, Kharaziha and Labbaf, 2019; Rashwan *et al.*, 2021**). However, the existing literature about the study of the mechanism of the incorporation of Ca^{2+} into $BaTiO_3$ is quite limited and important discrepancies can be found.

Kinetic analysis of solid-state reactions is essential to understand many transformations in solids and provides the essential kinetic parameters, in order to design and optimize the processes at an industrial scale and to establish the processes conditions (**Brown *et al.*, 2000**). The kinetics of solid-state reactions are frequently studied by thermal analysis techniques, i.e., differential thermogravimetry (DTG) (**Aghili, Panjepour and Meratian, 2017**), differential thermal analysis (DTA) (**Prasad and Varma, 2005; Erol, Küçükbayrak and Ersoy-Meriçboyu, 2009**) and differential scanning calorimetry (DSC) (**Prasad and Varma, 2005; Erol, Küçükbayrak and Ersoy-Meriçboyu, 2009; Gil-González *et al.*, 2018; Louaer *et al.*, 2019; Taibi *et al.*, 2019**), X-ray diffraction (XRD) methods (**Bots *et al.*, 2012; Gil-González *et al.*, 2018**), microscopic techniques (**M. Winseck *et al.*, 2016**) and rheology (**Orava *et al.*, 2012**).

In this chapter, the non-isothermal kinetics analysis of Ca^{2+} incorporation into $BaTiO_3$ to form BCT is investigated using DSC technique. The material employed for this study, $Ba_{0.85}Ca_{0.15}TiO_3$ (abbreviated as BCT15), is fabricated through the solid-state synthesis route.

In BCT15, the Ca^{2+} molar fraction (15%) was chosen since it is related to $(Ba_{0.85}Ca_{0.15})(Zr_{0.10}Ti_{0.90})O_3$ (commonly named BCZT) lead-free piezoelectric material that has acquired a huge attention due to its enormously high piezoelectric coefficient (d_{33} = 620 pC/N) according to the results reported by Liu and Ren (**Liu and Ren, 2009**).

III.2. Thermal Behavior and Phase Formation of BCT15 Solid Solution

In order to study the thermal behavior of the BCT solid solution, approximately 20 mg of the BCT powder mixture was used to perform the thermal analysis of BCT. It should be noted that the sample was previously dried at 100°C for two hours.

The thermal behavior of BCT15 was studied using DSC/TG instrument from 70-1000 °C at a heating rate of 10 °C/min. The obtained DSC/TG curves are displayed in **Figure III.1**. The TG curve reveals an overall weight loss of approximately 13.8 %, which is divided into three stages. A weight loss of 3.2 % was first observed between 500 and 680 °C, which corresponds to two DSC endothermic peaks. The first peak, at around 534 °C, is associated to the formation of thin layer of $BaTiO_3$ on the surface of TiO_2 (**Eq (III.1)**) (**Liu and Ren, 2009**) and the second one, at around 662 °C, is caused by the decomposition of $CaCO_3$ as mentioned in **Eq (III.2)**. Another 2.2 % weight loss occurred in the 680-800 °C temperature range which could be assigned to the formation of Ba_2TiO_4 during the reaction between $BaTiO_3$ and $BaCO_3$ (**Eq (III.3)**) (**Liu and Ren, 2009**). Finally, in the temperature range from 800-1000 °C, the TG curve shows the highest weight loss (8.4 %) appended by two endothermic peaks at 810 and 893 °C. The first peak was attributed to the phase transition (from γ to β) of $BaCO_3$ (**Templeton and Pask, 1959**) and the second one is related to the solid-state reaction between Ba_2TiO_4 and the remaining TiO_2 oxides and formation of barium titanate through **Eq (III.4)** and is attributed also for the reaction between the unreacted $BaCO_3$ and TiO_2 (**Hassan *et al.*, 2014**).

$$BaCO_3 + TiO_2 \rightarrow BaTiO_3 + CO_2 \qquad \text{(III.1)}$$

$$CaCO_3 \rightarrow CaO + CO_2 \qquad \text{(III.2)}$$

$$BaCO_3 + BaTiO_3 \rightarrow Ba_2TiO_4 + CO_2 \qquad \text{(III.3)}$$

$$Ba_2TiO_4 + TiO_2 \rightarrow 2BaTiO_3 \qquad \text{(III.4)}$$

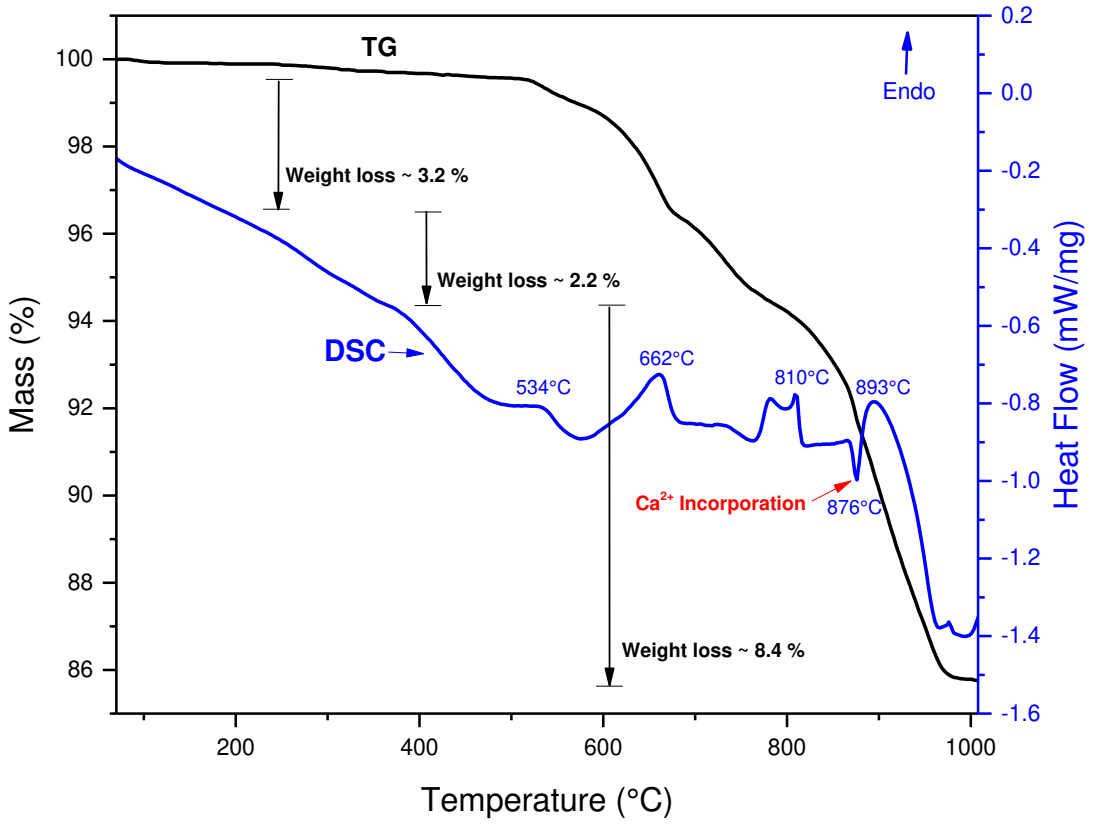

Figure III.1. DSC/TG curves of the as ground BCT15 powders at heating rate of 10 °C/min.

Besides the previous findings, a single DSC exothermic peak is observed at around 876 °C. This peak can be attributed to the incorporation of Ca^{2+} into $BaTiO_3$ to form BCT. The latter corroborates the ideas of Shu et al (**Shu, Reed and Button, 2015**), who suggested that the incorporation of Ca^{2+} into $BaTiO_3$ to form BCT, take place after the formation of $BaTiO_3$. As a confirmation step, the DSC curves of pure $BaTiO_3$ (pure-BT) and Ca-doped $BaTiO_3$ (BCT15) are compared (**Figure III.2**). The exothermic peak at around 876 °C is observed for the BCT15 while this peak is not observed for pure-BT, which proves its association in the incorporation process of Ca^{2+} into BT.

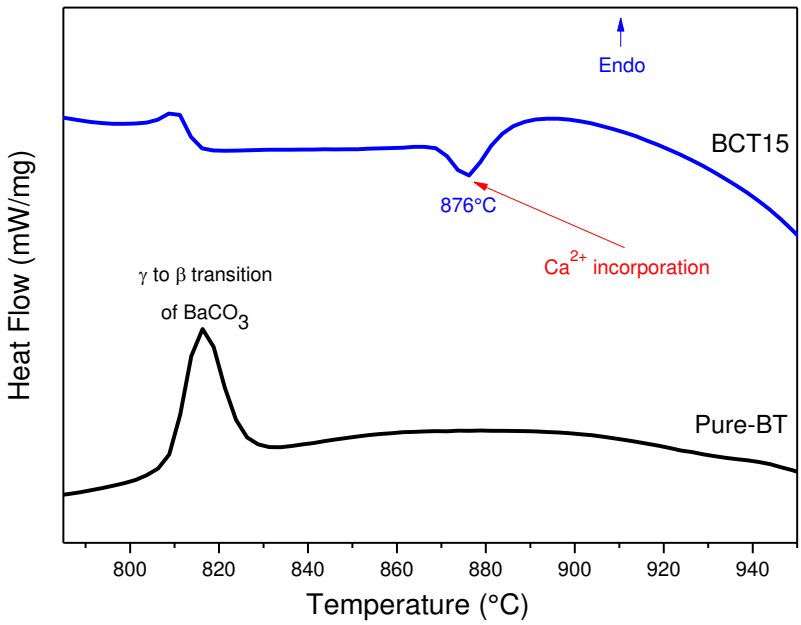

Figure III.2. DSC curves of pure (pure-BT) and Ca-doped $BaTiO_3$ (BCT15).

Figure III.3 shows the XRD results for BCT15 mixture calcined at different temperatures (600-1000 °C). At 600°C, a small amount of BT phase (2θ = 31.5°) already appeared with unreacted $BaCO_3$ and TiO_2. Significant decreases in $BaCO_3$ and TiO_2 phases were detected at 800 °C. Alongside, the intensity of the BT phase dramatically increased with appearance of a small amounts of Ba_2TiO_4 at 2θ = 28.4° and 2θ = 28.9° (**JCPDS 38-1481**). At the same calcination temperature, A Bragg peak assigned to Orthorhombic $CaTiO_3$ is observed at 2θ = 33.1° (**JCPDS 42-0423**). As the temperature increased to 900 °C, the intensity of the BT phase was further enhanced followed by a decrease of Ba_2TiO_4 and $CaTiO_3$ phases. At 1000 °C, no secondary phase was revealed and a pure cubic BT phase (**JCPDS 31-0174**) was achieved, indicating that Ca^{2+} may have entered into the $BaTiO_3$ lattice to form a solid solution. This result is consistent with those obtained by DSC/TG analysis.

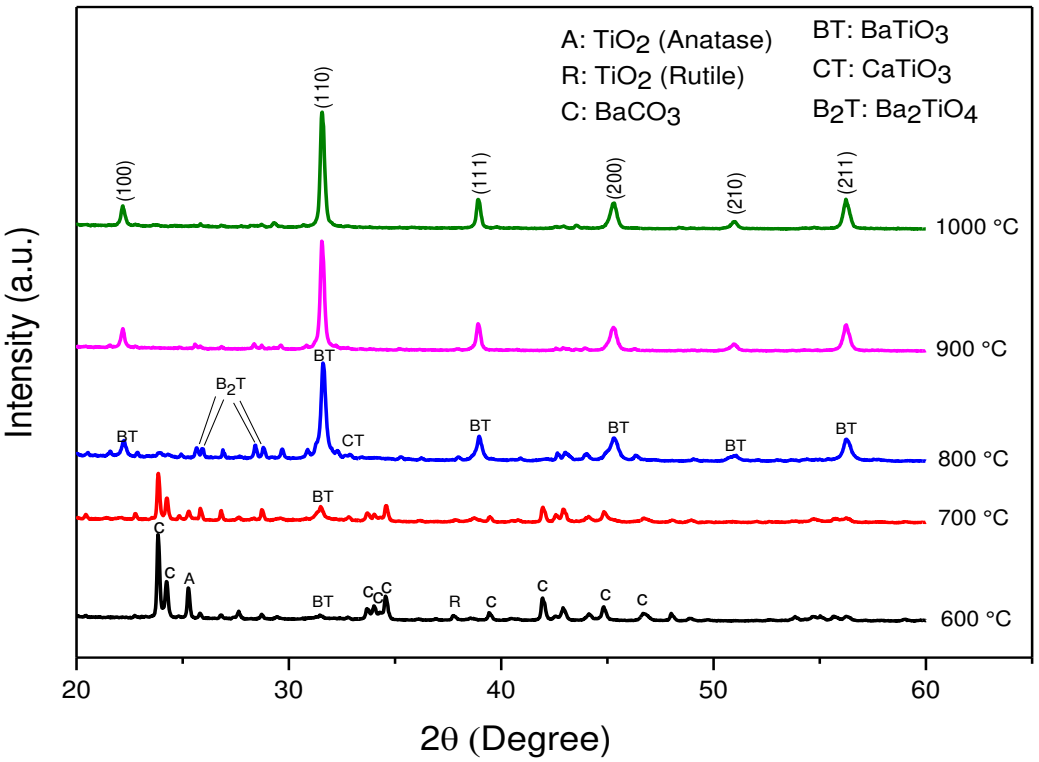

Figure III.3. XRD patterns of BCT15 samples calcined in the temperature range between 600-1000 °C.

The Scherrer's equation (**Moghtada, Moghadam and Ashiri, 2018**) can be used based on the XRD patterns to calculate the BCT15 average crystallite size:

$$D = \frac{0.9\lambda}{\beta cos\theta} \qquad \text{(III.5)}$$

where D is the average crystallite size, λ is the wavelength of X-ray (1.54056 Å), β is the full width at half-maximum intensity (FWHM) and θ is the diffraction angle. The BCT15 estimated average crystallite size based on the lattice plane (110) was found to be approximately 36 nm.

The SEM micrograph of BCT15 sample calcined at 1000 °C for 2 hours are presented in **Figure III.4**. It is visible that the grains have spherical to irregular morphologies and form agglomerates of different sizes. The average grain sizes of the selected sample are found to be around 0.9 – 2.6 µm. The average grain size is larger than the average crystallite size determined earlier by the Scherrer's equation from the XRD data. This can be explained by the fact that the grains are constructed through combination of several crystallites.

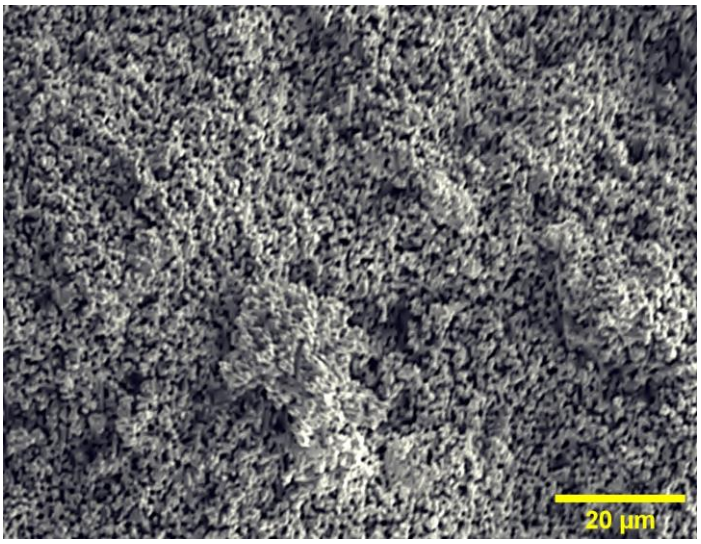

Figure III.4. SEM micrograph of the BCT15 sample heated at 1000 °C for 2 h.

III.2.1. Non-Isothermal Kinetics Analysis

The kinetics study of incorporation was performed from the DSC exothermic peaks corresponding to the incorporation of Ca^{2+} into $BaTiO_3$ to form BCT (**Figure III.5 (a, b)**) obtained at multiple heating rates (β = 3, 5, 10 and 20 °C.min^{-1}). The values of the incorporation peak temperature (T_p) at different heating rate are displayed in **Table III.1**.

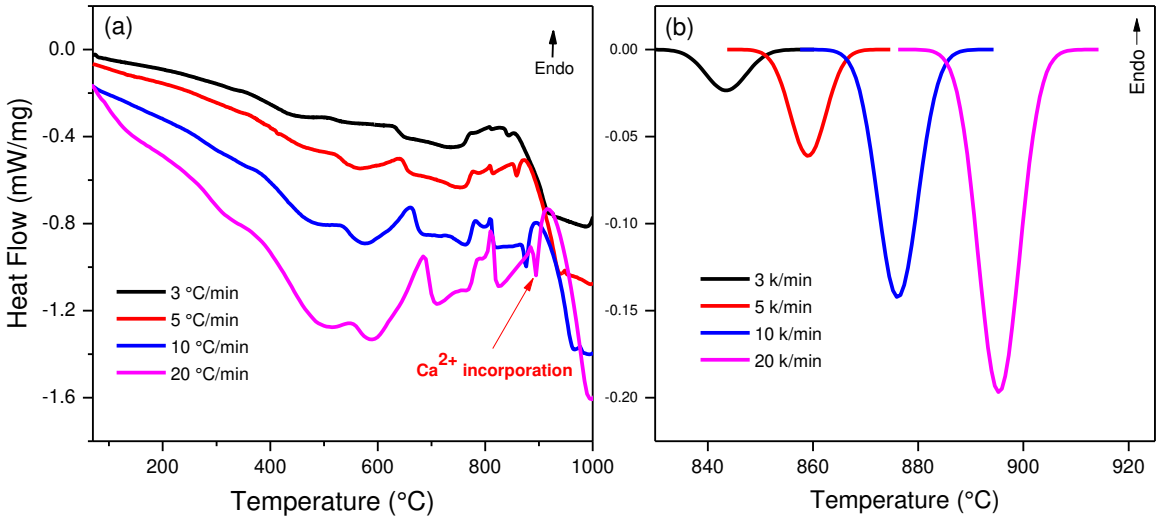

Figure III.5. (a) DSC experimental curves **(b)** DSC incorporation curves registered at different heating rates (β = 3, 5, 10 and 20 °C/min).

Table III.1. The values of the incorporation peak temperature (T_p) at the heating rate β= 3, 5, 10 and 20 K/min for BCT15 solid solution.

Heating rate (K/min)	Peak Temperature (°C)
3	843
5	859
10	876
20	896

From DSC data, the extent of conversion α was calculated as a ratio of the current heat change, ΔH, to the total heat, ΔH_{tot}, based on **Eq (I.14)**. The α-T curves at various heating rates are shown in **Figure III.6 (a)**. The reaction rates (dα/dt) were then obtained by differentiating the α-T plots with respect to the time (**Figure III.6 (b)**).

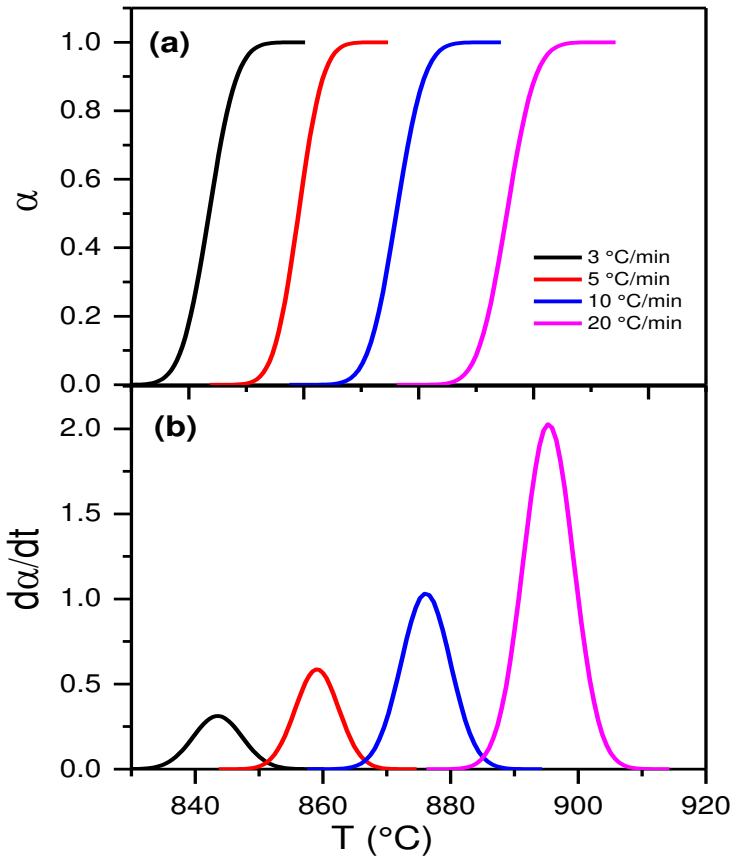

Figure III.6. Experimental **(a)** α-T and **(b)** dα/dt-T plots corresponding to the incorporation mechanism recorded at different heating rates (β = 3, 5, 10 and 20 °C/min).

III.2.2. Determination of Activation Energy

The non-isothermal apparent activation energy of the incorporation mechanism was estimated as a function of α via isoconversional methods. As a first step, the original Kissinger's equation (**Kissinger, 1956**) is applied to calculate the apparent activation energy that corresponds to the maximum rate of the process.

III.2.2.1. Kissinger Method

The original Kissinger's equation is applied in order to estimate the apparent activation energy of the incorporation mechanism without any previous assumption and accurate on the reaction model by the following equation:

$$ln\frac{\beta}{T_p^2} = -\frac{E_a}{RT_p} + const \qquad \text{(III.6)}$$

Figure III.7 presents the Kissinger straight line for the incorporation process. According to **Eq (III.6)**, the resulting E_a value for the incorporation process is 381 kJ/ mol.

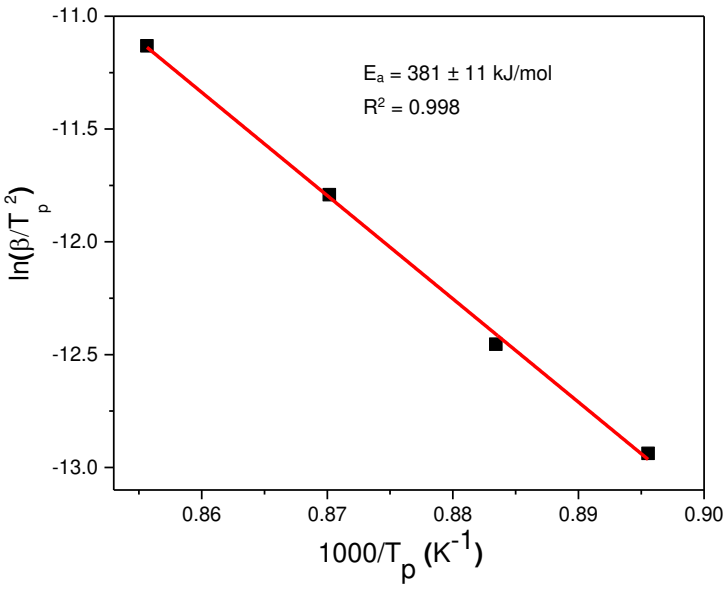

Figure III.7. Kissinger linear fit of $\ln(\beta/T_p^2)$ versus $1000/T_p$ for the incorporation mechanism.

III.2.2.2. Isoconversional Methods

Isoconversional methods such as FR, KAS and OFW, were applied to determine the apparent activation energy of the incorporation mechanism as a function of α. **Figure III.8** shows the plot of the left-hand side of **Eqs (I.21)**, **(I.22)** and **(I.23)** as a function of $1000/T_\alpha$ for the FR, KAS and OFW isoconversional methods, respectively.

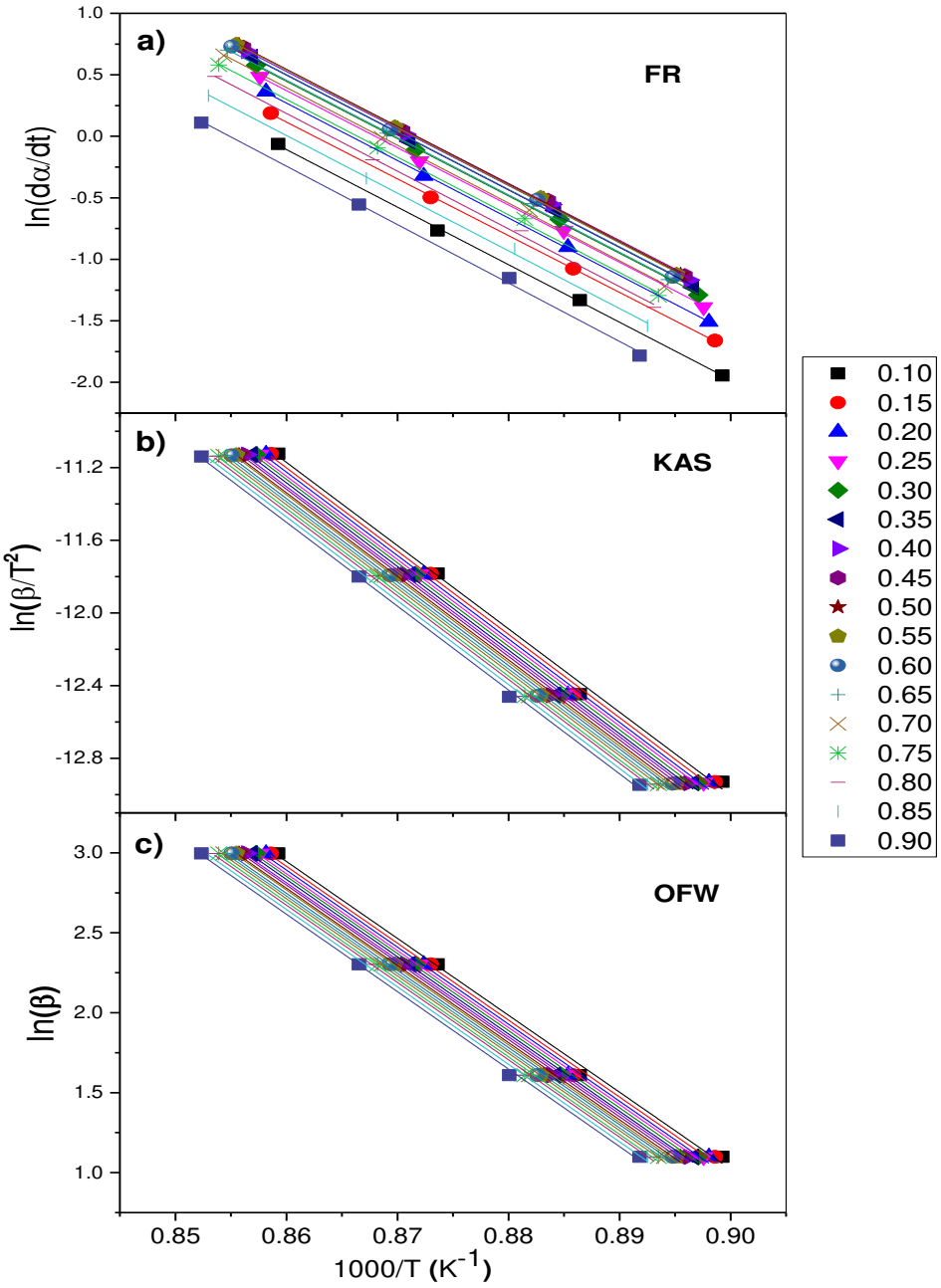

Figure III.8. Isoconversional plots as a function of α: **a)** FR, **b)** KAS and OFW.

The apparent activation energy of the incorporation process can be determined from the slope of the plots. The results are summarized in **Table III.2** and displayed in **Figure III.9** in the conversion α range from 0.1-0.9 with a step-size of 0.05 as mentioned by Vyazovkin et al (**Vyazovkin *et al.*, 2011**) in ICTAC Kinetics Committee recommendations. It can be observed that E_α is clearly constant during the whole process for the three isoconversional methods, with average values of 388, 382 and 401 kJ/mol for the FR, KAS and OFW isoconversional methods, respectively. These results suggest that the incorporation of Ca^{2+} into BT to form BCT15 is carried out through a single step.

Table III.2. Apparent activation energy values obtained from FR, OFW and KAS isoconversional methods for the incorporation mechanism.

α	FR		OFW		KAS	
	E_α (KJ/mol)	R^2	E_α (KJ/mol)	R^2	E_α (KJ/mol)	R^2
0.10	389	0.999	400	0.995	381	0.995
0.15	384	0.999	400	0.995	381	0.995
0.20	388	0.999	401	0.995	382	0.995
0.25	387	0.999	400	0.996	381	0.996
0.30	387	0.999	401	0.996	382	0.996
0.35	388	0.998	402	0.996	383	0.996
0.40	385	0.999	400	0.997	381	0.996
0,45	385	0.999	401	0.997	382	0.996
0.50	388	0.999	401	0.997	382	0.996
0.55	389	0.998	402	0.997	383	0.997
0.60	388	0.998	401	0.997	382	0.997
0.65	388	0.998	402	0.997	383	0.997
0.70	390	0.998	402	0.997	383	0.997
0.75	390	0.998	402	0.997	383	0.997
0.80	390	0.998	402	0.998	383	0.998
0.85	390	0.998	403	0.998	384	0.998
0.90	395	0.997	403	0.998	384	0.998
Average (KJ/mol)	$E_\alpha = 388 \pm 7$		$E_\alpha = 401 \pm 12$		$E_\alpha = 382 \pm 12$	

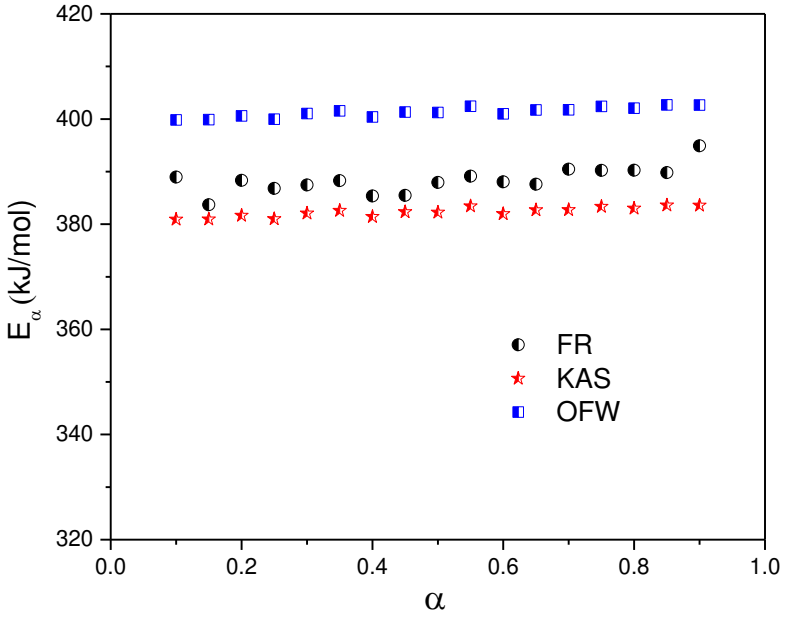

Figure III.9. Stability of apparent activation energy E_α in the conversion α range from 0.1-0.9 using Friedman, OFW and KAS isoconversional methods.

III.2.3. Determination of Kinetic Parameters

In order to obtain the kinetic parameters (f(α), E_a and A) of the incorporation mechanism of Ca^{2+} into $BaTiO_3$, the combined kinetic analysis method was applied.

Figure III.10 (a-f) displays the combined kinetic analysis plots of the left-hand side of **Eq (I.24)** versus 1000/T after assuming the most common theoretical kinetic models found in the literature (**Table I.1**). It can be observed that the entire kinetic data at different heating rates for $\alpha = 0.1–0.9$ is fitted ideally by the Avrami-Erofeev (A3) kinetic model (**Figure III.10 (d)**), giving a correlation coefficient R^2 value of 0.998. The average E_a and A values, obtained from the plot slope and intercept, were found to be equal to 388 kJ/mol and 4.1×10^{17} min^{-1}, respectively. The obtained E_a value is similar of that calculated by Friedman (388 kJ/mol) method than those obtained by OFW (401 kJ/mol) and KAS (382 kJ/mol) isocoversional methods. This can be interpreted by the fact that the Friedman method commonly provides the most reliable results compared to other isoconversional methods (**Burnham and Dinh, 2007**).

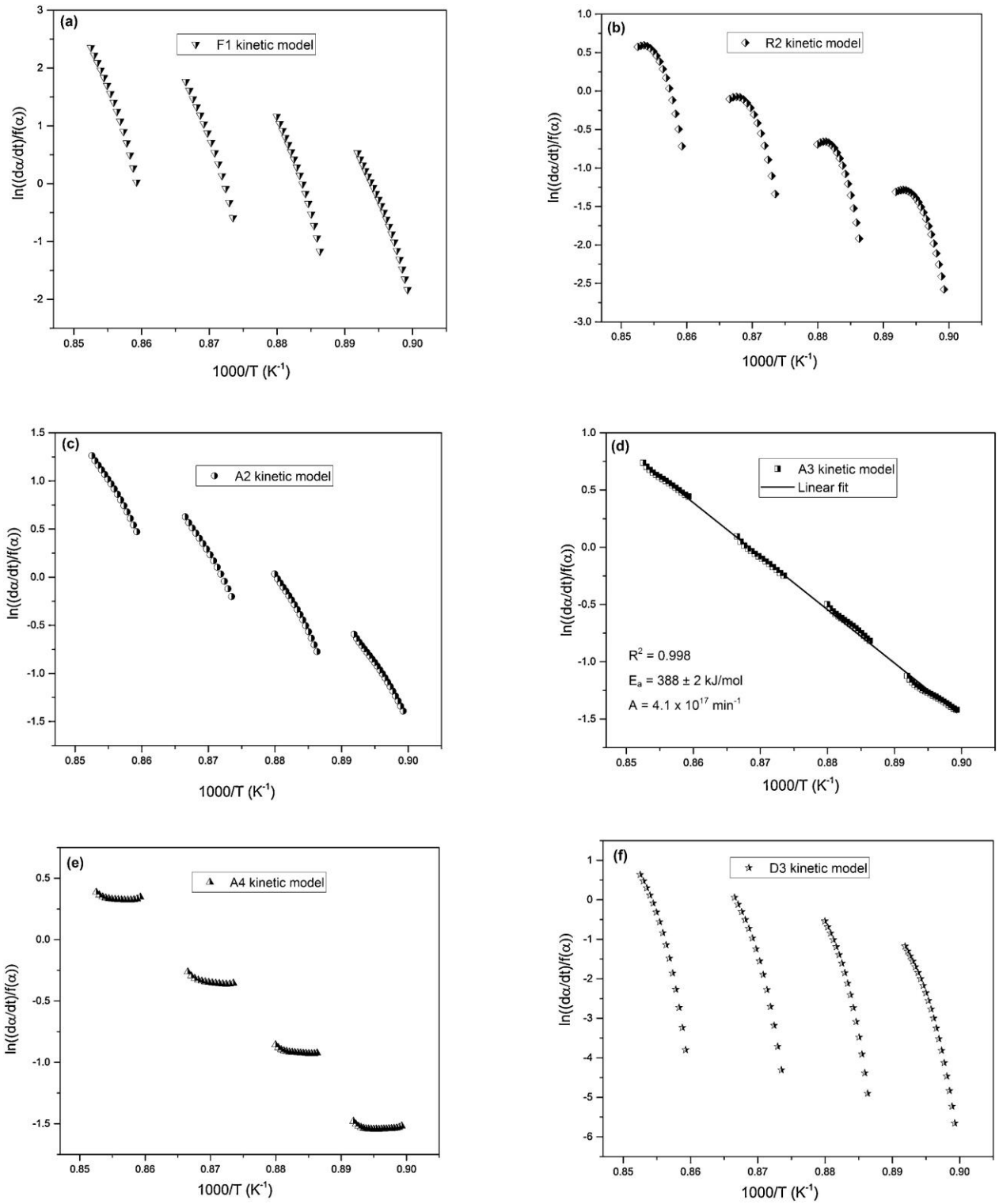

Figure III.10. Combined analysis plots by means of **Eq (I.24)** for the incorporation mechanism after assuming different solid-state kinetic models: **a)** F1, **b)** R2, **c)** A2, **d)** A3, **e)** A4 and **f)** D3.

The obtained kinetic model for the incorporation mechanism was then confirmed by employing the differential master plot method (**Eq (I.25)**). According to this method, the experimental master plot curves at different heating rates (β = 3, 5, 10 and 20 °C/min) were compared with some of the most widely used solid-state kinetic models (**Table I.1**).

The experimental master plot values can be obtained for each value of α from the right-hand side of **Eq (I.25)**, using the average E_a value calculated by Friedman (388 kJ/mol) isoconversional method. The resulting experimental master plot values are plotted as a function of α and compared against theoretical master plot curves, as shown in **Figure III.11**. It was clearly observed that the resulting experimental master plots at different heating rates are in good consistent with the Avrami-Erofeev (A3) kinetic model. Also, it can be established that the incorporation mechanism is constant at all heating rates. This finding is in agreement with that obtained by the combined kinetic analysis method.

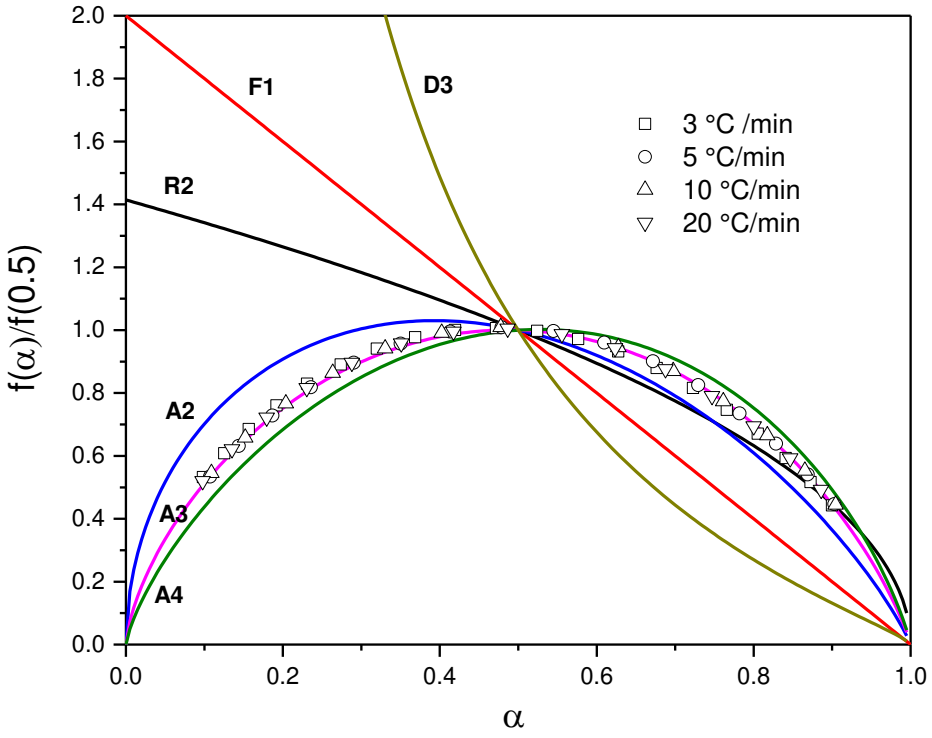

Figure III.11. Comparison of the experimental master plot curves registered at all heating rates (β = 3, 5, 10 and 20 °C/min).

In the general form of Avrami-Erofeev kinetic equations (**Eq (III.7)**), the exponent n indicates the mechanism of nucleation and growth (**Pérez-Maqueda, Criado and Málek, 2003**). The Avrami-Erofeev kinetic model, obtained for the present study, can be certainly considered as an instantaneous random nucleation and three-dimensional growth of nuclei (A3). The obtained reaction mechanism is consistent with those obtained in many perovskite solid solutions found in the literature (**Wang *et al.*, 2000; Stojanovic *et al.*, 2005; Kuscer, Holc and Kosec, 2007**), which involve nucleation and growth process.

$$f(\alpha) = n(1-\alpha)[-\ln(1-\alpha)]^{1-1/n} \qquad \text{(III.7)}$$

III.2.4. Reliability of the Kinetic Parameters

In the last part of the kinetic analysis, the reliability of the obtained kinetic parameters was checked by constructing the simulated kinetic curves and comparing them with the experimental ones. The general kinetic equation for incorporation process under non-isothermal conditions can be rewritten as follows:

$$\frac{d\alpha}{dt} = 4.1 \times 10^{17}\, e^{(-388/RT)} 3(1-\alpha)[-\ln(1-\alpha)]^{2/3} \qquad \text{(III.8)}$$

Figure III.12. (b) represents the experimental and simulated dα/dt-T curves at all heating rates. The simulated α-T kinetic curves can be deduced by integration of the calculated dα/dt values with respect to time. As shown in **Figure III.12. (a)**, the experimental and simulated α-T curves are presented for every β. It is clearly observed that the simulated kinetic curves are quite similar to the experimental ones, which proves the reliability of the kinetic parameters.

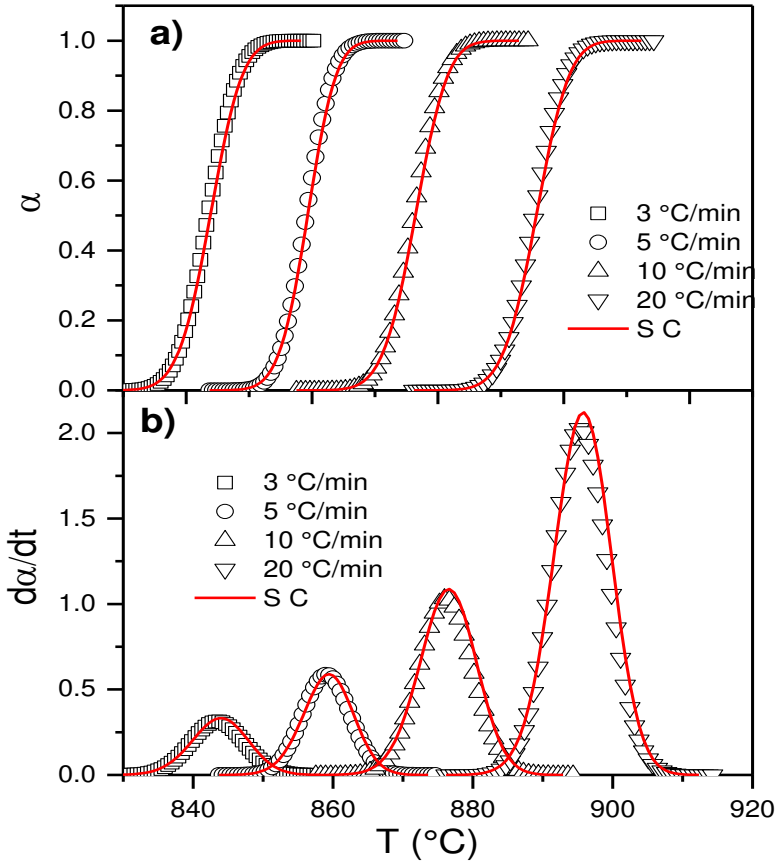

Figure III.12. Simulated (S C) versus experimental curves of **a)** α-T and **b)** dα/dt-T plots corresponding to the incorporation mechanism recorded at different heating rates (β = 3, 5, 10 and 20 °C/min).

III.3. Conclusion

The kinetic analysis of Ca^{2+} incorporation into BT in $Ba_{0.85}Ca_{0.15}TiO_3$ (BCT15) solid solution was explored in this work using non isothermal DSC data at various heating rates (3, 5, 10, and 20 °C min^{-1}) to determine the kinetic parameters of the incorporation mechanism. DSC measurement reveals a single exothermic peak at around 876 °C, which can be attributed to the incorporation of Ca^{2+} into BT to form BCT15. From the XRD data, a pure cubic BT structure was achieved for the BCT15 sample calcined at 1000 °C, which confirms the complete incorporation of Ca^{2+} into BT. The apparent activation energies were determined by Friedman, OFW and KAS isoconversional methods. Results indicate that the values of apparent activation energies are constant with the extent of conversion, proving that the incorporation mechanism is carried out through a single step. Kinetic parameters ($f(\alpha)$, E_a and A) were successfully determined through the combined kinetic analysis method. It was found that the incorporation process follows A3 kinetic model, an activation energy of 388 kJ/mol and a preexponential factor of 4.1×10^{17} min^{-1}. The reliability of the obtained kinetic parameters was proved by comparing simulated and experimental kinetic curves.

Chapter IV

Structural, Microstructural and Electrical Properties of BCT Piezoelectric Ceramics

IV.1. Introduction

Among the different families of lead-free dielectric ceramics, barium titanate (BT) based materials have become one of the most studied dielectric ceramic materials in recent years. The improvement of the properties of this material is mainly done by doping its structure. The objective is to keep the synthesis process simple and to obtain a material with enhanced and reproducible structural and electrical properties.

In this chapter, the influence of Ca^{2+} doping on the structural, microstructural and electrical properties of $Ba_{0.85}Ca_{0.15}TiO_3$ (BCT15) is studied. In addition, the material properties are presented and compared with pure $BaTiO_3$ (BT) ceramic material synthesized by following the same steps.

IV.2. Structural Properties

IV.2.1. Density Measurement

The density of pure BT and BCT15 ceramic pellets was determined using Archimedes methods. The density values are summarized in **Table IV.1**. The theoretical density for both samples (BT and BCT15) were calculated using crystal cell parameters. The resulting pellets density was 5.75 g cm^{-3} (95%) and 5.58 g cm^{-3} (97%) for BT and BCT15 samples, respectively. Both samples have a relative density above 95%, which means that the samples reflect dense ceramic material.

IV.2.2. XRD Results

The crystal structure of the prepared materials (BT and BCT15) was checked by XRD. **Figure IV.1** shows the XRD pattern of prepared samples. The JCPDS (Joint Compounds Powder Diffraction Standards) cards of $BaTiO_3$ is also listed in **Figure IV.1**. Both samples (BT and BCT) presents a perovskite structure similar to that of pure tetragonal barium titanate (PDF#31-0174), without any traces of secondary phases. Moreover, no deformation or broadening of the peaks were observed indicating that the symmetry of the structure remains tetragonal for BCT15 sample.

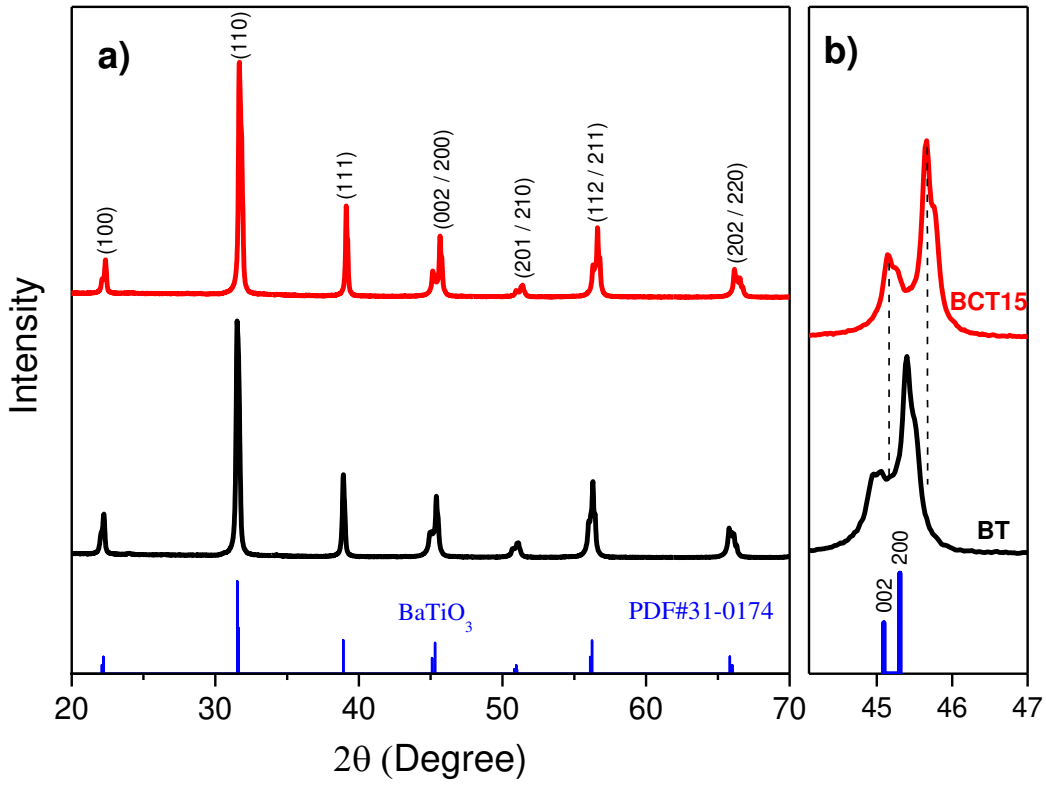

Figure IV.1. a) X-ray diffraction (XRD) pattern of pure (BT) and Ca-doped $BaTiO_3$ (BCT15) sintered at 1400°C **b)** Magnified 2Θ ~ 45° diffraction peak.

However, all the diffraction peaks of BCT15 are slightly shifted to the right compared to those of pure BT suggesting an evolution of the unit cell parameters (**Figure IV.1 (b)**). Therefore, the unit cell parameters are calculated using High score software and the results are illustrated in **Table IV.1**. It was noted that both the lattice parameters (a and c) and the unit cell volume (V) decrease with the addition of Ca^{2+}. Moreover, with c/a ratio that goes from 1.008 to 1.010, the tetragonal distortion has increased. This is due to the fact that the ionic radius of Ca^{2+} (r = 1.34 Å) is smaller than that of Ba^{2+} (r = 1.61 Å). These results confirms the fact that the addition of Ca^{2+} to $BaTiO_3$ provides an increase of the tetragonality and consequently increase the spontaneous tetragonal distortion which by turn helps to improve ferroelectric and piezoelectric properties of BCT15 **(Levin, Krayzman and Woicik, 2013; Shu, 2018; Ako *et al.*, 2019; Buscaglia, Buscaglia and Canu, 2021)**.

Table IV.1. Summary of lattice parameters, measured density (D_M), theoretical density (D_T) and relative density (D_R) for pure (BT) and Ca-doped $BaTiO_3$ (BCT15) ceramics sintered at 1400°C.

Sample name	a=b (Å)	c (Å)	c/a	Volume ($Å^3$)	D_M (g/cm^3)	D_T (g/cm^3)	$D_R = \frac{D_M}{D_T}$ (%)
BT	3.99436	4.02617	1.008	64.2370	5.75	6.03	95
BCT15	3.97198	4.01253	1.010	63.3041	5.58	5.73	97

IV.2.3. Raman Spectroscopy

The Raman spectrum of pure (BT) and Ca-doped barium titanate (BCT15) at room temperature are illustrated in **Figure IV.2**. **Table IV.2** summarize the Raman modes of tetragonal pure $BaTiO_3$ collected from the previous reports. Raman spectra of BCT15 possessed the same modes as tetragonal pure $BaTiO_3$. The ~520 and ~720 cm^{-1} modes are slightly shifted to higher frequency for BCT15 due to the increase in force constant caused by the substitution of Ba^{2+} by Ca^{2+} at the A site **(Chang, 2000; Puli *et al.*, 2014)**. However, the ~250 cm^{-1} and ~305 cm^{-1} modes slightly shifted to lower frequency with addition of Ca^{2+}. This shift might be associated to the phonon vibrations of Ti–O bonds **(Chang, 2000)**. We also notice that the peak ~305 cm^{-1} has broadened with the addition of Ca^{2+}, this effect has also been observed by Shu et al**. (Shu, Reed and Button, 2018)**, where they observed a linear dependence between peak broadening and Ca^{2+} concentration. Both [B_1/E(TO+LO)], [$A_1(TO_3)$/E(TO)] modes at ~305 and ~520 cm^{-1} respectively, indicate the presence of the tetragonal phase at room temperature **(Chang, 2000)**, which is in good agreement with the XRD findings. These results are consistent with previous reports on BT and BCT based ceramics **(Chang, 2000; Yun, Wang, Li, *et al.*, 2009; Yun, Wang, Shi, *et al.*, 2009)**.

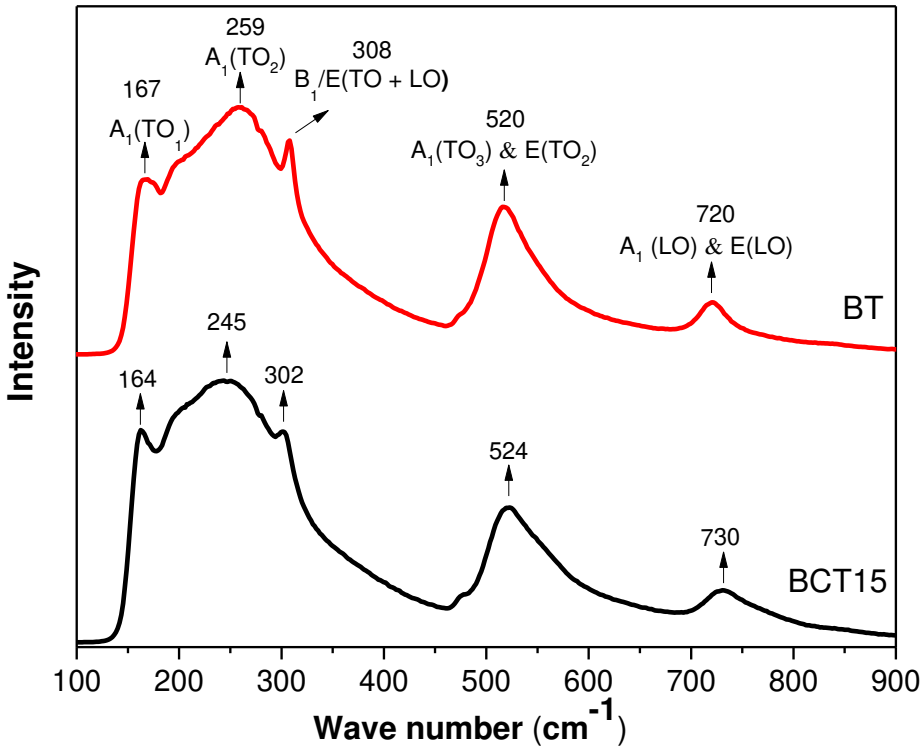

Figure IV.2. Raman spectrum of pure (BT) and Ca-doped barium titanate (BCT15) at room temperature.

Table IV.2. Raman modes for Tetragonal pure $BaTiO_3$ **(Freire and Katiyar, 1988; Dobal *et al.*, 2001; Karan *et al.*, 2009; Gajović *et al.*, 2013; Buscaglia *et al.*, 2014)**.

Raman shifts	Raman modes	Related molecular vibrations
~180	[$A_1(TO_1)$]	Ti^{+4} vibrating against the O^{-2}-cage
~250	[$A_1(TO_2)$]	Polar [TiO_6] vibrating against the Ba^{2+} -cage
~305	[B_1/E(TO + LO)]	Asymmetry within the [TiO_6] octahedra
~520	[$A_1(TO_3)$ & $E(TO_2)$]	Ti-O bond movement
~720	[A_1 (LO) & E(LO)]	Bending and stretching of [TiO_6]

IV.3. Microstructural Properties

For a comparative study, the microstructural analysis of pure $BaTiO_3$ (BT) and Ca-doped $BaTiO_3$ (BCT15) samples sintered at 1400 °C was carried out. **Figure IV.3** shows the SEM micrographs of BT and BCT15 samples. Before getting these SEM images, the samples were polished and then thermally etched (at 1200 °C for 30 min) to reveal the grains.

Both samples correspond to well-sintered material with a tiny amount of pores, which confirms the as obtained high relative density (> 95%) and also demonstrates that dense samples of BT and BCT15 can be prepared at 1400 °C. For pure $BaTiO_3$, it is clear that the microstructure is inhomogeneous and that the grains have irregular morphologies with different sizes varying between 3 and 19 µm with an average grain size of 13.2 (± 0.6) µm. On the other side, the BCT15 sample presents more or less a homogeneous microstructure. In BCT15, the grains grow and give a microstructure with grains between 8 and 22 μm with an average of 16.6 (± 0.8) µm. From all that has been mentioned before, it is clear that the addition of Ca^{2+} significantly improve the microstructure of $BaTiO_3$.

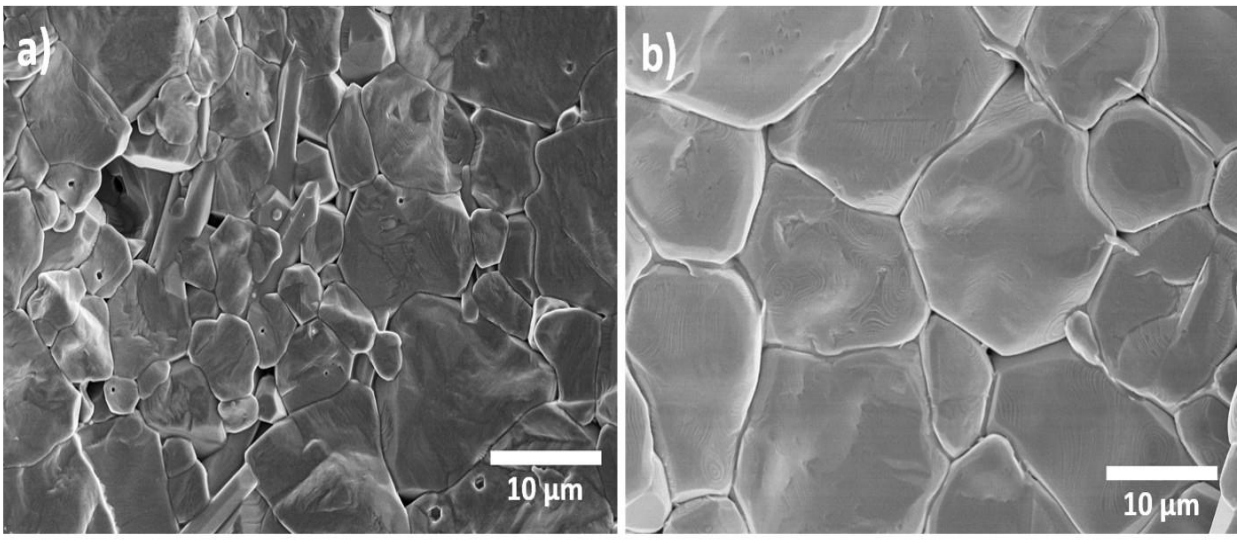

Figure IV.3. SEM micrographs of **a)** BT and **b)** BCT15 samples sintered at 1400°C for 4h.

Using the SEM and in order to identify the elemental composition of BT and BCT15 samples, an Energy Dispersive X-ray (EDS) analysis was performed. The EDS spectrum of BT and BCT15 are displayed in **figure IV.4**. From the EDS spectrum, it is clear that only the constituent elements of BT and BCT15 samples (Ba, Ti, and Ca) are present which confirms that no contamination occurred during the preparation process.

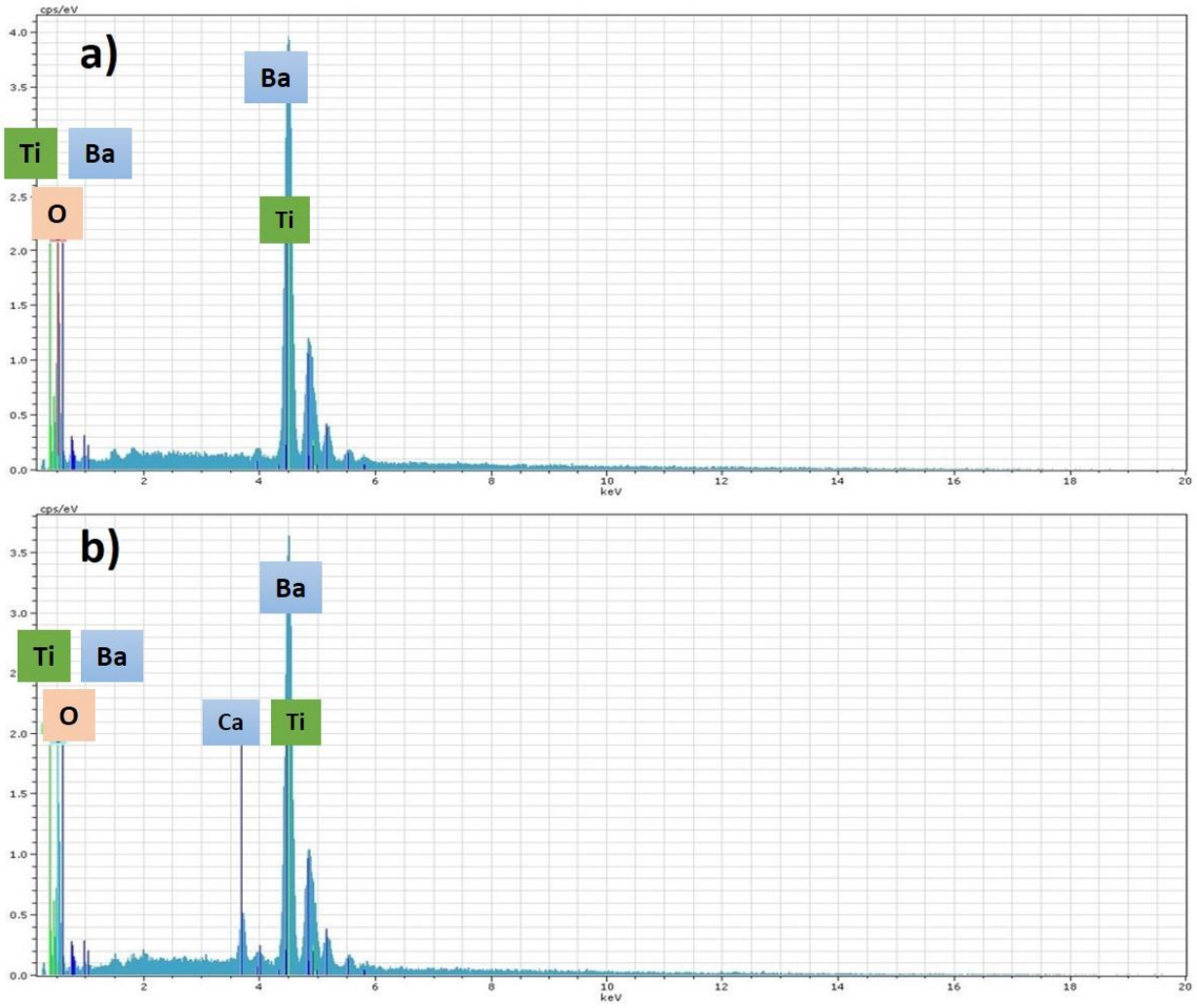

Figure IV.4. EDS elemental composition of **a)** BT and **b)** BCT15 samples sintered at 1400°C for 4h.

IV.4. Dielectric Properties

IV.4.1. LCR Measurements

The temperature dependence of dielectric constant (ε') and dielectric loss (tanδ) of BT and BCT15 sintered samples were studied at four different frequencies (1 kHz, 10 kHz, 20 kHz and 100 KHz) and plotted in **Figure IV.5**. Details of the plots have been summarized in **Table IV.3**. Both schematics are quite similar, the value of ε' increases to a maximum value (ε'_{max}) with increase in temperature up to the curie transition T_c and then decreases evenly indicating a phase transition (tetragonal to cubic phase transition).

Figure IV.6 presents the temperature dependence of dielectric constant (ε') and dielectric loss (tanδ) measured at 1 kHz. For pure BT, maximum dielectric constant ~8671 at T_c ~117 °C and dielectric loss of ~0.019 is observed. For BCT15, the T_c remain approximatively constant ~116 °C where the dielectric constant was ~8099 with a dielectric loss of 0.013.

Moreover, it is clear that as Ca^{2+} is added to $BaTiO_3$, the dielectric constant at RT decreases from 1540 to around 700 which is due to the non-ferroelectric nature of $CaTiO_3$ **(Varatharajan *et al.*, 2000; Wada *et al.*, 2004)**. The value of tanδ is low (under 0.1) for both samples and in all frequencies, and it is increased by increasing the frequency from 1 KHz to 100 KHz. In addition, the results of the dielectric measurements show that the behavior of BT and BCT15 samples is that of a normal ferroelectric, their Curie transition, respectively equal to 117°C and 116°C, exhibit a sharp peaks that do not change with frequency **(Zeb and Milne, 2013; Huang *et al.*, 2016)**.

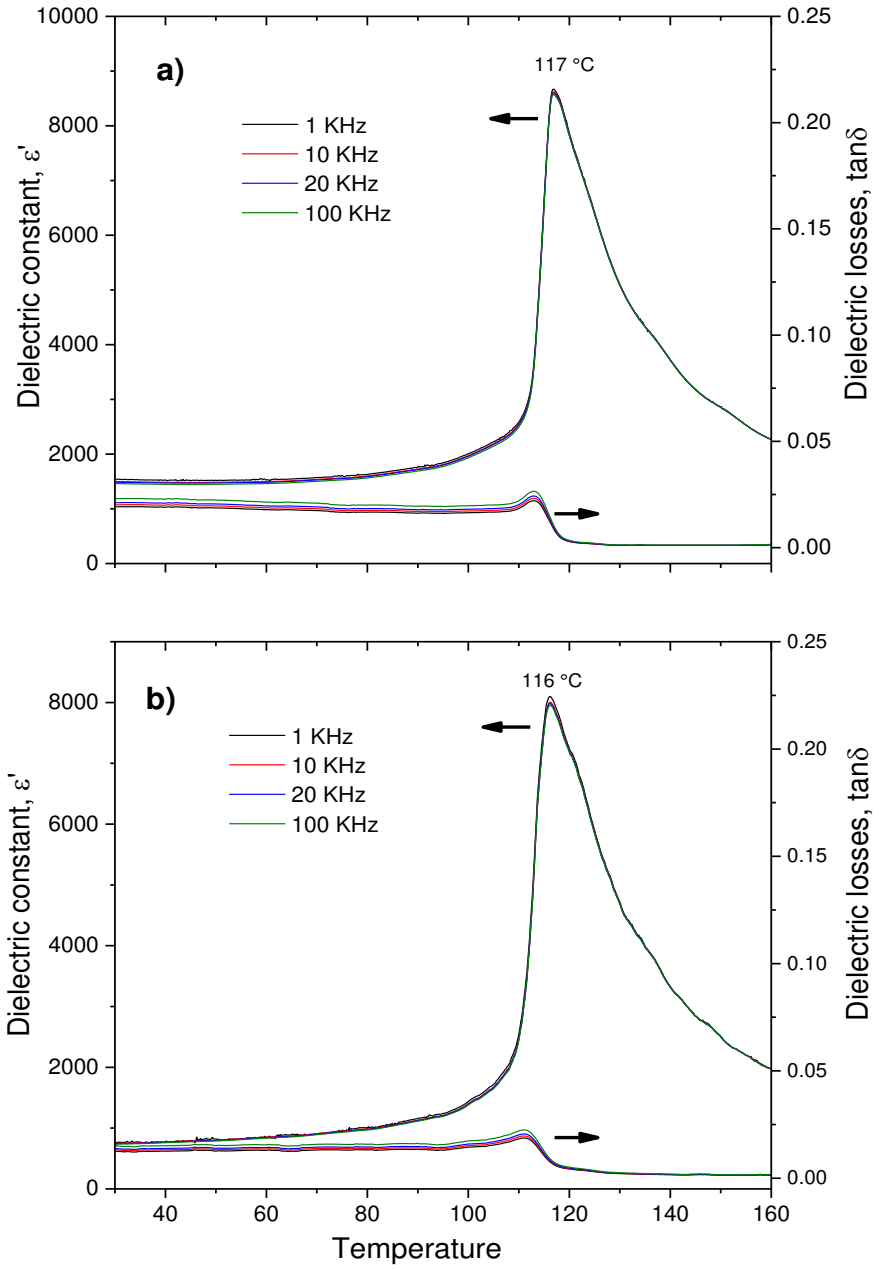

Figure IV.5. The temperature dependence of dielectric constant (ε') and dielectric loss (tanδ) of **a)** BT and **b)** BCT15 sintered samples at 1 kHz, 10 kHz, 20 kHz and 100 KHz.

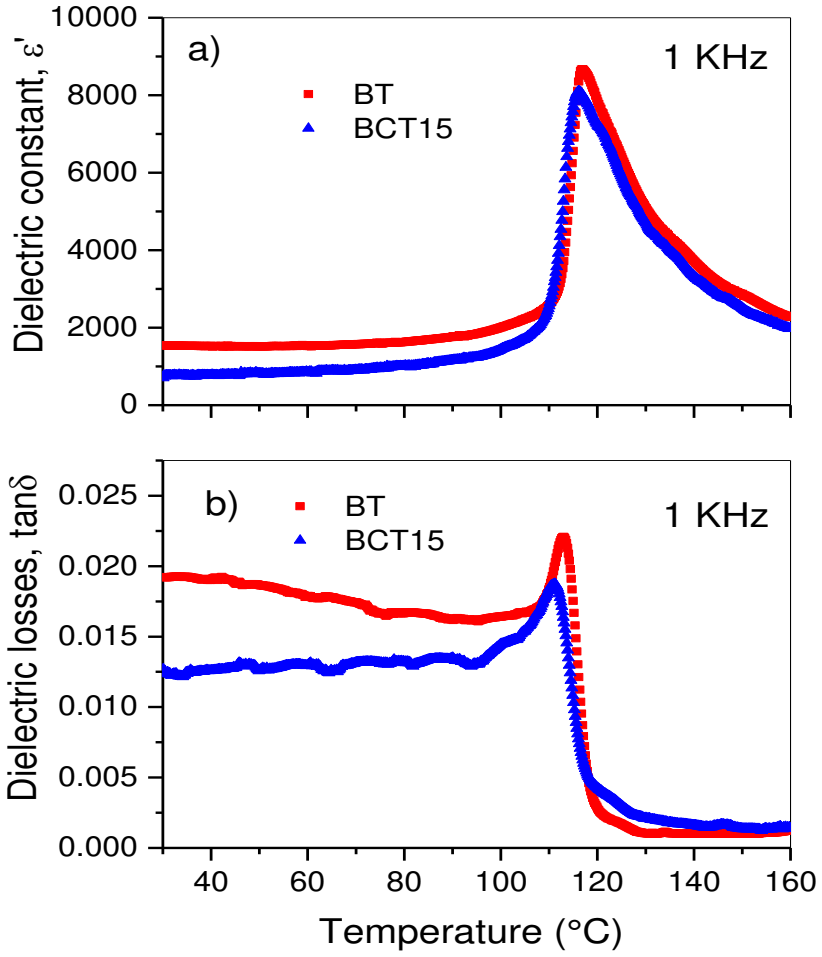

Figure IV.6. The temperature dependence of **a)** dielectric constant (ε') and **b)** dielectric loss (tanδ) of BT and BCT15 sintered samples measured at 1 kHz.

For a normal ferroelectric, the Curie–Weiss law (**Eq (II.7)**) is followed. **Figure IV.7** shows the inverse of dielectric constant (ε') as a function of temperature measured at 1 kHz. The fitting parameters were extracted from **Eq (II.7)** and summarized in **Table IV.3**. It is clear that the dielectric permittivity of pure BT and BCT15 ceramic samples follows the Curie–Weiss law below the T_c.

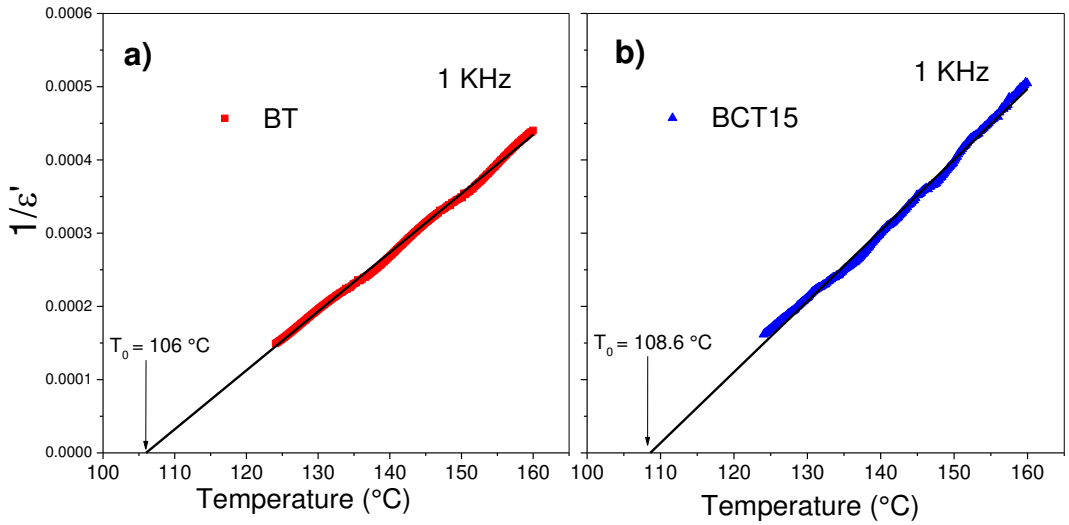

Figure IV.7. Curie-Weiss plot for **(a)** pure BT and **(b)** BCT15 ceramics (symbols: experimental data; solid line: fitting to the Curie–Weiss law).

The diffuse character of the ferroelectric-paraelectric phase transition for BT and BCT15 ceramic samples was studied by the modified Curie-Weiss relationship (**Eq (II.8)**). **Figure IV.8** displays the plot of $\ln(1/\varepsilon' - 1/\varepsilon'_{max})$ versus $\ln(T_0 - T_C)$ for BT and BCT15 samples.

The value of γ (**Table IV.3**), obtained by fitting the experimental data based on **Eq (II.8)**, was found to be 1.24 for pure BT and 1.37 for BCT15. The γ values are close to 1, which confirm that both phase transitions are typical for normal ferroelectric **(Panigrahi and Panigrahi, 2010; Rached *et al.*, 2021)**. The small increase of diffuseness with addition of Ca^{2+} ions could be linked to the compositional variation and structural disarranging of cations in one or more crystallographic sites of the perovskite structures **(Panigrahi and Panigrahi, 2010)**.

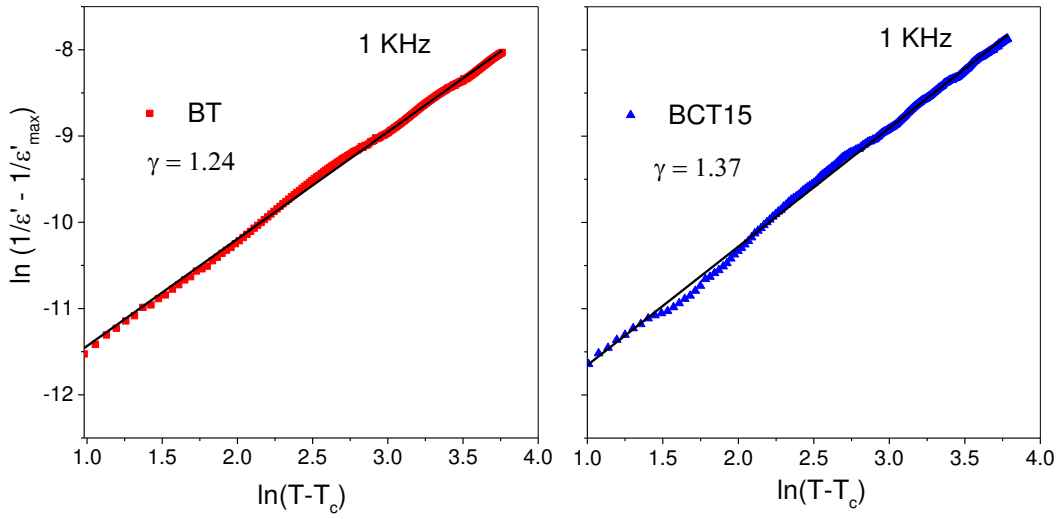

Figure IV.8. Modified Curie-Weiss plot for **(a)** pure BT and **(b)** BCT15 ceramics (symbols: experimental data; solid line: fitting to the modified Curie–Weiss law).

IV.4.2. Differential Scanning Calorimetry (DSC)

In order to confirm the tetragonal to cubic phase transition temperature T_c, The DSC on pure BT and BCT15 sintered samples were performed and each sample provides an endothermic peak at 120 (for BT) and 121.2 °C (for BCT15) **(Figure IV.9)**. The value of T_c at the phase transition temperature is very similar to that obtained by LCR measurement. A slight difference between DSC and LCR values was observed, which could be related to the high sensitivity of DSC compared to LCR measurements.

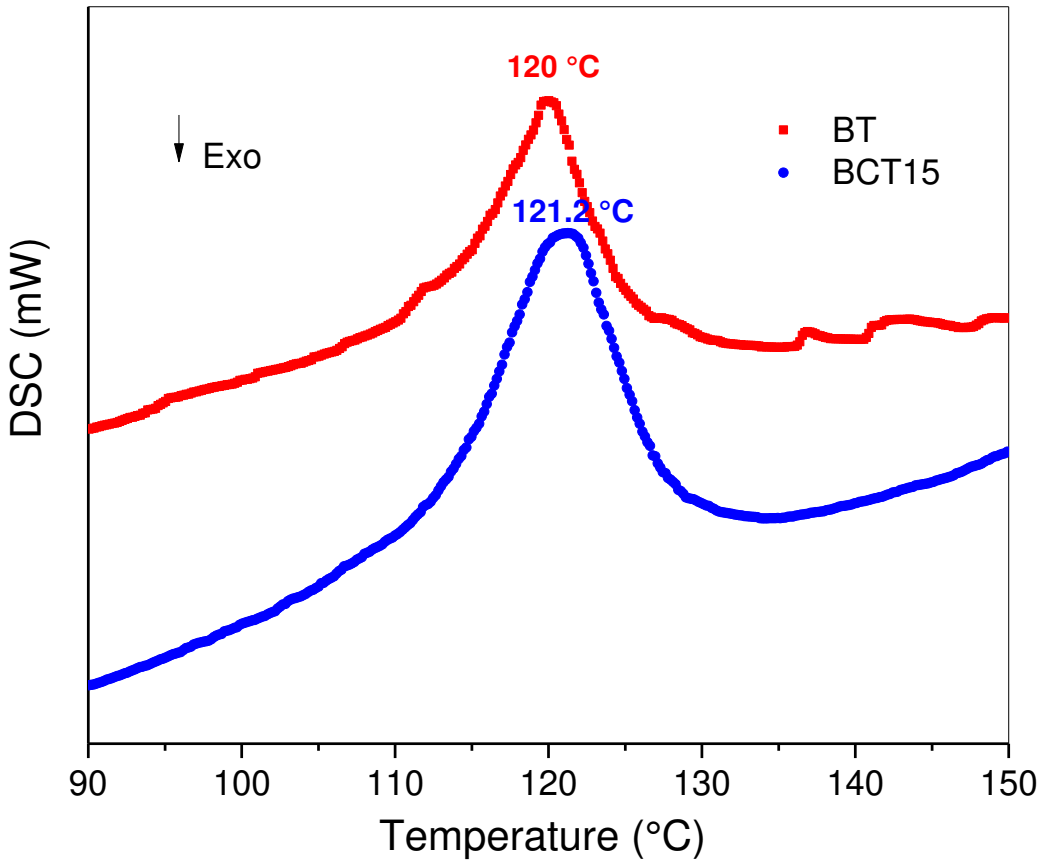

Figure IV.9. DSC trace of pure BT and BCT15 sintered samples at 1400-4h.

Table IV.3. Summary of the properties of BT and BCT15 ceramics sintered at 1400°C.

Samples	**BT**	**BCT15**
Relative density (%)	95	97
ε' (RT)	1540	700
Grain size (μm)	13.2 ± 0.6	16.6 ± 0.8
ε'_{max} (1 KHz)	8671	8099
tanδ (1KHz)	0.019	0.013
T_c (°C) from ε′ (1KHz)	117	116
T_c (°C) from DSC	120	121
T_0 (°C) (1KHz)	106	108.6
$T_c - T_0$	11	7.4
C_w (10^5 °C)	1.24	1.03
γ	1.24	1.37

IV.5. Conclusion

In conclusion, the current chapter focuses on the study of the influence of Ca^{2+} doping on the microstructural, structural and electrical properties of $Ba_{0.85}Ca_{0.15}TiO_3$ (BCT15) ceramics prepared by conventional route. The XRD patterns confirm the formation of single-phase tetragonal perovskite structure in BT and BCT15 ceramic samples. XRD analysis also reveals that both the lattice parameters (a and c) and unit cell volume (V) decreased while the tetragonality (c/a) increased with the addition of Ca^{2+}, which consequently increases spontaneous tetragonal distortion and thus enhancement of the piezoelectric and ferroelectric properties of BCT15. The obtained Raman spectra are consistent with those found in literature and confirms the total incorporation of Ca^{2+} ions into the structure. SEM micrographs of BCT15 ceramic sample demonstrate dense and homogeneous microstructure. The grain size of BCT15 sample increases with the addition of Ca. The dielectric measurements show that the BT and BCT15 samples behave as normal ferroelectrics. Our data shows that Ca substitution promote a slight shift (~1 °C) of T_c with respect to pure $BaTiO_3$. The dielectric constant (ε') was decreased by the addition of Ca due to the non-ferroelectric nature of $CaTiO_3$.

Chapter V

Reactive Flash Sintering of $BiFeO_3$-$BaTiO_3$ Piezoelectric Ceramic

V.1. Introduction

Basically, dense $BiFeO_3$-$BaTiO_3$ ceramics are synthesized in two steps, including preparation and sintering of $BiFeO_3$-$BaTiO_3$ powders. Both steps need high temperatures and long treatment times, which are high energy consuming. Under these conditions, it is difficult to prepare dense and stoichiometric $BiFeO_3$-$BaTiO_3$ ceramics due to the high volatilization of Bi and reduction of Fe^{3+} resulting in impurity formation such as $Bi_2Fe_4O_9$, $Bi_{25}FeO_{39}$, or Bi_2O_3 (**Pabst *et al.*, 2007; Zheng *et al.*, 2014; Cheng *et al.*, 2018; Xun *et al.*, 2021**). Thus, other techniques to prepare dense and stoichiometric $BiFeO_3$-$BaTiO_3$ ceramics are required. Exploring different techniques to prepare dense and stoichiometric $BiFeO_3$-$BaTiO_3$ ceramics, such as flash sintering (described in section I.4.2), is of great interest for several reasons including its lower onset sintering furnace temperatures and its short time densification as compared to conventional preparation techniques (**Cologna, Rashkova and Raj, 2010; Prette *et al.*, 2011; Caliman *et al.*, 2016; Jha *et al.*, 2018; Shi, Pu, Wang, *et al.*, 2019; Vendrell *et al.*, 2019; Phuah *et al.*, 2021**). Also, it is a promising processing method to prevent the high volatility of certain elements during the preparation of materials, such as potassium (**Wu *et al.*, 2020**), bismuth (**Perez-Maqueda *et al.*, 2019; Shi, Pu, Li, *et al.*, 2019; Taghaddos *et al.*, 2019; Wassel *et al.*, 2019**) and lithium (**Clemenceau *et al.*, 2019**). Moreover, it has been reported that it is possible to prepare single-phase oxides in a single step by flash sintering of its precursors (**Gil-González *et al.*, 2018**). This methodology has been called Reactive Flash Sintering (RFS) and has been used to prepare other materials, such as lead zirconate titanate (PZT), sodium potassium niobate (KNN) and other multi-phase oxide ceramics (**Yoon *et al.*, 2018; Avila and Raj, 2019; Jia *et al.*, 2019; Avila *et al.*, 2020; Wu *et al.*, 2020**).

The scope of this chapter is to explore the synthesis and densification of $0.67BiFeO_3$-$0.33BaTiO_3$ (BFO-33BT) ceramics in a single step using reactive flash sintering. Adjustment of the experimental flash conditions (applied electric field and selected current density limit) was performed to obtain a high-quality ceramic.

V.2. Preparation of BFO-33BT by Reactive Flash Sintering

V.2.1. Adjustment of the Experimental Flash Conditions

Series of experiments for the preparation of $0.67BiFeO_3$-$0.33BaTiO_3$ (BFO-33BT) by reactive flash sintering were performed with the aim of adjusting the experimental flash conditions, i.e., applied electric field (E (V cm^{-1}) and selected current density limit (I (mA mm^{-2}).

The results obtained from the experiments are displayed in **Figure V.1**. In this Figure, two large regions where reaction is either incomplete or heterogeneous (due to localization of the electrical current) can be clearly distinguished. Thus, only in a very narrow range of experimental conditions (electric field of 35 V cm^{-1} and current density of 60 or 70 mA mm^{-2}), within the boundary between incomplete and heterogeneous regions, the reaction is optimal, yielding a homogeneous material. The corresponding captured images of resulting flash sintered samples corresponding to incomplete, heterogeneous and optimal reactions are also included in **Figure V.1 (b-d)**. Samples prepared within the optimal experimental conditions range yielded an identical density of 6.90 g cm^{-3}, corresponding to a relative density of 91%, as determined by the Archimedes method (**Table V.1**).

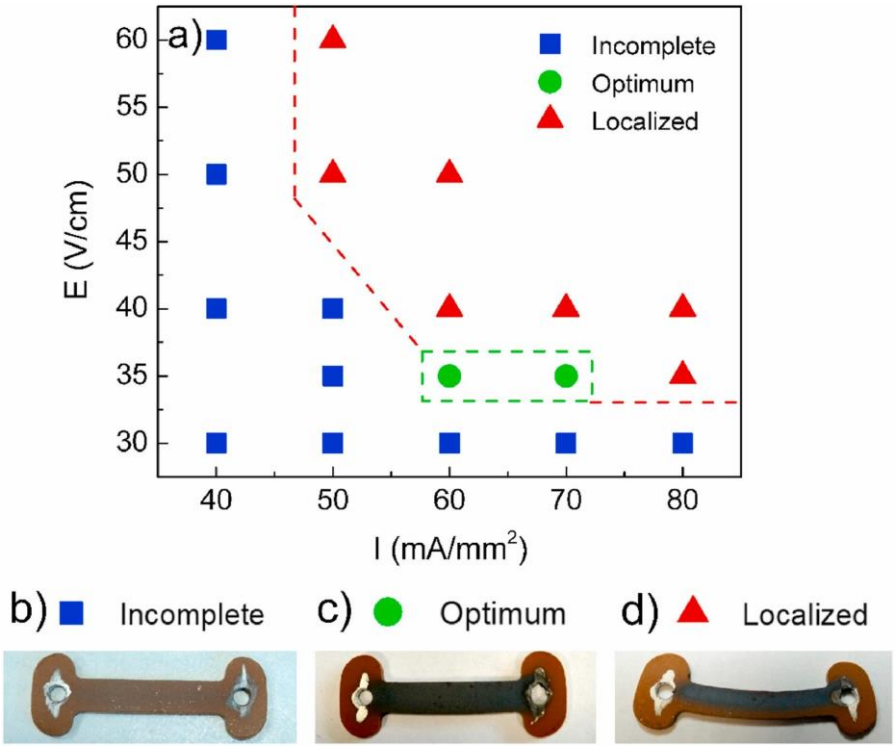

Figure V.1. (a) Experimental conditions used for the reaction flash sintering of BFO-33BT. Dog bone samples for **(b)** incomplete reaction (30 V cm^{-1}, 40 mA mm^{-2}), **(c)** optimum reaction conditions (35 V cm^{-1}, 60 mA mm^{-2}) and **(d)** heterogeneous reaction (due to localization, 50 V cm^{-1}, 60 mA mm^{-2}).

Figure V.2 shows, as examples, the plots of the power density and XRD diffraction patterns corresponding to the samples shown in the photographs in **Figure V.1**, which resulted in incomplete (30 V cm^{-1}, 40 mA mm^{-2}), optimum (35 V cm^{-1}, 60 mA mm^{-2}) and localized (50 V cm^{-1}, 60 mA mm^{-2}) reactions. The generated electrical power density was calculated by multiplying the current density passing through the circuit (I) and the voltage (E) (**Eq (V.1)**).

$$P = E.I \qquad \text{(V.1)}$$

As expected, the flash event takes place at lower temperatures as the applied electric field is increased. Thus, significant deviations on the onset of the flash are observed for the reactive flash-sintering of $0.67BiFeO_3$-$0.33BaTiO_3$, which takes place at 742 °C, 858 °C and 910 °C for the Localized, optimum and incomplete reactions, respectively. The XRD diffraction patterns of these samples are included in **Figure V.2 (b)**. It can be observed that the specimens corresponding to the incomplete and localized flash reactions show certain amounts of the secondary phase $Bi_{25}FeO_{39}$. On the other hand, the sample prepared under an applied voltage of 35 V cm^{-1} and a current density limit of 60 mA mm^{-2} (optimum reaction) is phase pure $0.67BiFeO_3$-$0.33BaTiO_3$. Interestingly, the XRD data show that it is possible to obtain phase pure $0.67BiFeO_3$-$0.33BaTiO_3$ samples by reactive flash sintering as long as the experimental conditions are properly controlled. Therefore, an electric field of 35 V cm^{-1} and a current density of 60 mA mm^{-2} can be considered as the optimum conditions for the preparation of BFO-33BT by reactive flash sintering, as a lower power density (0.210 W mm^{-3}) is required as compared to the other sample obtained with a current intensity of 70 mA mm^{-2} (0.245 W mm^{-3}).

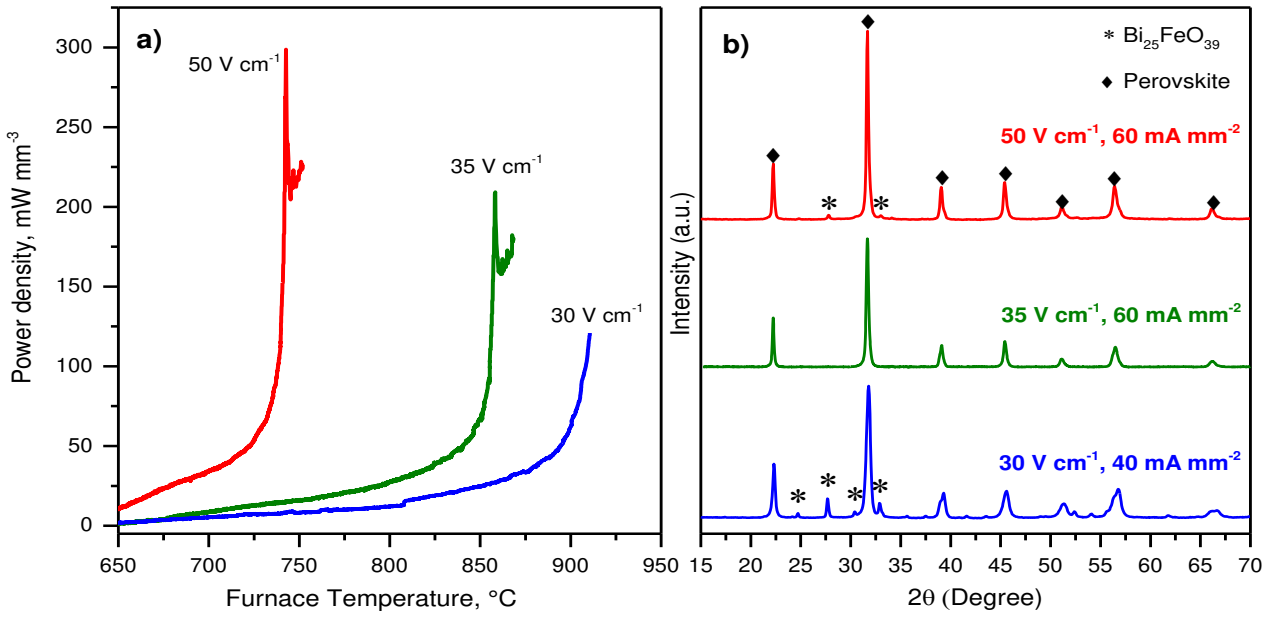

Figure V.2. (a) Power dissipation profiles and **(b)** XRD patterns corresponding to the samples shown in the photographs in **Figure V.1**.

Table V.1. Reactive flash-sintering parameters for $0.67BiFeO_3$-$0.33BaTiO_3$. The optimum reactive flash-sintering parameters have been marked in bold.

E (V cm^{-1})	I (mA mm^{-2})	P (mW mm^{-3})	T_{on} (°C)	Relative density (%)	Reaction
30	40	120	910	81	Incomplete
35	**60**	**210**	**858**	**91**	**Optimum**
35	**70**	**245**	**861**	**91**	**Optimum**
40	60	240	815	89	Localized
5O	60	300	742	87	Localized
60	60	360	690	85	Localized

Another interesting feature of these experiments is related to the onset temperature for the flash event. Dong et al. (**Dong and Chen, 2015**) observed a relationship between the applied electric field (E) and the onset temperature for RFS (T_{on}). **Figure V.3** presents the relationship between the applied electric (E) field and the onset temperature (T_{on}) of flash. The flash event occurred at 910, 858, 815, 742 and 690 °C at the applied electric field of 30, 35, 40, 50 and 60 V cm^{-1}, respectively, which indicates that the onset temperature of RFS gradually decreases as the initial electric field increases, as shown in **Figure V.3. (a)**. In **Figure V.3. (b)**, a linear dependence (R^2 = 0.998) of the logarithm of the DC applied electric field, lnE, and the inverse of the flash temperature onset, $1000/T_{on}$. This behavior is in agreement with the reported results (**Downs and Sglavo, 2013; Dong and Chen, 2015; Yadav and Raj, 2017**).

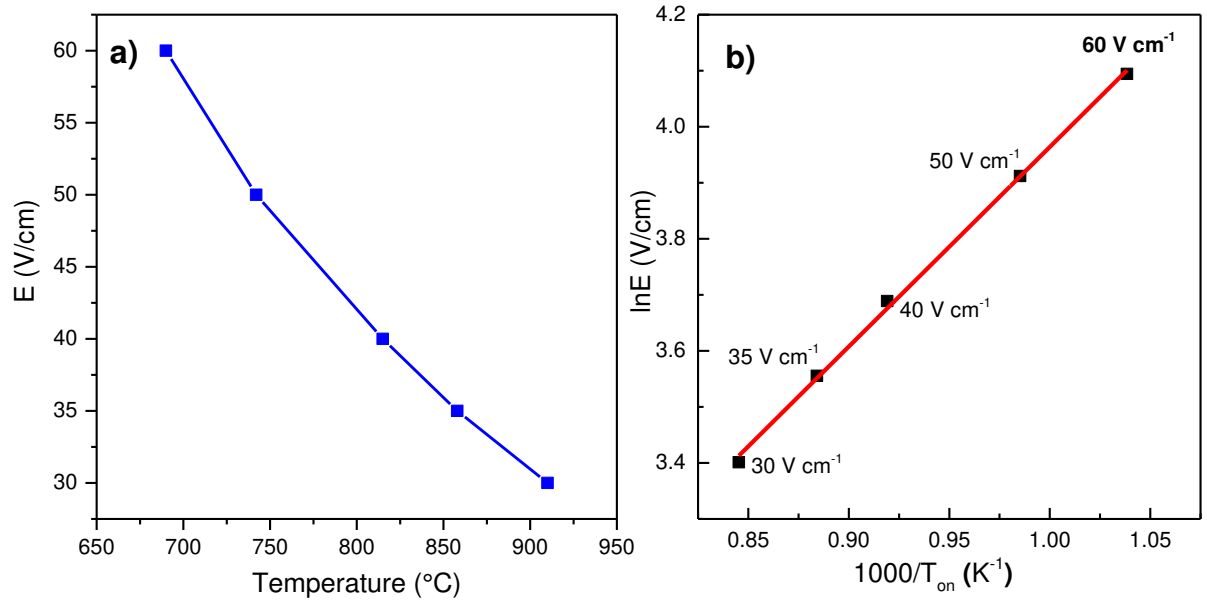

Figure V.3. (a) The flash electric field as a function of the onset temperature **(b)** Arrhenius plot of the applied DC electric field as a function of the inverse of the onset temperature for the reactive flash event, $1000/T_{on}$.

V.2.2. Reactive Flash Sintering of BFO-BT

Figure V.4 shows the evolution of electric field, current intensity, and power dissipation as a function of furnace temperature for the sample flashed under optimal conditions (35 V cm^{-1}, 60 mA mm^{-2}). The three stages of the flash sintering experiment are clearly observed in these figures. Thus, after a first stage, where the electric field is maintained constant by the power supply at 35 V cm^{-1}, the current density (**Figure V.4. (a)**) rises sharply in a second stage to the preset maximum value of 60 mA mm^{-2} (corresponding to a power dissipation of 210 mW mm^{-3}, **Figure V.4. (b)**. At this point, the power supply shifts from constant voltage (CV) to current controlled (CC) regime. In the third stage, the sample is maintained in a flash-activated state under controlled current (CC). The onset of flash is reached at a furnace temperature of 858 °C.

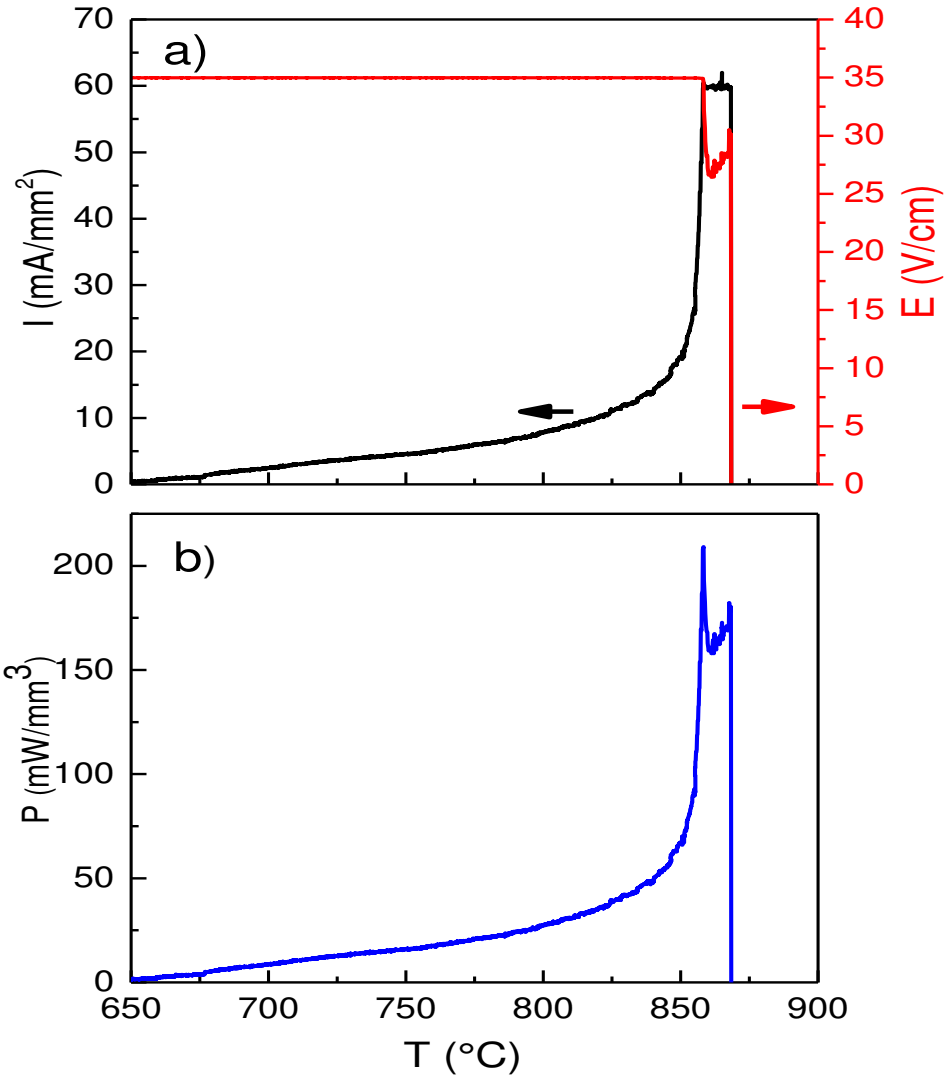

Figure V.4. (a) Evolution of electric field and current density, and **(b)** power dissipation versus furnace temperature for the reaction flash sintering experiment performed at an electric field of 35 V cm^{-1} and a current density limit of 60 mA mm^{-2}.

The temperature of the sample at stage III of the flash can be estimated by using the blackbody radiation model (**Raj, 2012**):

$$T = \left[T_0^4 + \frac{W}{A\varepsilon\sigma}\right]^{1/4} \qquad \text{(V.2)}$$

where T and T_0 respectively reflect the real sample temperature and the furnace temperature, W is the power dissipation, A is the surface area of the sample (m^2), ε is the emissivity (0.9) and σ is Stefan's constant (5.67×10^{-8} W m^{-2} K^{-4}). Thus, the estimated real temperature of the sample was found to be approximately 1050 °C.

Field-assisted processing of materials is commonly analyzed in terms of power dissipation density. The Arrhenius plot of the power dissipation is shown in **Figure V.5**. At low temperatures, the power dissipation exhibits a linear-like type behavior. This behavior is interrupted at 50 mW mm^{-3} when the flash event takes place, followed by a sharp increase in the 90–210 mW mm^{-3} power dissipation range that signals the onset of flash. It is remarkable that the inflexion of the curve that signals the flash event occurs within the same narrow range (10–50 mW mm^{-3}) described in literature for flash sintering of numerous materials, despite the fact that, in this case, there is a reaction and sintering taking place at the same time (**Raj *et al.*, 2021**).

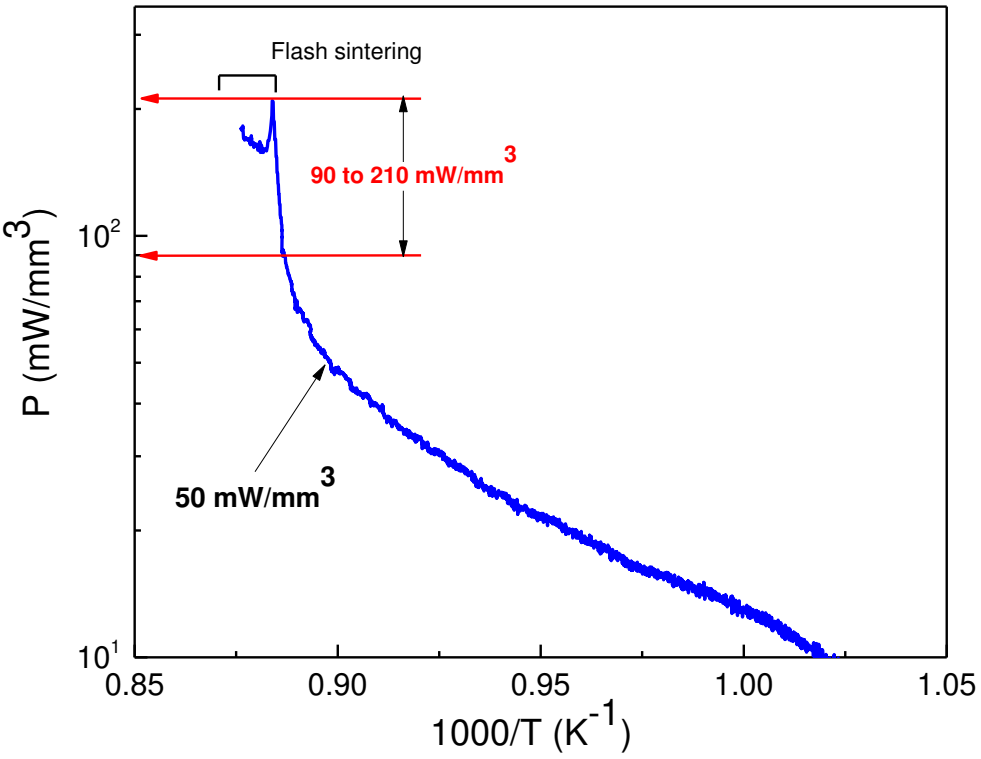

Figure V.5. Arrhenius plot for the BFO-33BT flashed sample.

V.2.2.1. Structural Characterization

Figure V.6 shows the room temperature XRD pattern of the BFO-33BT sample before and after the flash (at 35 V cm^{-1} and 60 mA mm^{-2}). The JCPDS cards of $BiFeO_3$ and $BaTiO_3$ are also listed in **Figure V.6**. The XRD peaks of the sample before the flash are broad due to the small crystallites size obtained after ball milling during 15 min and the mixture is completely composed of the starting precursors: Bi_2O_3 (**JCPDS #71–0465**), Fe_2O_3 (**JCPDS # 24–0072**) and $BaTiO_3$ (**JCPDS #31–0174**). After the flash, the XRD pattern of the sample evidences that the composition BFO-33BT is within the MPB region of the BFO-BT system.

Thus, a significant splitting is observed in the reflections at 2θ values of 39° and 56.5° (see inset in **Figure V.6**), which has been associated with the coexistence of rhombohedral (R3c) and pseudocubic (PC) phases (**Yang *et al.*, 2013; Xun *et al.*, 2021; Yin *et al.*, 2021**). The ratio between the R3c and PC phases was estimated by deconvolution of these reflections, using a pseudo-Voigt function, and the results indicate that a mixture of 57% R3c and 43% PC phases is obtained (see inset in **Figure V.6**). Thus, it can be concluded that the Bi_2O_3–Fe_2O_3–$BaTiO_3$ mixed powders are transformed to a mixture of R3c and PC phases of $0.67BiFeO_3$-$0.33BaTiO_3$ after the reactive flash sintering.

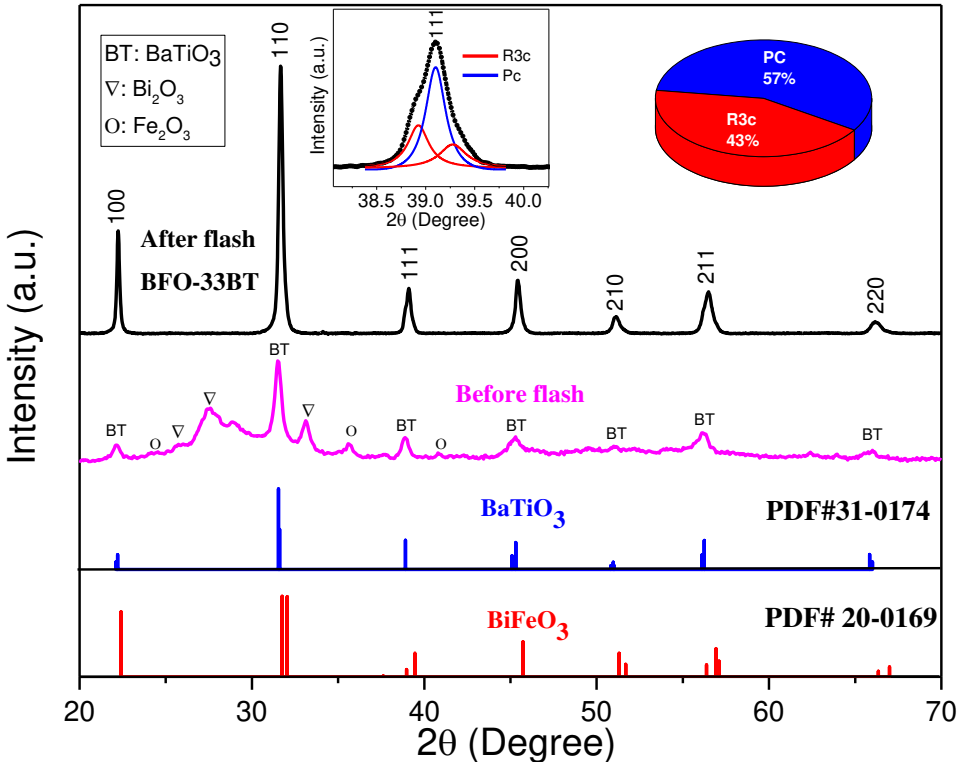

Figure V.6. XRD patterns of BFO-33BT sample before and after the reaction flash process.

Thus, it can be concluded that the Bi_2O_3-Fe_2O_3-$BaTiO_3$ mixed powders are transformed to a mixture of R3c and PC phases of $0.67BiFeO_3$-$0.33BaTiO_3$ after the reactive flash sintering. The presented synthesis route using reactive flash sintering led to a significant reduction of the furnace reaction temperature (Ts ~ 858 °C) and time (t = 30s) for $0.67BiFeO_3$-$0.33BaTiO_3$, compared to conventional solid-state method (**Li *et al.*, 2017; Lee *et al.*, 2018; Kim, Lee and Song, 2019**), which requires at least 1000 °C and 2 to 3 hours of dwell time.

The Raman spectrum for the BFO-33BT sample obtained under optimal conditions (35 V cm^{-1}, 60 mA mm^{-2}) is shown in **Figure V.7**. The spectrum obtained clearly presents 8 mode peaks, three of them belonging to A1 modes at 177, 250 and 476 cm^{-1}, and five to E modes at 307, 522, 566, 663 and 750 cm^{-1}. These values are consistent with previous reports of $BiFeO_3$-$BaTiO_3$ based ceramics. Thus, Bouzidi et al. (**Bouzidi *et al.*, 2019**), Qi et al. (**Qi *et al.*, 2020**) and Li et al. (**Li, Zheng and Wu, 2021**) observed, for conventionally prepared $BiFeO_3$-$BaTiO_3$, bands at approximately the same values as for the A1 and E modes. They were able to distinguish two main regions in the Raman spectrum: (i) low frequency vibrational modes below 400 cm^{-1}, which are essentially associated to the vibrations of B-O band. In particular, the most intense vibration mode, at around 250 cm^{-1}, has been assigned to Fe/Ti-O. (ii) High frequency vibrational modes above 400 cm^{-1} reflect to the vibrational frequencies of BO_6 octahedral. Our results are also in good agreement with those obtained by Pakalniškis et al. (**Pakalniškis *et al.*, 2020**) for $BiFeO_3$-$BaTiO_3$ samples prepared by sol gel method. On the other hand, the appearance of the vibration mode at around 750 cm^{-1} indicates the existence of the rhombohedral (R3c) symmetry (**Bouzidi *et al.*, 2019**), which confirms the mixture of rhombohedral and pseudocubic symmetry expected at the MPB region.

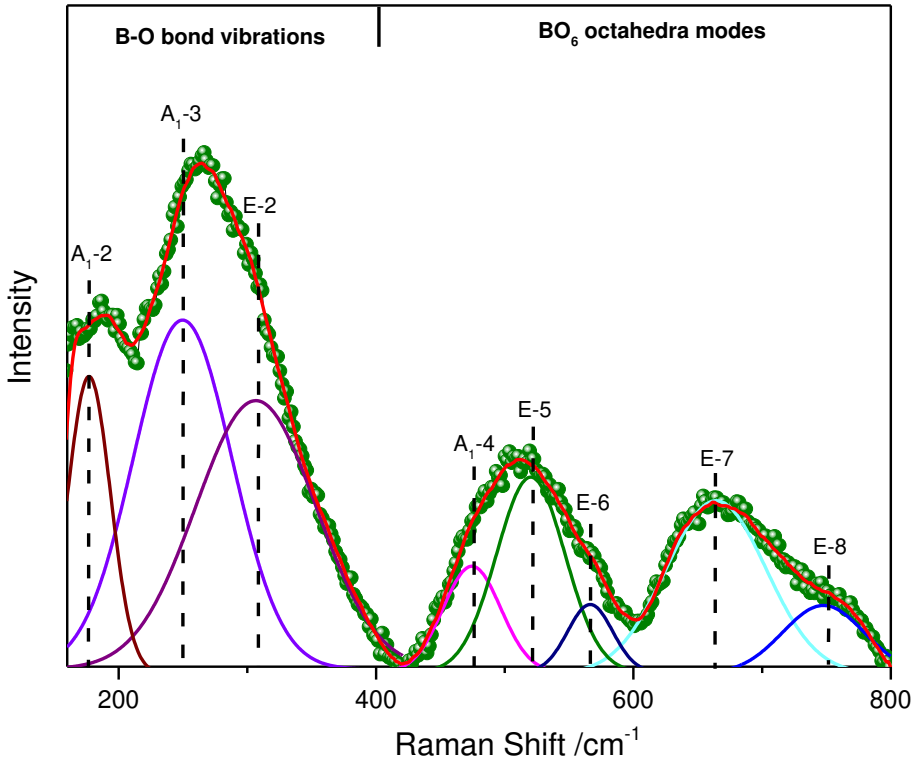

Figure V.7. Raman spectrum for the BFO-33BT sample obtained under optimal conditions.

V.2.2.2. Microstructural Characterization

The surface morphology of the fracture of BFO-33BT reactive flash sintered sample, as observed by SEM, is shown in **Figure V.8 (a)**. It corresponds to a well sintered material with a small amount of pores. **Figure V.8 (b)** shows a high-magnification SEM image of the fractured surface. It shows a peculiar microstructure with a bimodal grain size distribution, where small grains are located in the grain boundaries between larger grains. The mean value corresponding to the large grains is 3.4 ± 1 µm, while the mean value corresponding to the smaller grains is 0.4 ± 0.1 µm. The EDS mapping shows that Bi, Fe, Ba and Ti are uniformly dispersed within the flashed sample, both small and large grains show identical compositional ratios, confirming the chemical homogeneity of the BFO-33BT ceramic sample (**Figure V.8 (c-g)**).

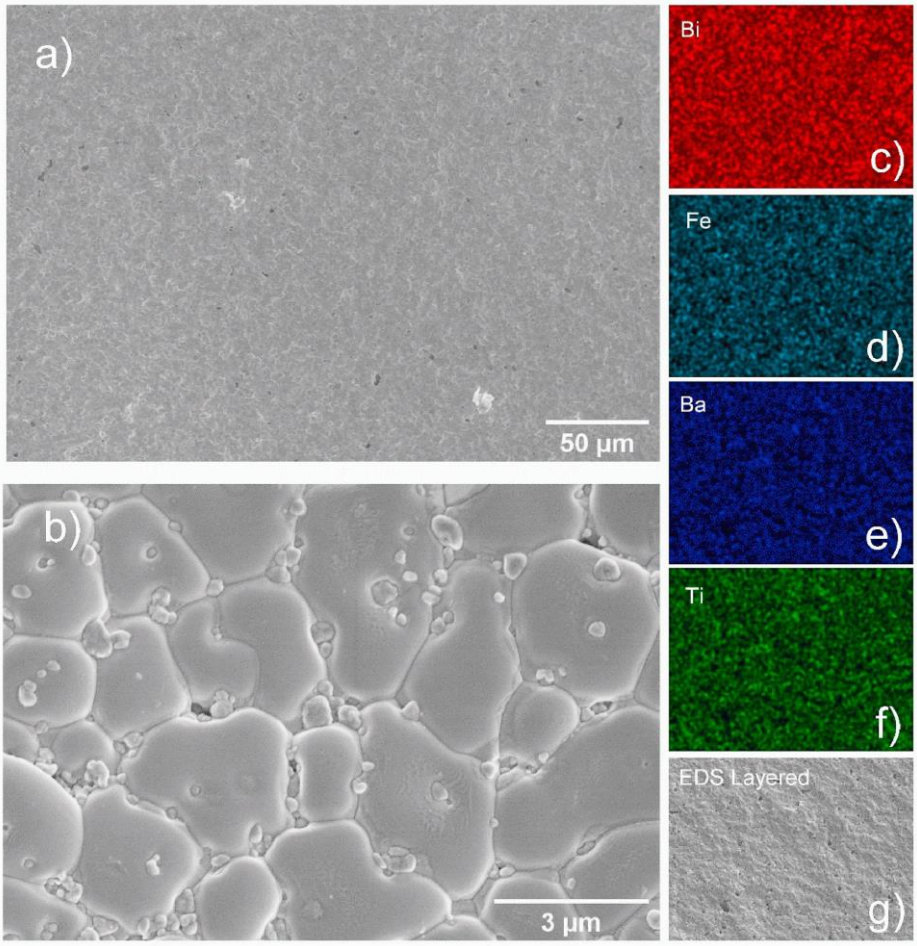

Figure V.8. SEM micrographs of BFO-33BT obtained under optimal conditions: a) surface morphology of the fracture surface, b) SEM image at high magnification. EDS elemental mapping of: c) Bi, d) Fe, e) Ba, f) Ti and g) EDS layered image.

V.2.2.3. Dielectric and Impedance Spectroscopy of BFO-33BT Flashed Sample

The dielectric properties of the BFO-33BT flashed sample were studied as a function of the temperature at selected frequencies and plotted in **Figure V.9**. Both the dielectric permittivity (**Figure V.9 (a)**) and dielectric loss (**Figure V.9 (b)**) appeared to increase clearly at temperatures above 200 °C, especially when measured at low frequencies. These effects are due to the increase of the electrical conductivity of the BFO-33BT flashed sample and to the associated space-charge polarization (**Liu *et al.*, 2018; Shankar *et al.*, 2020**). Thus, an extrinsic contribution to the dielectric permittivity due to the high dielectric loss is expected. A frequency-dependent dielectric anomaly appears slightly over 400 ℃ that can be attributed to the ferroelectric-paraelectric transition. The dielectric permittivity decreases and the peak shifts to higher temperatures with increasing frequencies. The strong dependence of the dielectric permittivity (ε') on frequency and the diffuse phase transition (T_c ~ 440 °C), suggests a relaxation phase transition behavior. This confirms previous finding by Singh et al. (**Singh, Kumar and Pandey, 2018**) having observed a relaxor-type ferroelectric behavior for samples prepared using $BaTiO_3$ as starting precursor. The dielectric loss significantly shifts to higher temperatures at higher frequencies, thereby suggesting mobile ions or vacancies might constitute the main conduction mechanism. Overall, the observed properties are consistent with previous reports (**Zhang *et al.*, 2014; Wang, Wang, *et al.*, 2018; Ji *et al.*, 2021; Xun *et al.*, 2021**).

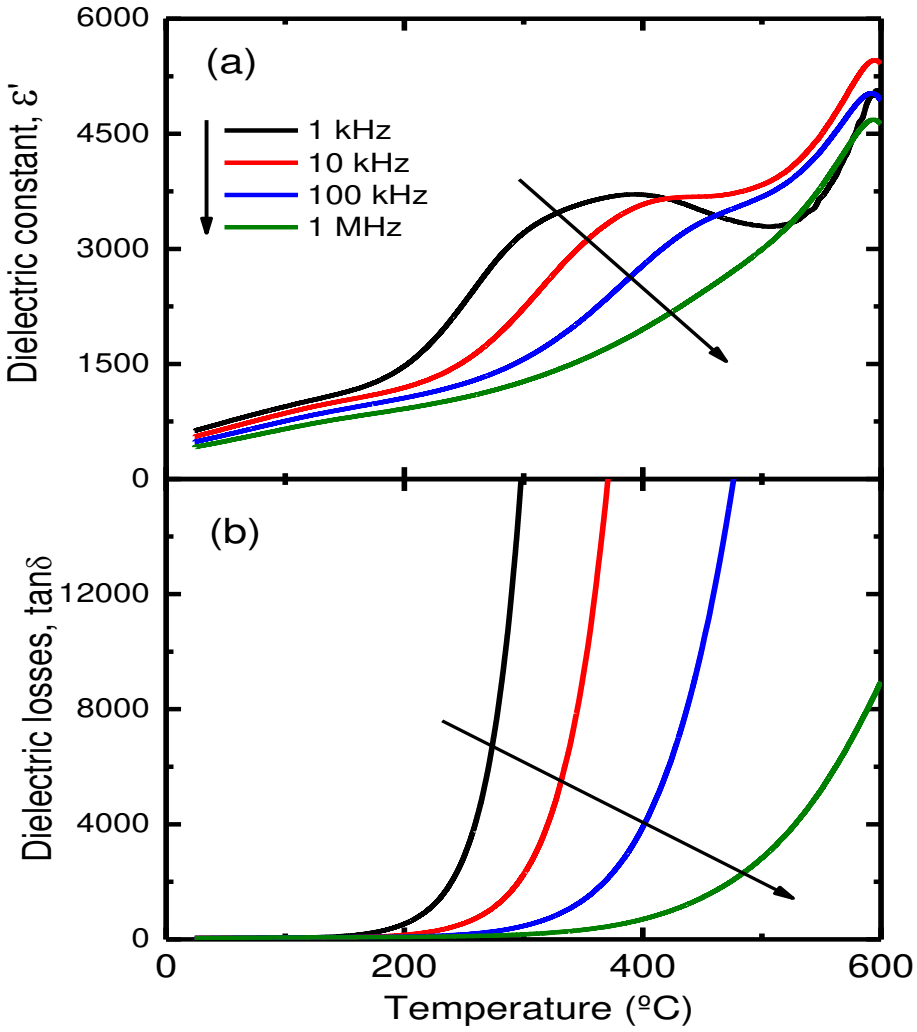

Figure V.9. Temperature dependent **a)** dielectric constant and **b)** loss for BFO–33BT obtained by reaction flash sintering.

In order to check the electrical homogeneity of the BFO-33BT flashed sample, impedance spectroscopy measurements were performed. Impedance data for BFO-33BT in air are displayed in **Figure V.10**. The Nyquist plot of BFO-33BT flashed sample is presented in **Figure V.10 (a)**. The flashed sample exhibits typical single semicircular arcs at all temperatures. As the temperature increases, the intercept of the semicircles on the Z' axis is smaller, indicating a decrease in the resistivity of the BFO-33BT sample. **Figure V.10 (b)** shows the Arrhenius plots of the conductivity for BFO–33BT. The average activation energy value, Ea, obtained from the plot slope, is found to be equal to 1.10 eV. This Ea value is quite similar to other results found in the literature for $BiFeO_3$-$BaTiO_3$ based ceramics (**Li, Cheng and Chen, 2017; Murakami *et al.*, 2018; Wang *et al.*, 2019**). Such value is consistent with reported activation energies of oxygen vacancies ($V_O^{\cdot\cdot}$), suggesting the conduction mechanism relies on oxygen vacancies that dominate the conductivity as elsewhere reported (**Deng *et al.*, 2017; Xun *et al.*, 2021**).

This mechanism can be further promoted by the synthesis method as it has been shown how ceramics prepared by flash sintering exhibit a significant amount of defects and ion vacancies (**Li *et al.*, 2019; Raj *et al.*, 2021**). To verify the existence of a short-range and a long-range ordering in BFO-33BT sample, spectroscopic plots of imaginary components of impedance, Z″, and modulus, M″, are plotted at 380 °C (**Figure V.10 (c)**). As seen from the graph, both peaks are almost in the same position, indicating good electrical homogeneity of BFO-33BT sample. The capacitance increases with increasing temperature (**Figure V.10 (d)**) and it is also noted that at all temperatures the capacitance shows a single capacitance plateau, with an approximate value range of 0.20–0.60 nF/cm. This indicates the presence of single electrical responses.

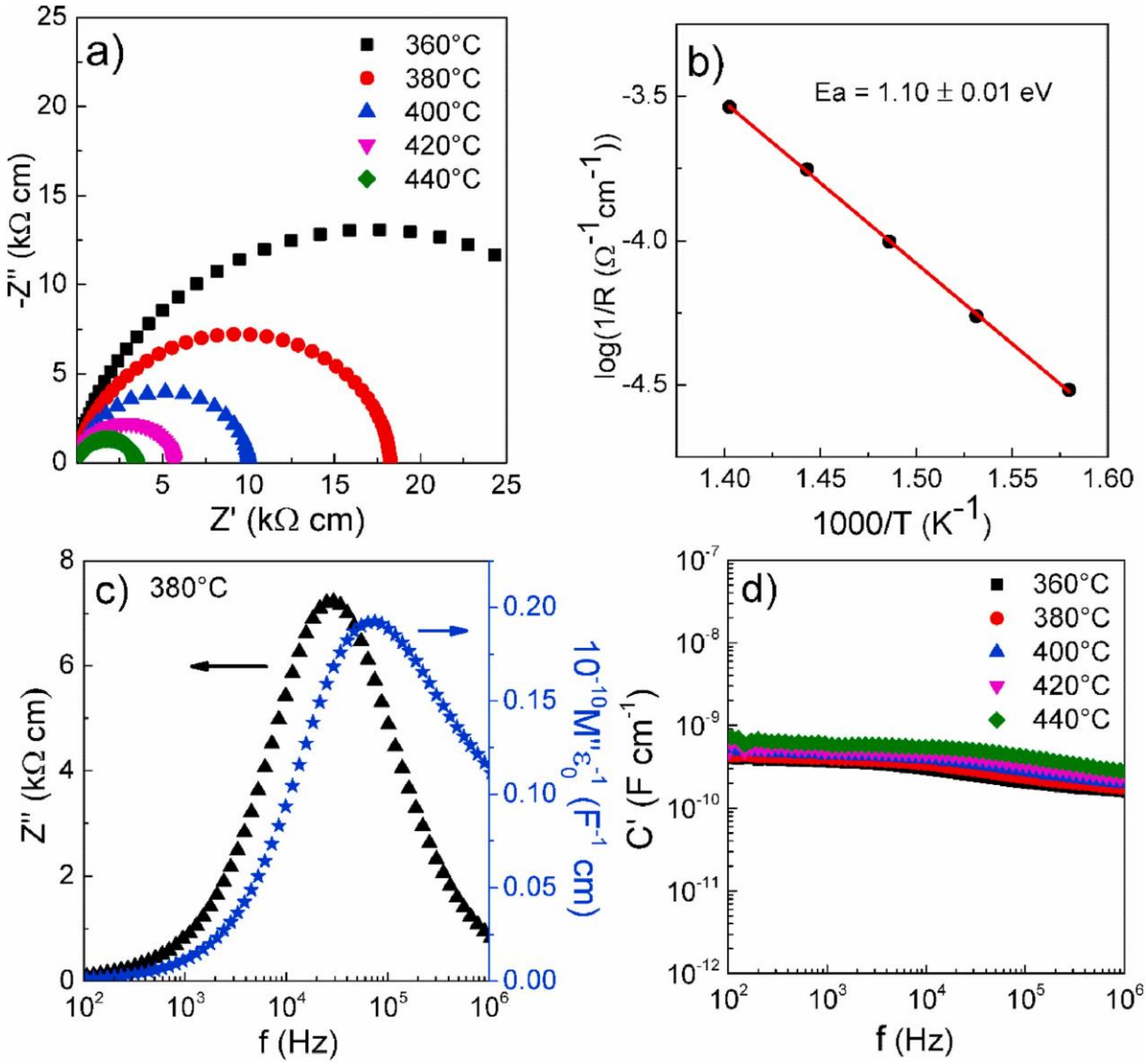

Figure V.10. Impedance data for BFO-33BT obtained by reaction flash sintering: **(a)** Nyquist plot, **(b)** Arrhenius plot of total electrical conductivity, **(c)** spectroscopic plots of imaginary components of impedance, Z″, and modulus, M″ at 380 °C and **(d)** capacitance versus frequency graph.

V.2.2.4. Ferroelectric and Piezoelectric Properties of BFO-33BT Flashed Sample

The room-temperature polarization hysteresis loops, measured under 60 kV/cm at 1 Hz are shown in **Figure V.11**. The loops exhibit poor saturation which can be attributed to the bimodal microstructure with relatively small grains obtained by reactive flash sintering. The large density of grain boundaries and defects as well as the consequently smaller ferroelectric domains hamper domain switching and limits maximum polarization (**Huo *et al.*, 2012**). The measured P_r, E_c and S_{max} are included in **Table V.2**. **Figure V.11** also displays the electric-field induced strain curves at 60 kV/cm. The sample exhibits the symmetric butterfly-shaped loops characteristic of ferroelectric materials. A small maximum strain of 0.034% is measured. All remnant and maximum polarization, as well as maximum strain appear slightly smaller than reported elsewhere, most probably due to the large number of small grains (**Wang, Fan, *et al.*, 2018; Xun *et al.*, 2021**). These measured properties are consistent with values reported in previous works (**Wang, *et al.*, 2018**).

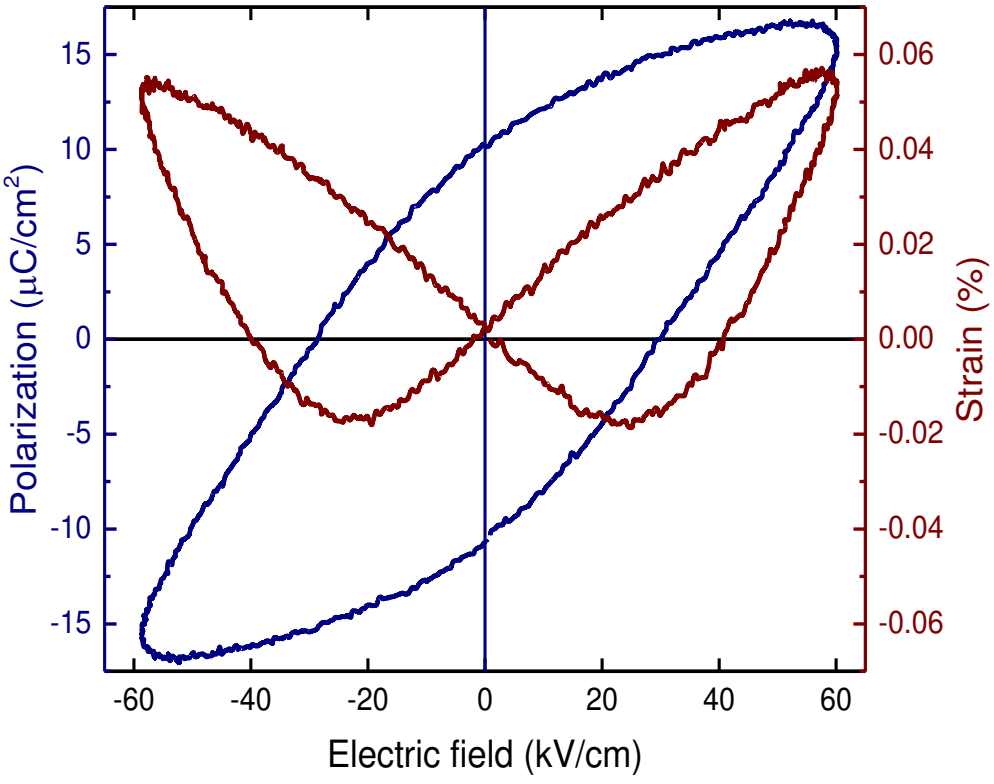

Figure V.11. P–E hysteresis loop and strain curve of BFO-33BT sample prepared by RFS.

Table V.2. Remnant polarization (P_r), coercive field (E_c) and strain max (S_{max}) for BFO-33BT prepared by reaction flash sintering. The piezoelectric coefficient (d_{33}), dielectric constant (ε') and loss (tanδ) at room temperature are also included.

Sample	**P_r (μC/cm^2)**	**E_c (kV/cm)**	**S_{max} (%)**	**d_{33} (pC/N)**	**ε'**	tanδ
BFO-33BT	3.0	24	0.034	30	620	0.07

Table V.2 also include the values of d_{33}, ε' and tanδ at room temperature. The measured piezoelectric constant d_{33} is 30 pC/N. The small value is a consequence of the low Pr, which hampers the piezoelectric properties.

V.2.3. Electrical Energy Consumption Analysis

A comparison of the electrical energy consumption during RFS and conventional preparation method (CM) of the material was performed. It was considered that the preparation of BFO-33BT by the conventional preparation method takes place in two stages, including synthesis (~800 °C for 2 h) and sintering (~1000 °C for 3 h) (**Zheng *et al.*, 2014; Cheng *et al.*, 2018; Tong *et al.*, 2018; Xun *et al.*, 2021**). Therefore, the total electric energy consumed in the conventional preparation of BFO-33BT is the quantity of energy consumed by the furnace during synthesis and sintering. Regarding the RFS, the energy consumed includes the energy required to heat up the furnace to the onset flash temperature (858 °C) and the energy delivered by the power supply during the flash (**Figure V.4 (b)**). **Figure V.12** shows the evolution of the electrical energy consumption during the RFS and CM experiment.

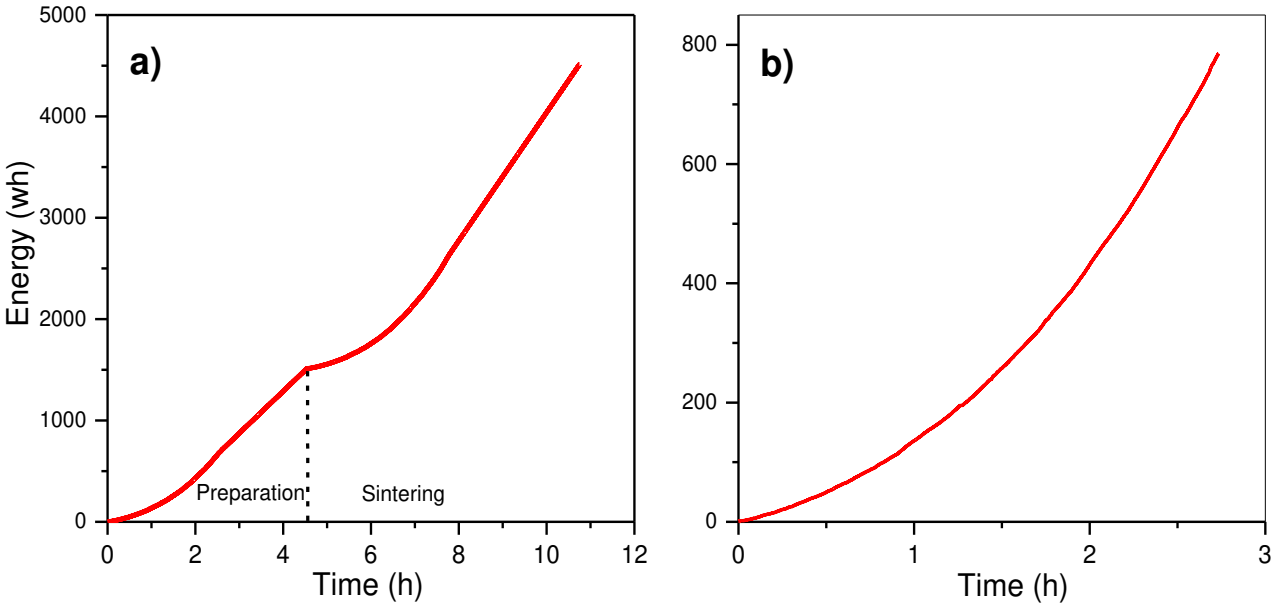

Figure V.12. Evolution of the electrical energy consumption during: **a)** CM and **b)** RFS of BFO-33BT.

Although at a laboratory scale, the results provide a proof of concept according to which the preparation by reaction flash sintering provides benefits regarding the electrical energy consumption. The total value of 788 Wh of electrical energy consumption in case of the experiment performed by RFS shows a decrease of about 82% compared to the electrical energy consumption of 4512 Wh for conventional preparation (**Figure V.13**).

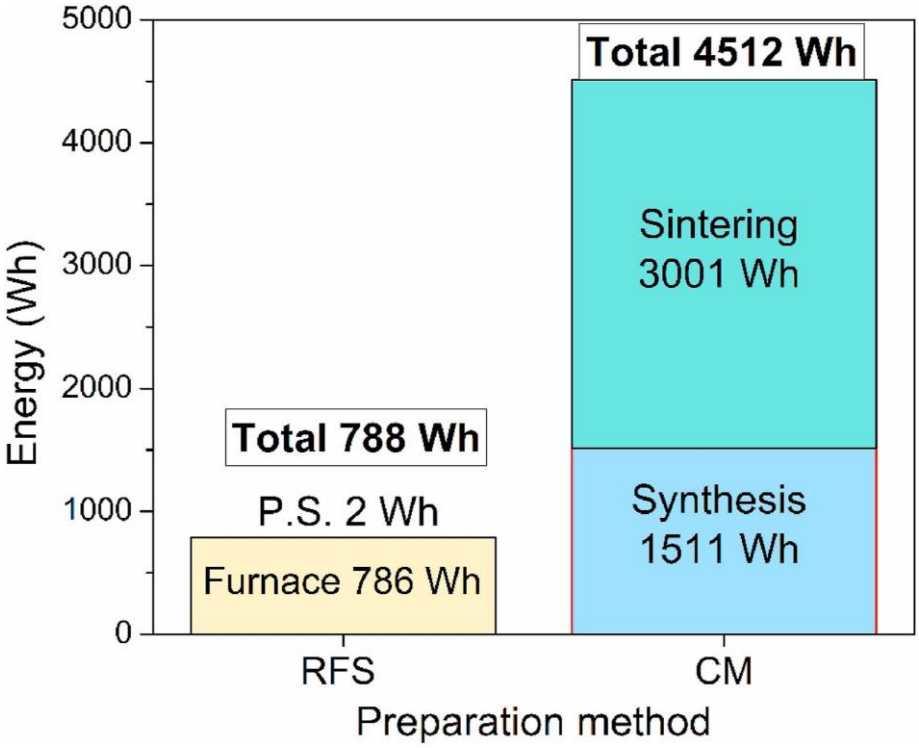

Figure V.13. Electrical energy consumption for the preparation of BFO-33BT by RFS and CM.

The experiments also confirmed the basic principles of flash sintering. Thus, energy is transferred directly to the materials, which provides rapid densification (<60 s) at moderate furnace temperatures. During the conventional preparation method, where energy is generated by external heating elements and transferred to the samples via convection, conduction and radiation, 67% of the total electrical energy is consumed in the sintering stage and the rest of 33% is used during the synthesis stage of BFO-33BT.

V.3. Conclusion

In this work, $0.67BiFeO_3$-$0.33BaTiO_3$ ceramic specimens have been synthesized and sintered in a single step by means of Reaction Flash Sintering technique. The starting powders, previously mechanically mixed to ensure homogeneous distribution, reacted during the flash to produce the stoichiometric solid solution and sintered to near full density in a matter of seconds at a temperature of 858 °C under a modest field of 35 V cm^{-1}. Conversely, conventional solid-state preparation procedures typically require two thermal treatments at temperatures around 1000 °C during hours, what often leads to sample inhomogeneity due to Bi volatilization. Reducing the temperature and length of the preparation method by RFS allows achieving pure perovskite structure without secondary phases nor impurities. With a 33% content in $BaTiO_3$, the structure lies in a MPB region where a rhombohedral R3c phase coexist with a pseudocubic phase.

The features of the RFS synthesis method, which greatly reduce the time the material is subjected to high temperatures, lead to a peculiar microstructure of the flashed ceramics. A bimodal grain size distribution with large 3 μm grains coexisting with small 0.4 μm grains is obtained. The electrical properties are largely in line with previous results, which validates RFS as energy and time saving technique for the synthesis and sintering of complex ceramics. Moreover, a comparison of the electrical energy consumption during the RFS and conventional preparation method was performed. It is demonstrated that the energy consumption is almost six times reduced, as compared with the conventional method, when RFS is used for the preparation of the $0.67BiFeO_3$-$0.33BaTiO_3$ ceramic.

General Conclusion and Perspectives

The present work focuses on two types of lead-free piezoceramics, namely $Ba_{(1-x)}Ca_xTiO_3$ (BCT) and (1-y)$BiFeO_3$-y$BaTiO_3$ (BFO-BT), as they appear to be promising candidates for the next generation of piezoceramics.

Based on the results obtained from kinetic analysis of Ca^{2+} incorporation into $BaTiO_3$ using DSC and XRD, it can be concluded that the Ca^{2+} was completely incorporated into $BaTiO_3$. Isoconversional methods, such as Fr, OFW and KAS, prove that the incorporation mechanism is simple and takes place in a single step. The combined kinetic analysis method was used to determine the kinetic parameters of the incorporation mechanism. The incorporation process was discovered to follow the A3 kinetic model, with an activation energy of 388 kJ/mol and a preexponential factor of 4.1 10^{17} min^{-1}. The reliability of the obtained kinetic parameters was demonstrated by comparing simulated and experimental kinetic curves.

Regarding the effect of Ca^{2+} doping on the properties of BCT piezoceramics. The samples, $Ba_{(1-x)}Ca_xTiO_3$ (BCT) (x=0 (BT) and x=15% (BCT15)), were prepared using the conventional solid-state preparation method. The XRD patterns confirm the formation of single-phase tetragonal perovskite structure in pure (BT) and in Ca-doped $BaTiO_3$ (BCT15) ceramic samples. XRD analysis also reveals that with the addition of Ca^{2+}, both the lattice parameters and unit cell volume decreased while the tetragonality increased, resulting in increased spontaneous tetragonal distortion and thus an enhancement of the piezoelectric and ferroelectric properties of BCT15. The obtained Raman spectra are consistent with those found in the literature, indicating that Ca^{2+} ions have been completely incorporated into the structure. SEM micrographs of the BCT15 ceramic sample show a dense and homogeneous microstructure. The dielectric measurements reveal that the BT and BCT15 samples behave as normal ferroelectrics. The present results show that Ca substitution has almost no effect on T_c. Due to the non-ferroelectric nature of $CaTiO_3$, the dielectric constant (ε') was reduced by the addition of Ca^{2+}.

In the case of 0.67$BiFeO_3$-0.33$BaTiO_3$ (BFO-33BT) system, the ceramic specimens were quickly synthesized and sintered in a single step using the Reactive Flash Sintering technique. To obtain a high-quality ceramic sample, the experimental flash conditions, namely the applied electric field and the current density limit, were first adjusted. The powder mixture reacted during the flash event to produce the stoichiometric solid solution and sintered to a high density in a matter of seconds at a temperature of 858 °C under a modest field of 35 V cm^{-1}. In contrast, conventional preparation typically requires two thermal treatment for hours, the first at around 800 ° C (for synthesis) and the second at 1000 ° C (for sintering), resulting in sample inhomogeneity

due to Bi volatilization. The RFS processing method reduces both the temperature and time of preparation to obtain a pure perovskite structure without secondary phases and impurities. With a $BaTiO_3$ content of 33%, the structure is located in a MPB region where a rhombohedral R3c phase coexists with a pseudocubic phase. The characteristics of the RFS synthesis method, which significantly reduce the time during which the material is subjected to elevated temperatures, result in a unique microstructure of the flashed ceramics. A bimodal grain size distribution was obtained, with large grains of 3 μm coexisting with small grains of 0.4 μm. The electrical properties are broadly consistent with previous studies, confirming RFS as an energy and time-saving technique for the synthesis and sintering of complex ceramics. Moreover, the electrical energy consumed during the RFS was compared to the energy consumed during the conventional preparation. It has been demonstrated that the energy consumption during preparation of BFO-33BT by the RFS method is almost six times lower when compared to the conventional method. This demonstrates that RFS is an energy efficient method to prepare piezoelectric ceramics.

Based on the results obtained, the main perspectives for the future work can be divided into two parts.

In the case of $BaTiO_3$-based piezoceramics, it would be worthy to complete this study by investigating the incorporation mechanism between Zr^{4+} and Ti^{4+} in the $BaZr_{(1-x)}Ti_xO_3$ (BZT) system. This can help in better understanding the formation mechanism of the pseudobinary ceramic system, BCT-xBZT, and optimizing its preparation.

Regarding $BiFeO_3$-$BaTiO_3$ piezoceramics, several suggestions could be considered for future work in order to improve the ferroelectric and piezoelectric properties:

- The partial substitution of Bi^{3+} in BFO-BT by an isovalent rare-earth ion, such as Sm^{3+}, can be a solution to significantly enhance the electrical properties of the ceramic samples.
- Through the results obtained, it was found that the use of $BaTiO_3$ as a starting powder humiliates the ferroelectric and piezoelectric properties of BFO-33BT flashed sample. Accordingly, a binary mixture of $BaCO_3$ (or BaO, BaO_2) and TiO_2 could be the good alternative for $BaTiO_3$ in order to improve the quality of the prepared ceramic samples.
- The milling time is also an important parameter that can be adjusted in future work..

Research Work and Activities

Research Work and Activities

International Publications

2. Taibi, A., Chaguetmi, S., Sánchez-Jiménez, P. E., Perejón, A., García, J. E., Satha, H., and Pérez-Maqueda, L. A., "Pure perovskite $BiFeO_3$–$BaTiO_3$ ceramics prepared by reaction flash sintering of Bi_2O_3–Fe_2O_3–$BaTiO_3$ mixed powders", *Ceramics international*, 47 (2021) 26947–26954. https://doi.org/10.1016/j.ceramint.2021.06.108.

1. Taibi, A., Chaguetmi, S., Louaer, A., Layachi, A. and Satha, H., "Barium calcium titanate solid solution: Non-isothermal kinetic analysis of Ca^{2+} incorporation into $BaTiO_3$", *Thermochimica Acta*. 680 (2019) 178356. https://doi.org/10.1016/j.tca.2019.178356.

International Communications

5. Taibi, A., Gil-Gonzalez, E., Chaguetmi, S., Sánchez-Jiménez, P.E., Perejón, A., García, J.E., Satha, H., Pérez-Maqueda, L.A., 2021. "New synthesis strategy of $BiFeO_3$-$BaTiO_3$ electroceramics for high temperature applications", *6th Central and Eastern European Conference on Thermal Analysis and Calorimetry & 15th Mediterranean Conference on Calorimetry and Thermal Analysis (CEEC-TAC6 & Medicta 2021)*, 20-24 July 2021, Split, Croatia. (**Poster** presentation)

4. Louaer, A., **Taibi, A.**, Layachi, A., Chaguetmi, S. and Satha, H., 2018. "Synthesis, thermal and structural properties of new PZT doped ceramic", *Fourth International Conference on Energy, Materials, Applied Energetics and Pollution (ICEMAEP-2018)*, 29-30 April 2018, Constantine-Algeria. (**Poster** presentation)

3. Taibi, A., Louaer, A., Layachi, A., Chaguetmi, S. and Satha, H., 2018. "Thermal analysis and XRD structural properties of a new doped PZT ternary system piezoelectric ceramic near morphotropic phase boundary", *Fourth International Conference on Energy, Materials, Applied Energetics and Pollution (ICEMAEP-2018)*, 29-30 April 2018, Constantine-Algeria. (**Poster** presentation)

2. Louaer, A., **Taibi, A.**, Layachi, A., Chaguetmi, S. and Satha, H., 2018. "Synthèse et caractérisation d'une nouvelle céramique de type PZT dopé". *International Symposium on Materals Chemistry (ISyMC-2018)*, 19-21 March 2018, Boumerdes-Algeria. (**Poster** presentation)

1. Taibi, A., Louaer, A., Layachi, A., Chaguetmi, S. and Satha, H., 2018. "Synthèse, analyse thermique et propriété structurale de céramique PZT modifiée proche de la frontière morphotropique de phase". *International Symposium on Materials Chemistry (ISyMC-2018)*, 19-21 March 2018, Boumerdes-Algeria. (**Poster** presentation)

National communications

3. Taibi, A., Chaguetmi, S., Satha, H., Pérez-Maqueda, L.A., 2021. "Isoconversional analysis on the non-isothermal incorporation kinetics of Ca^{2+} into $BaTiO_3$ in Barium Calcium Titanate (BCT)", *Grupo Especializado de Calorimetría y Análisis Térmico (GEGAT 2021) Young Researchers Workshop*, June 2021, University of Girona, Spain. (**Oral** presentation)

2. Taibi, A., Chaguetmi, S., Layachi, A. Louaer, A., and Satha, H., "Phase formation of $Ba_{0.85}Ca_{0.15}TiO_3$ piezoelectric ceramic prepared via solid state reaction", *Journée Nationale: Etude des Matériaux : Elaboration et Modélisation (JEMEM'2018)*, Décembre 2018, Guelma –Algeria. (**Oral** presentation)

1. Taibi, A., Chaguetmi, S., Louaer, A., Layachi, A. and Satha, H., 2019. "Phase evolution of $0.7BiFeO_3$-$0.3BaTiO_3$ solid solution prepared via the solid-state reaction", *1er Séminaire National de Physique et Chimie des Matériaux (SNPCM12018)*, 28-29 November 2018, ENSET Skikda Algeria. (**Poster** presentation)

References

References

Acosta, M. *et al.* (2017) 'BaTiO$_3$-based piezoelectrics: Fundamentals, current status, and perspectives', *Applied Physics Reviews*, 4(4), p. 041305. doi: 10.1063/1.4990046.

Aghili, S., Panjepour, M. and Meratian, M. (2017) 'Kinetic analysis of formation of boron trioxide from thermal decomposition of boric acid under non-isothermal conditions', *Journal of Thermal Analysis and Calorimetry 2017 131:3*, 131(3), pp. 2443–2455. doi: 10.1007/s10973-017-6740-3.

Ahmadi, N., Kharaziha, M. and Labbaf, S. (2019) '(BaCa)TiO$_3$ nanopowder: Synthesis and their electrical and biological characteristics', *Materials Chemistry and Physics*, 226, pp. 263–271. doi: 10.1016/j.matchemphys.2018.12.081.

Akahira, T. and Sunose (1971) 'Method of determining activation deterioration constant of electrical insulating materials', *Res. Rep. Chiba. Inst. Technol. (Sci. Technol.)*, pp. 22–31.

Ako, M. *et al.* (2019) 'Formation of Ba$_{1-x}$Ca$_x$TiO$_3$ solid solutions beyond the solubility limit by "sputter-anneal" method', *Thermochimica Acta*, 679, p. 178339. doi: 10.1016/j.tca.2019.178339.

Al-Taie, A. A., Al-Shakarchi, E. K. and Kamel, M. (2018) 'In Situ Preparation of Ba$_{0.75}$Ca$_{0.25}$ TiO$_3$ Nanoparticles by Hydrothermal Method', *Open Access Journal of Physics*, 2(1), pp. 39–43. doi: Available at: https://www.academia.edu/36597632 (Accessed: 28 February 2022).

An, G. *et al.* (2021) 'Rapid preparation of Bi$_{0.5}$Na$_{0.5}$TiO$_3$ ceramics by reactive flash sintering of Bi$_2$O$_3$-NaCO$_3$-TiO$_2$ mixed powders', *Journal of the European Ceramic Society*. doi: 10.1016/j.jeurceramsoc.2021.11.053.

Araújo, V. D. *et al.* (2014) 'Effect of calcium on the structural properties of Ba$_{(1-x)}$Ca$_x$TiO$_3$ particles synthesized by complex polymerization method', *Journal of Materials Science 2014 49:7*, 49(7), pp. 2875–2878. doi: 10.1007/S10853-013-7993-2.

Avila, V. *et al.* (2020) 'Reactive flash sintering of the complex oxide Li$_{0.5}$La$_{0.5}$TiO$_3$ starting from an amorphous precursor powder', *Scripta Materialia*, 176, pp. 78–82. doi: 10.1016/j.scriptamat.2019.09.037.

Avila, V. *et al.* (2021) 'Phase evolution during reactive flash sintering of Li$_{6.25}$Al$_{0.25}$La$_3$Zr$_2$O$_{12}$ starting from a chemically prepared powder', *Journal of the European Ceramic Society*, 41(8), pp. 4552–4557. doi: 10.1016/j.jeurceramsoc.2021.02.054.

Avila, V. and Raj, R. (2019) 'Reactive flash sintering of powders of four constituents into a single phase of a complex oxide in a few seconds below 700°C', *Journal of the American Ceramic Society*, 102(11), pp. 6443–6448. doi: 10.1111/jace.16625.

Bao, H. *et al.* (2010) 'A modified lead-free piezoelectric BZT–xBCT system with higher T$_C$', *Journal of Physics D: Applied Physics*, 43(46), p. 465401. doi: 10.1088/0022-3727/43/46/465401.

Bechmann, R. (1956) 'Elastic, Piezoelectric, and Dielectric Constants of Polarized Barium Titanate Ceramics and Some Applications of the Piezoelectric Equations', *The Journal of the Acoustical Society of America*, 28(3), p. 347. doi: 10.1121/1.1908324.

Bell, A. J. and Deubzer, O. (2018) 'Lead-free piezoelectrics—The environmental and regulatory issues', *MRS Bulletin*, 43(8), pp. 581–587. doi: 10.1557/mrs.2018.154.

Berlincourt, D. (1998) 'Piezoelectric ceramics: Characteristics and applications', *The Journal of the Acoustical Society of America*, 70(6), p. 1586. doi: 10.1121/1.387224.

Bernache-Assollant, D. and Bonnet, J.-P. (2005) 'Frittage: aspects physico-chimiques Partie 1: frittage en phase solide', *Techniques de l'ingénieur. Sciences fondamentales*, AFP4(AF6620), p. AF6620.1-AF620.20. Available at: https://hal-emse.ccsd.cnrs.fr/emse-00497555 (Accessed: 4 January 2022).

Bezerra, G. V. P. and Cabral, A. A. (2021) 'Model-free and model-fitting analysis applied to the non-isothermal crystallization kinetics of a SrO-CaO-B_2O_3-TiO_2-SiO_2 glass sealant for SOFCs', *Journal of Non-Crystalline Solids*, 572, p. 121113. doi: 10.1016/j.jnoncrysol.2021.121113.

Boonchom, B. (2008) 'Kinetics and Thermodynamic Properties of the Thermal Decomposition of Manganese Dihydrogenphosphate Dihydrate', *Journal of Chemical and Engineering Data*, 53(7), pp. 1533–1538. doi: 10.1021/je800103w.

Boskabady, M. *et al.* (2018) 'The effect of environmental lead exposure on human health and the contribution of inflammatory mechanisms, a review', *Environment International*, 120, pp. 404–420. doi: 10.1016/j.envint.2018.08.013.

Bots, P. *et al.* (2012) 'Mechanistic Insights into the Crystallization of Amorphous Calcium Carbonate (ACC)', *Crystal Growth and Design*, 12(7), pp. 3806–3814. doi: 10.1021/cg300676b.

Bouzidi, H. *et al.* (2019) 'Structural, Raman, ferroelectric and magnetic studies of the (1-x)BF-xBCT multiferroic system', *Journal of Alloys and Compounds*, 772, pp. 877–884. doi: 10.1016/j.jallcom.2018.09.105.

Brown, M.E., Dollimore, D. and Galwey, A. . (1980) *Reactions in the Solid State*. 1st edn. Elsevier Science. Available at: https://www.elsevier.com/books/reactions-in-the-solid-state/brown/978-0-444-41807-4 (Accessed: 31 October 2021).

Brown, M. E. *et al.* (2000) 'Computational aspects of kinetic analysis: Part A: The ICTAC kinetics project-data, methods and results', *Thermochimica Acta*, 355(1–2), pp. 125–143. doi: 10.1016/S0040-6031(00)00443-3.

Burnham, A. K. and Dinh, L. N. (2007) 'A comparison of isoconversional and model-fitting approaches to kinetic parameter estimation and application predictions', *Journal of Thermal Analysis and Calorimetry 2007 89:2*, 89(2), pp. 479–490. doi: 10.1007/s10973-006-8486-1.

Buscaglia, V. *et al.* (2014) 'Average and local atomic-scale structure in $BaZr_xTi_{1-x}O_3$ (x = 0.10, 0.20, 0.40) ceramics by high-energy x-ray diffraction and Raman spectroscopy', *Journal of Physics: Condensed Matter*, 26(6), p. 065901. doi: 10.1088/0953-8984/26/6/065901.

Buscaglia, V., Buscaglia, M. T. and Canu, G. (2021) '$BaTiO_3$-Based Ceramics: Fundamentals, Properties and Applications', *Encyclopedia of Materials: Technical Ceramics and Glasses*, pp. 311–344. doi: 10.1016/b978-0-12-803581-8.12132-0.

Caliman, L. B. *et al.* (2016) 'Flash sintering of ionic conductors: The need of a reversible electrochemical reaction', *Journal of the European Ceramic Society*, 36(5), pp. 1253–1260. doi: 10.1016/j.jeurceramsoc.2015.12.005.

Campos, J. V. *et al.* (2021) 'On the Arrhenius-like behavior of conductivity during flash sintering of 3 mol% yttria stabilized zirconia ceramics', *Scripta Materialia*, 203, p. 114093. doi: 10.1016/j.scriptamat.2021.114093.

Chang, M. C. (2000) 'Raman study for $(Ba_{1-x}Ca_x)TiO_3$ and $Ba(Ti_{1-y}Ca_y)O_3$ crystalline ceramics Three Dimensionally Ordered Microstructure of Polycrystalline Materials with micro/meso porosity View project', *Article in Journal of Materials Science Letters*. doi: 10.1023/a:1006732628003.

Chawla, A. *et al.* (2018) 'Structural, surface morphological and ferroelectric properties of Ca doped $BaTiO_3$ solid solutions', *AIP Conference Proceedings*, 2009(1), p. 020016. doi: 10.1063/1.5052085.

Chen, C. *et al.* (2015) 'Effect of Ca substitution sites on dielectric properties and relaxor behavior of Ca doped barium strontium titanate ceramics', *Journal of Materials Science: Materials in Electronics*, 26(4), pp. 2486–2492. doi: 10.1007/s10854-015-2710-3.

Chen, J. *et al.* (2020) 'Excellent thermal stability and aging behaviors in $BiFeO_3$-$BaTiO_3$ piezoelectric ceramics with rhombohedral phase', *Journal of the American Ceramic Society*, 103(1), pp. 374–381. doi: 10.1111/jace.16755.

Chen, J. R. *et al.* (2008) 'X-ray diffraction analysis and specific heat capacity of $(Bi_{1-x}La_x)FeO_3$ perovskites', *Journal of Alloys and Compounds*, 459(1–2), pp. 66–70. doi: 10.1016/j.jallcom.2007.05.034.

Cheng, S. *et al.* (2018) 'Enhanced insulating and piezoelectric properties of $0.7BiFeO_3$-$0.3BaTiO_3$ lead-free ceramics by optimizing calcination temperature: Analysis of Bi^{3+} volatilization and phase structures', *Journal of Materials Chemistry C*, 6(15), pp. 3982–3989. doi: 10.1039/c8tc00329g.

Clemenceau, T. *et al.* (2019) 'Flash sintering of Li-ion conducting ceramic in a few seconds at 850 °C', *Scripta Materialia*, 172, pp. 1–5. doi: 10.1016/j.scriptamat.2019.06.038.

Coelho, R. J. and Aladenize, B. (1993) 'Les diélectriques : propriétés diélectriques des matériaux isolants', p. 230. Available at: https://catalogue-bu.u bourgogne.fr/permalink/33ub_inst/1s43pht/alma991000621489706659 (Accessed: 28 February 2022).

Cologna, M., Francis, J. S. C. and Raj, R. (2011) 'Field assisted and flash sintering of alumina and its relationship to conductivity and MgO-doping', *Journal of the European Ceramic Society*, 31(15), pp. 2827–2837. doi: 10.1016/j.jeurceramsoc.2011.07.004.

Cologna, M., Prette, A. L. G. and Raj, R. (2011) 'Flash-Sintering of Cubic Yttria-Stabilized Zirconia at 750°C for Possible Use in SOFC Manufacturing', *Journal of the American Ceramic Society*, 94(2), pp. 316–319. doi: 10.1111/j.1551-2916.2010.04267.x.

Cologna, M., Rashkova, B. and Raj, R. (2010) 'Flash Sintering of Nanograin Zirconia in <5 s at 850°C', *Journal of the American Ceramic Society*, 93(11), pp. 3556–3559. doi: 10.1111/J.1551-2916.2010.04089.X.

Criado, J. M., Málek, J. and Ortega, A. (1989) 'Applicability of the master plots in kinetic analysis of non-isothermal data', *Thermochimica Acta*, 147(2), pp. 377–385. doi: 10.1016/0040-6031(89)85192-5.

Dancer, C. E. J. (2016) 'Flash sintering of ceramic materials', *Materials Research Express*, 3(10), p. 102001. doi: 10.1088/2053-1591/3/10/102001.

Deng, X. Z. *et al.* (2017) 'Crystal structure, impedance, and multiferroic property of $SrZrO_3$ and MnO_2 modified $0.725BiFeO_3$–$0.275BaTiO_3$ ceramics', *Ceramics International*, 43(17), pp. 14748–14755. doi: 10.1016/j.ceramint.2017.07.215.

Dobal, P. S. *et al.* (2001) 'Micro-Raman scattering and dielectric investigations of phase transition behavior in the $BaTiO_3$–$BaZrO_3$ system', *Journal of Applied Physics*, 89(12), p. 8085. doi: 10.1063/1.1369399.

Dong, Y. and Chen, I.-W. (2015) 'Predicting the Onset of Flash Sintering', *Journal of the American Ceramic Society*, 98(8), pp. 2333–2335. doi: 10.1111/jace.13679.

Downs, J. A. and Sglavo, V. M. (2013) 'Electric Field Assisted Sintering of Cubic Zirconia at 390°C', *Journal of the American Ceramic Society*, 96(5), pp. 1342–1344. doi: 10.1111/jace.12281.

Doyle, C. D. (1961) 'Kinetic analysis of thermogravimetric data', *Journal of Applied Polymer Science*, 5(15), pp. 285–292. doi: 10.1002/app.1961.070051506.

Doyle, C. D. (1962) 'Estimating isothermal life from thermogravimetric data', *Journal of Applied Polymer Science*, 6(24), pp. 639–642. doi: 10.1002/app.1962.070062406.

Doyle, C. D. (1965) 'Series Approximations to the Equation of Thermogravimetric Data', *Nature 1965 207:4994*, 207(4994), pp. 290–291. doi: 10.1038/207290a0.

Dukor, R. K. (2006) 'Vibrational Spectroscopy in the Detection of Cancer', *Handbook of Vibrational Spectroscopy*. doi: 10.1002/0470027320.s8107.

Erol, M., Küçükbayrak, S. and Ersoy-Meriçboyu, A. (2009) 'The application of differential thermal analysis to the study of isothermal and non-isothermal crystallization kinetics of coal fly ash based glasses', *Journal of Non-Crystalline Solids*, 355(9), pp. 569–576. doi: 10.1016/j.jnoncrysol.2009.01.023.

Flückiger, U. and Arend, H. (1978) 'On the preparation of pure, doped and reduced $KNbO_3$ single crystals', *Journal of Crystal Growth*, 43(4), pp. 406–416. doi: 10.1016/0022-0248(78)90338-x.

Flynn, J. H. and Wall, L. A. (1966) 'General Treatment of the Thermogravimetry of Polymers', *Journal of Research of the National Bureau of Standards. Section A, Physics and Chemistry*, 70A(6), p. 487. doi: 10.6028/JRES.070A.043.

Francisco J. Gotor, † *et al.* (2000) 'Kinetic Analysis of Solid-State Reactions: The Universality of Master Plots for Analyzing Isothermal and Nonisothermal Experiments', *Journal of Physical Chemistry A*, 104(46), pp. 10777–10782. doi: 10.1021/jp0022205.

Freire, J. D. and Katiyar, R. S. (1988) 'Lattice dynamics of crystals with tetragonal <span class', *Physical Review B*, 37(4), p. 2074. doi: 10.1103/physrevb.37.2074.

Friedman, H. L. (1964) 'Kinetics of thermal degradation of char-forming plastics from thermogravimetry. Application to a phenolic plastic', *Journal of Polymer Science Part C: Polymer Symposia*, 6(1), pp. 183–195. doi: 10.1002/polc.5070060121.

Fu, D. and Itoh, M. (2011) 'Ferroelectricity in Silver Perovskite Oxides', *Ferroelectrics - Material Aspects*. doi: 10.5772/17261.

Fu, D., Itoh, M. and Koshihara, S. (2008) 'Crystal growth and piezoelectricity of $BaTiO_3$–$CaTiO_3$ solid solution', *Applied Physics Letters*, 93(1), p. 012904. doi: 10.1063/1.2956400.

Gajović, A. *et al.* (2013) 'Temperature-dependent Raman spectroscopy of $BaTiO_3$ nanorods synthesized by using a template-assisted sol–gel procedure', *Journal of Raman Spectroscopy*, 44(3), pp. 412–420. doi: 10.1002/jrs.4206.

Gao, X. and Dollimore, D. (1993) 'The thermal decomposition of oxalates: Part 26. A kinetic study of the thermal decomposition of manganese(II) oxalate dihydrate', *Thermochimica Acta*, 215(C), pp. 47–63. doi: 10.1016/0040-6031(93)80081-k.

Ghaderi, F. *et al.* (2016) 'DSC kinetic study of the incompatibility of doxepin with dextrose: Application to pharmaceutical preformulation studies', *Journal of Thermal Analysis and Calorimetry*, 123(3), pp. 2081–2090. doi: 10.1007/s10973-015-4995.

Gil-González, E., Perejón, A., Sánchez-Jiménez, P. E., Medina-Carrasco, S., *et al.* (2018) 'Crystallization Kinetics of Nanocrystalline Materials by Combined X-ray Diffraction and Differential Scanning Calorimetry Experiments', *Crystal Growth & Design*, 18(5), pp. 3107–3116. doi: 10.1021/acs.cgd.8b00241.

Gil-González, E., Perejón, A., Sánchez-Jiménez, P. E., Sayagués, M. J., *et al.* (2018) 'Phase-pure $BiFeO_3$ produced by reaction flash-sintering of Bi_2O_3 and Fe_2O_3', *Journal of Materials Chemistry A*, 6(13), pp. 5356–5366. doi: 10.1039/c7ta09239c.

Gil-González, E. *et al.* (2020) 'Control of experimental conditions in reaction flash-sintering of complex stoichiometry ceramics', *Ceramics International*, 46(18), pp. 29413–29420. doi: 10.1016/j.ceramint.2020.05.091.

Goldschmidt, V. M. (1926) 'Die Gesetze der Krystallochemie', *Naturwissenschaften 1926 14:21*, 14(21), pp. 477–485. doi: 10.1007/bf01507527.

Grasso, S., Sakka, Y. and Maizza, G. (2009) 'Electric current activated/assisted sintering (ECAS): a review of patents 1906–2008', *Science and Technology of Advanced Materials*, 10(5), p. 053001. doi: 10.1088/1468-6996/10/5/053001.

Gupta, S. (2021) 'Introduction to ferroelectrics and related materials', *Ferroelectric Materials for Energy Harvesting and Storage*, pp. 1–41. doi: 10.1016/b978-0-08-102802-5.00001-7.

Habib, M. *et al.* (2020) 'Phase evolution and origin of the high piezoelectric properties in lead-free $BiFeO_3$–$BaTiO_3$ ceramics', *Ceramics International*, 46(14), pp. 22239–22252. doi: 10.1016/j.ceramint.2020.05.301.

Hassan, A. A. *et al.* (2014) 'Formation-Mechanism-of-Barium-Titanate-by-Solid-State Reactions Formation Mechanism of Barium Titanate by Solid-State Reactions', *International Journal of Scientific & Engineering Research*, 5(7). Available at: http://www.ijser.org (Accessed: 1 November 2021).

Hatakeyama, T., Quinn, F. and Wiley, J. (1999) 'Thermal Analysis Fundamentals and Applications to Polymer Science Second Edition'. Available at: http://www.wiley.co.ukorhttp//www.wiley.com (Accessed: 31 October 2021).

Huang, G. *et al.* (2016) 'Thermally stable $Ba_{0.8}Ca_{0.2}TiO_3$-$Bi(Mg_{0.5}Zr_{0.5})O_3$ solid solution with low dielectric loss in a broad temperature usage range', *Journal of Materials Science: Materials in Electronics*, 27. doi: 10.1007/s10854-016-4599-x.

Huang, Y. *et al.* (2017) 'Multiphase coexistence and enhanced electrical properties in (1-x-y)$BaTiO_3$-x$CaTiO_3$-y$BaZrO_3$ lead-free ceramics', *Ceramics International*, 43(16), pp. 13516–13523. doi: 10.1016/j.ceramint.2017.07.057.

Huo, S. *et al.* (2012) 'Grain size effects on the ferroelectric and piezoelectric properties of $Na_{0.5}K_{0.5}NbO_3$ ceramics prepared by pechini method', *Journal of the American Ceramic Society*, 95(4), pp. 1383–1387. doi: 10.1111/j.1551-2916.2011.04992.x.

Hwan Lee, M. *et al.* (2015) 'High-Performance Lead-Free Piezoceramics with High Curie Temperatures', *Advanced Materials*, 27(43), pp. 6976–6982. doi: 10.1002/adma.201502424.

IEEE Standard on Piezoelectricity (1988) 'IEEE Standard on Piezoelectricity: An American National Standard', *ANSI/IEEE Std 176-1987*, pp. 8–10. Available at: http://ieeexplore.ieee.org/stamp/stamp.jsp?tp=&arnumber=26560&isnumber=1019 (Accessed: 11 December 2021).

Janković, B., Mentus, S. and Jelić, D. (2009) 'A kinetic study of non-isothermal decomposition process of anhydrous nickel nitrate under air atmosphere', *Physica B: Condensed Matter*, 404(16), pp. 2263–2269. doi: 10.1016/j.physb.2009.04.024.

Jha, S. K. *et al.* (2018) 'In-situ observation of oxygen mobility and abnormal lattice expansion in ceria during flash sintering', *Ceramics International*, 44(13), pp. 15362–15369. doi: 10.1016/j.ceramint.2018.05.186.

Ji, C. *et al.* (2021) 'Influence of sintering method on microstructure, electrical and magnetic properties of $BiFeO_3$–$BaTiO_3$ solid solution ceramics', *Materials Today Chemistry*, 20, p. 100419. doi: 10.1016/j.mtchem.2020.100419.

Jia, Y. *et al.* (2019) 'Fabrication of lead zirconate titanate ceramics by reaction flash sintering of PbO-ZrO_2-TiO_2 mixed oxides', *Journal of the European Ceramic Society*, 39(13), pp. 3915–3919. doi: 10.1016/j.jeurceramsoc.2019.05.044.

Joraid, A. A. (2007) 'Estimating the activation energy for the non-isothermal crystallization of an amorphous $Sb_{9.1}Te_{20.1}Se_{70.8}$ alloy', *Thermochimica Acta*, 456(1), pp. 1–6. doi: 10.1016/j.tca.2007.01.023.

Kanzig, W. (2011) 'History of ferroelectricity', 74(1), pp. 285–291. doi: 10.1080/00150198708201308.

Karakuscu, A. *et al.* (2012) 'Defect Structure of Flash-Sintered Strontium Titanate', *Journal of the American Ceramic Society*, 95(8), pp. 2531–2536. doi: 10.1111/j.1551-2916.2012.05240.x.

Karan, N. K. *et al.* (2009) 'Raman spectral studies of Zr^{4+}-rich $BaZr_xTi_{1-x}O_3$($0.5 \leqslant x \leqslant 1.00$) phase diagram', *Journal of Raman Spectroscopy*, 40(4), pp. 370–375. doi: 10.1002/jrs.2134.

Keeble, D. S. *et al.* (2013) 'Revised structural phase diagram of ($Ba_{0.7}Ca_{0.3}TiO_3$)-($BaZr_{0.2}Ti_{0.8}O_3$)', *Applied Physics Letters*, 102(9), p. 092903. doi: 10.1063/1.4793400.

Kim, D. J., Lee, M. H. and Song, T. K. (2019) 'Comparison of multi-valent manganese oxides (Mn^{4+}, Mn^{3+}, and Mn^{2+}) doping in $BiFeO_3$-$BaTiO_3$ piezoelectric ceramics', *Journal of the European Ceramic Society*, 39(15), pp. 4697–4704. doi: 10.1016/j.jeurceramsoc.2019.07.013.

Kim, S. *et al.* (2017) 'Structural and electrical characteristics of potential candidate lead-free BiFeO3-BaTiO3 piezoelectric ceramics', *Journal of Applied Physics*, 122(16), p. 164105. doi: 10.1063/1.4999375.

Kissinger, H. E. (1956) 'Reaction Kinetics in Differential Thermal Analysis', *Helv. Chim. Acta*, 28(5), p. 73. Available at: https://pubs.acs.org/sharingguidelines (Accessed: 31 October 2021).

Kubel, F. and Schmid, H. (1990) 'Structure of a ferroelectric and ferroelastic monodomain crystal of the perovskite $BiFeO_3$', *urn:issn:0108-7681*, 46(6), pp. 698–702. doi: 10.1107/s0108768190006887.

Kumar, M. M., Srinivas, A. and Suryanarayana, S. V. (1999) 'Structure property relations in $BiFeO_3/BaTiO_3$ solid solutions', *Journal of Applied Physics*, 87(2), p. 855. doi: 10.1063/1.371953.

Kuscer, D., Holc, J. and Kosec, M. (2007) 'Formation of $0.65Pb(Mg_{1/3}Nb_{2/3})O_3–0.35PbTiO_3$ Using a High-Energy Milling Process', *Journal of the American Ceramic Society*, 90(1), pp. 29–35. doi: 10.1111/j.1551-2916.2006.01332.x.

Lee, M. H. *et al.* (2018) 'Low sintering temperature for lead-free $BiFeO_3$-$BaTiO_3$ ceramics with high piezoelectric performance', *Journal of the American Ceramic Society*, 102(5), p. jace.16126. doi: 10.1111/jace.16126.

Leontsev, S. O. and Eitel, R. E. (2009) 'Dielectric and Piezoelectric Properties in Mn-Modified $(1−x)BiFeO_3–xBaTiO_3$ Ceramics', *Journal of the American Ceramic Society*, 92(12), pp. 2957–2961. doi: 10.1111/j.1551-2916.2009.03313.x.

Levin, I., Krayzman, V. and Woicik, J. C. (2013) 'Local-structure origins of the sustained Curie temperature in $(Ba,Ca)TiO_3$ ferroelectrics', *Applied Physics Letters*, 102(16), p. 162906. doi: 10.1063/1.4802996.

Li, C., Zheng, T. and Wu, J. (2021) 'Competitive mechanism of temperature-dependent electrical properties in $BiFeO_3$-$BaTiO_3$ ferroelectrics controlled by domain evolution', *Acta Materialia*, 206, p. 116601. doi: 10.1016/j.actamat.2020.116601.

Li, J. *et al.* (2019) 'Nanoscale stacking fault–assisted room temperature plasticity in flash-sintered TiO_2', *Science Advances*, 5(9), p. 5519. doi: 10.1126/sciadv.aaw5519.

Li, Q. *et al.* (2017) 'Remarkable piezoelectricity and stable high-temperature dielectric properties of quenched $BiFeO_3$-$BaTiO_3$ ceramics', *Journal of the American Ceramic Society*, 100(12), pp. 5573–5583. doi: 10.1111/jace.15079.

Li, Q., Cheng, J. and Chen, J. (2017) 'Reduced dielectric loss and enhanced piezoelectric properties of Mn modified $0.71BiFeO_3$-$0.29BaTiO_3$ ceramics sintered under oxygen atmosphere', *Journal of Materials Science: Materials in Electronics*, 28. doi: 10.1007/s10854-016-5670-3.

Liu, N. *et al.* (2018) 'Colossal negative electrocaloric effects in lead-free bismuth ferrite-based bulk ferroelectric perovskite for solid-state refrigeration', *Journal of Materials Chemistry C*, 6(39), pp. 10415–10421. doi: 10.1039/c8tc04125c.

Liu, W. and Ren, X. (2009) 'Large Piezoelectric Effect in Pb-Free Ceramics', *Physical Review Letters*, 103(25), p. 257602. doi: 10.1103/PhysRevLett.103.257602.

Louaer, A. *et al.* (2019) 'Crystallization kinetics and growth mechanism of $0.5(Ba_{0.85}Ca_{0.15})TiO_3{-}0.5Ba(Zr_{0.1}Ti_{0.9})O_3$ powders prepared via solid-state reaction', 93(1), pp. 116–133. doi: 10.1080/01411594.2019.1692014.

Macdonald, J. R. (1992) 'Impedance Spectroscopy', *Annals of Biomedical Engineering*, 20, pp. 289–305. doi: https://doi.org/10.1007/bf02368532.

Manavalan, S. (2005) 'Structural and Electrical Properties of Barium Strontium Titanate Thin Films for Tunable Microwave Applications', *Graduate Theses and Dissertations*. Available at: https://digitalcommons.usf.edu/etd/756 (Accessed: 4 January 2022).

Marcelli, A. *et al.* (2012) 'Biological applications of synchrotron radiation infrared spectromicroscopy', *Biotechnology Advances*, 30(6), pp. 1390–1404. doi: 10.1016/j.biotechadv.2012.02.012.

Mazon, T. *et al.* (2005) 'Structural and dielectric properties of Nd^{3+}-doped $Ba_{0.77}Ca_{0.23}TiO_3$ ceramics', *Journal of Applied Physics*, 97(10), p. 104113. doi: 10.1063/1.1901834.

Mitsui, T. and Westphal, W. B. (1961) 'Dielectric and X-Ray Studies of <span class', *Physical Review*, 124(5), p. 1354. doi: 10.1103/PhysRev.124.1354.

Moghtada, A., Moghadam, A. H. and Ashiri, R. (2018) 'Tetragonality enhancement in $BaTiO_3$ by mechanical activation of the starting $BaCO_3$ and TiO_2 powders: Characterization of the contribution of the mechanical activation and postmilling calcination phenomena', *International Journal of Applied Ceramic Technology*, 15(6), pp. 1518–1531. doi: 10.1111/ijac.13019.

Mohamed, M. *et al.* (2018) 'Examination of the kinetic reaction mechanisms of amorphous $As_{50}Se_{50}$ chalcogenide glass', *Applied Physics A: Materials Science and Processing*, 124(8), pp. 1–9. doi: 10.1007/S00339-018-1976-8.

Moreau, J. M. *et al.* (1971) 'Ferroelectric $BiFeO_3$ X-ray and neutron diffraction study', *Journal of Physics and Chemistry of Solids*, 32(6), pp. 1315–1320. doi: 10.1016/S0022-3697(71)80189-0.

Motta, F. V. *et al.* (2010) 'Room temperature photoluminescence of BCT prepared by Complex Polymerization Method', *Current Applied Physics*, 10(1), pp. 16–20. doi: 10.1016/j.cap.2009.04.005.

Murakami, S. *et al.* (2018) 'Optimising dopants and properties in $BiMeO_3$ (Me = Al, Ga, Sc, Y, $Mg_{2/3}Nb_{1/3}$, $Zn_{2/3}Nb_{1/3}$, $Zn_{1/2}Ti_{1/2}$) lead-free $BaTiO_3$-$BiFeO_3$ based ceramics for actuator applications', *Journal of the European Ceramic Society*, 38(12), pp. 4220–4231. doi: 10.1016/j.jeurceramsoc.2018.05.019.

Orava, J. *et al.* (2012) 'Characterization of supercooled liquid $Ge_2Sb_2Te_5$ and its crystallization by ultrafast-heating calorimetry', *Nature Materials 2012 11:4*, 11(4), pp. 279–283. doi: 10.1038/nmat3275.

Orrù, R. *et al.* (2009) 'Consolidation/synthesis of materials by electric current activated/assisted sintering', *Materials Science and Engineering: R: Reports*, 63(4–6), pp. 127–287. doi: 10.1016/j.mser.2008.09.003.

OzawaTakeo (2006) 'A New Method of Analyzing Thermogravimetric Data', *http://dx.doi.org/10.1246/bcsj.38.1881*, 38(11), pp. 1881–1886. doi: 10.1246/bcsj.38.1881.

Pabst, G. W. *et al.* (2007) 'Leakage mechanisms in $BiFeO_3$ thin films', *Applied Physics Letters*, 90(7), p. 072902. doi: 10.1063/1.2535663.

Pakalniškis, A. *et al.* (2020) 'Nanoscale ferroelectricity in pseudo-cubic sol-gel derived barium titanate - bismuth ferrite ($BaTiO_3$–$BiFeO_3$) solid solutions', *Journal of Alloys and Compounds*, 830, p. 154632. doi: 10.1016/j.jallcom.2020.154632.

Palai, R. *et al.* (2008) 'β phase and γ-β metal-insulator transition in multiferroic $BiFeO_3$', *Physical Review B - Condensed Matter and Materials Physics*, 77(1), p. 014110. doi: 10.1103/physrevb.77.014110.

Palewicz, A. *et al.* (2007) 'Atomic displacements in $BiFeO_3$ as a function of temperature: Neutron diffraction study', *Acta Crystallographica Section B: Structural Science*, 63(4), pp. 537–544. doi: 10.1107/s0108768107023956/ck5024sup2.

Panda, P. K. and Sahoo, B. (2015) 'PZT to Lead Free Piezo Ceramics: A Review', 474(1), pp. 128–143. doi: 10.1080/00150193.2015.997146.

Panigrahi, M. R. and Panigrahi, S. (2010) 'Diffuse phase transition and dielectric study in $Ba_{0.95}Ca_{0.05}TiO_3$ ceramic', *Physica B: Condensed Matter*, 405(11), pp. 2556–2559. doi: 10.1016/j.physb.2010.03.031.

Pérez-Maqueda, L. A., *et al.* (2002) 'Advantages of Combined Kinetic Analysis of Experimental Data Obtained under Any Heating Profile', *Journal of Physical Chemistry A*, 106(12), pp. 2862–2868. doi: 10.1021/jp012246b.

Pérez-Maqueda, L. A., J. M. Criado, and and Sánchez-Jiménez, P. E. (2006) 'Combined Kinetic Analysis of Solid-State Reactions: A Powerful Tool for the Simultaneous Determination of Kinetic Parameters and the Kinetic Model without Previous Assumptions on the Reaction Mechanism', *Journal of Physical Chemistry A*, 110(45), pp. 12456–12462. doi: 10.1021/JP064792G.

Pérez-Maqueda, L. A. *et al.* (2017) 'Flash sintering of highly insulating nanostructured phase-pure $BiFeO_3$', *Journal of the American Ceramic Society*, 100(8), pp. 3365–3369. doi: 10.1111/jace.14990.

Pérez-Maqueda, L. A. *et al.* (2019) 'Insight into the $BiFeO_3$ flash sintering process by in-situ energy dispersive X-ray diffraction (ED-XRD)', *Ceramics International*, 45(2), pp. 2828–2834. doi: 10.1016/j.ceramint.2018.07.293.

Pérez-Maqueda, L. A., Criado, J. M. and Málek, J. (2003) 'Combined kinetic analysis for crystallization kinetics of non-crystalline solids', *Journal of Non-Crystalline Solids*, 320(1–3), pp. 84–91. doi: 10.1016/S0022-3093(03)00023-1.

Phuah, X. L. *et al.* (2021) 'Defects in flash-sintered ceramics and their effects on mechanical properties', *MRS Bulletin*, 46(1), pp. 44–51. doi: 10.1557/s43577-020-00014-y.

Prasad, N. S. and Varma, K. B. R. (2005) 'Crystallization Kinetics of the $LiBO_2$–Nb_2O_5 Glass Using Differential Thermal Analysis', *Journal of the American Ceramic Society*, 88(2), pp. 357–361. doi: 10.1111/j.1551-2916.2005.00055.x.

Prette, A. L. G. *et al.* (2011) 'Flash-sintering of Co_2MnO_4 spinel for solid oxide fuel cell applications', *Journal of Power Sources*, 196(4), pp. 2061–2065. doi: 10.1016/j.jpowsour.2010.10.036.

Puli, V. S. *et al.* (2014) 'Investigations on structure, ferroelectric, piezoelectric and energy storage properties of barium calcium titanate (BCT) ceramics', *Journal of Alloys and Compounds*, 584, pp. 369–373. doi: 10.1016/j.jallcom.2013.09.108.

Qi, H. *et al.* (2020) 'Superior Energy-Storage Capacitors with Simultaneously Giant Energy Density and Efficiency Using Nanodomain Engineered $BiFeO_3$-$BaTiO_3$-$NaNbO_3$ Lead-Free Bulk Ferroelectrics', *Advanced Energy Materials*, 10(6), p. 1903338. doi: 10.1002/aenm.201903338.

Qin, W. *et al.* (2016) 'Electrode Effects on Microstructure Formation During Flash Sintering of Yttrium-Stabilized Zirconia', *Journal of the American Ceramic Society*, 99(7), pp. 2253–2259. doi: 10.1111/jace.14234.

Rabe, K. M. *et al.* (2007) 'Modern Physics of Ferroelectrics: Essential Background', *Topics in Applied Physics*, 105, pp. 1–30. doi: 10.1007/978-3-540-34591-6_1.

Rached, A. *et al.* (2021) 'Structural, optical and electrical properties of barium titanate', *Materials Chemistry and Physics*, 267, p. 124600. doi: 10.1016/j.matchemphys.2021.124600.

Raj, R. (2012) 'Joule heating during flash-sintering', *Journal of the European Ceramic Society*, 32(10), pp. 2293–2301. doi: 10.1016/j.jeurceramsoc.2012.02.030.

Raj, R. *et al.* (2021) 'Flash sintering: A new frontier in defect physics and materials science', *MRS Bulletin*, 46(1), pp. 36–43. doi: 10.1557/s43577-020-00011-1.

Randall M. G. (1996) 'Novel Sintering Techniques', *Sintering Theory and Practice*, pp. 373–420. Available at: https://www.wiley.com/en-us/Sintering+Theory+and+Practice-p-9780471057864 (Accessed: 4 January 2022).

Rashwan, G. M. *et al.* (2021) 'Preparation and Characterization and Dielectric Properties of $(Ba_{0.95}Ca_{0.05})TiO_3$ Ceramic Material', *International Journal of Thin Film Science and Technology*, 10(3). Available at: https://digitalcommons.aaru.edu.jo/ijtfst/vol10/iss3/1 (Accessed: 20 November 2021).

Ren, K., Liu, J. and Wang, Y. (2020) 'Flash sintering of yttria-stabilized zirconia: Fundamental understanding and applications', *Scripta Materialia*, 187, pp. 371–378. doi: 10.1016/j.scriptamat.2020.06.040.

Rosenberger, A., Brennan, R. E. and Fry, A. L. (2021) 'Flash sintering feasibility study and localized densification in boron carbide', *Journal of the American Ceramic Society*, 104(8), pp. 3823–3827. doi: 10.1111/jace.17833.

Sahoo, S. *et al.* (2019) 'Enhancement of dielectric and ferroelectric properties by Ca doping $BaTiO_3$', *AIP Conference Proceedings*, 2115(1), p. 030020. doi: 10.1063/1.5112859.

Sánchez-Jiménez, P. E. *et al.* (2009) 'Combined kinetic analysis of thermal degradation of polymeric materials under any thermal pathway', *Polymer Degradation and Stability*, 94(11), pp. 2079–2085. doi: 10.1016/j.polymdegradstab.2009.07.006.

Sánchez-Jiménez, P. E. *et al.* (2010) 'Generalized Kinetic Master Plots for the Thermal Degradation of Polymers Following a Random Scission Mechanism', *Journal of Physical Chemistry A*, 114(30), pp. 7868–7876. doi: 10.1021/jp103171h.

Sánchez-Jiménez, P. E. *et al.* (2013) 'Generalized master plots as a straightforward approach for determining the kinetic model: The case of cellulose pyrolysis', *Thermochimica Acta*, 552, pp. 54–59. doi: 10.1016/j.tca.2012.11.003.

Schmerbauch, C. *et al.* (2014) 'Flash Sintering of Nanocrystalline Zinc Oxide and its Influence on Microstructure and Defect Formation', *Journal of the American Ceramic Society*, 97(6), pp. 1728–1735. doi: 10.1111/jace.12972.

Schmidt, R. (2007) 'Impedance Spectroscopy of Electroceramics Multiferroic materials View project Materials for energy storage and conversion View project Impedance Spectroscopy of Electroceramics', *Ceramic Materials Research Trends*, pp. 321–351. Available at: https://www.researchgate.net/publication/229484033 (Accessed: 14 December 2021).

Schultheiß, J. *et al.* (2017) 'Effect of degree of crystallographic texture on ferro- and piezoelectric properties of $Ba_{0.85}Ca_{0.15}TiO_3$ piezoceramics', *Journal of the American Ceramic Society*, 100(5), pp. 2098–2107. doi: 10.1111/jace.14749.

Searcy, A. W. (1985) 'Driving Force for Sintering of Particles with Anisotropic Surface Energies', *Journal of the American Ceramic Society*, 68(10), pp. C–267. doi: 10.1111/j.1151-2916.1985.tb11526.x.

Shankar, S. *et al.* (2020) 'Dielectric and tunable ferroelectric properties in $BiFeO_3$–$BiCoO_3$–$BaTiO_3$ ternary compound', *Applied Physics A: Materials Science and Processing*, 126(9), p. 686. doi: 10.1007/s00339-020-03872-0.

Shao, S. *et al.* (2003) 'High piezoelectric properties and domain configuration in $BaTiO_3$ ceramics obtained through the solid-state reaction route', *Journal of Physics D: Applied Physics*, 41(12), p. 125408. doi: 10.1088/0022-3727/41/12/125408.

Shi, J. L. (1999) 'Thermodynamics and Densification Kinetics in Solid-state Sintering of Ceramics', *Journal of Materials Research*, 14(4), pp. 1398–1408. doi: 10.1557/jmr.1999.0190.

Shi, R., Pu, Y., Wang, W., *et al.* (2019) 'Flash sintering of barium titanate', *Ceramics International*, 45(6), pp. 7085–7089. doi: 10.1016/j.ceramint.2018.12.211.

Shi, R., Pu, Y., Li, J., *et al.* (2019) 'Particle transport mode during flash sintering of sodium bismuth titanate ceramic', *Ceramics International*, 45(10), pp. 13269–13274. doi: 10.1016/j.ceramint.2019.04.015.

Shomrat, N. *et al.* (2015) 'Flash sintering of potassium-niobate', *Journal of the European Ceramic Society*, 35(7), pp. 2209–2213. doi: 10.1016/j.jeurceramsoc.2015.01.017.

Shu, C. (2018) *Investigation of the structural and functional properties of lead-free barium calcium zirconate titanate piezoceramics*. University of Birmingham. Available at: http://etheses.bham.ac.uk/id/eprint/8148 (Accessed: 23 October 2021).

Shu, C., Reed, D. and Button, T. (2015) 'Mechanism of Ca-Ba diffusion in lead-free (Ba,Ca)TiO_3 piezoelectrics', *MRS Online Proceedings Library (OPL)*, 1782, pp. 23–28. doi: 10.1557/olp.2015.668.

Shu, C., Reed, D. and Button, T. W. (2018) 'A phase diagram of $Ba_{1-x}Ca_xTiO_3$ (x = 0-0.30) piezoceramics by Raman spectroscopy', *Journal of the American Ceramic Society*, 101(6), pp. 2589–2593. doi: 10.1111/jace.15415.

Sinclair, D. C. and West, A. R. (1998) 'Impedance and modulus spectroscopy of semiconducting $BaTiO_3$ showing positive temperature coefficient of resistance', *Journal of Applied Physics*, 66(8), p. 3850. doi: 10.1063/1.344049.

Singh, A., Kumar, A. and Pandey, D. (2018) 'Effect of synthesis route on structure and dielectric properties of (1-x)$BiFeO_3$-x$BaTiO_3$ solid solutions and its phase diagram', *Journal of Applied Physics*, 124(22), p. 224101. doi: 10.1063/1.5043164.

Srihari, N. V., Vinayakumar, K. B. and Nagaraja, K. K. (2020) 'Magnetoelectric Coupling in Bismuth Ferrite—Challenges and Perspectives', *Coatings 2020, Vol. 10, Page 1221*, 10(12), p. 1221. doi: 10.3390/coatings10121221.

Stojanovic, B. D. *et al.* (2005) 'Mechanochemical synthesis of barium titanate', *Journal of the European Ceramic Society*, 25(12), pp. 1985–1989. doi: 10.1016/j.jeurceramsoc.2005.03.003.

Taghaddos, E. *et al.* (2019) 'Electromechanical properties of flash sintered BNT-based piezoelectric ceramic', *Journal of the European Ceramic Society*, 39(9), pp. 2882–2888. doi: 10.1016/j.jeurceramsoc.2019.03.050.

Taibi, A. *et al.* (2019) 'Barium calcium titanate solid solution: Non-isothermal kinetic analysis of Ca^{2+} incorporation into $BaTiO_3$', *Thermochimica Acta*, 680, p. 178356. doi: 10.1016/j.tca.2019.178356.

Templeton, L. K. and Pask, J. A. (1959) 'Formation of $BaTiO_3$ from $BaCO_3$ and TiO_2 in Air and in CO_2', *Journal of the American Ceramic Society*, 42(5), pp. 212–216. doi: 10.1111/j.1151-2916.1959.tb15455.x.

Tiwari, B., Babu, T. and Choudhary, R. N. P. (2021) 'Piezoelectric lead zirconate titanate as an energy material: A review study', *Materials Today: Proceedings*, 43, pp. 407–412. doi: 10.1016/j.matpr.2020.11.692.

Tong, K. *et al.* (2018) 'Enhanced piezoelectric response and high-temperature sensitivity by site-selected doping of $BiFeO_3$-$BaTiO_3$ ceramics', *Journal of the European Ceramic Society*, 38(4), pp. 1356–1366. doi: 10.1016/j.jeurceramsoc.2017.10.023.

Uchino, K. and Nomura, S. (2011) 'Critical exponents of the dielectric constants in diffused-phase-transition crystals', 44(1), pp. 55–61. doi: 10.1080/00150198208260644.

Varatharajan, R. *et al.* (2000) 'Ferroelectric characterization studies on barium calcium titanate single crystals', *Materials Characterization*, 45(2), pp. 89–93. doi: 10.1016/S1044-5803(00)00053-x.

Vendrell, X. *et al.* (2019) 'Influence of flash sintering on the ionic conductivity of 8 mol% yttria stabilized zirconia', *Journal of the European Ceramic Society*, 39(4), pp. 1352–1358. doi: 10.1016/j.jeurceramsoc.2018.12.048.

Vlaev, L. T., Nikolova, M. M. and Gospodinov, G. G. (2004) 'Non-isothermal kinetics of dehydration of some selenite hexahydrates', *Journal of Solid State Chemistry*, 177(8), pp. 2663–2669. doi: 10.1016/j.jssc.2004.04.036.

Vyazovkin, S. *et al.* (2011) 'ICTAC Kinetics Committee recommendations for performing kinetic computations on thermal analysis data', *Thermochimica Acta*, 520(1–2), pp. 1–19. doi: 10.1016/j.tca.2011.03.034.

Vyazovkin, S. (2015) 'Some Basics En Route to Isoconversional Methodology', *Isoconversional Kinetics of Thermally Stimulated Processes*, pp. 1–25. doi: 10.1007/978-3-319-14175-6_1.

Vyazovkin, S. and Sbirrazzuoli, N. (2006) 'Isoconversional Kinetic Analysis of Thermally Stimulated Processes in Polymers', *Macromolecular Rapid Communications*, 27(18), pp. 1515–1532. doi: 10.1002/marc.200600404.

Wada, S. *et al.* (2004) 'Anomalous Structure and Dielectric Properties of $BaTiO_3$–$CaTiO_3$ System Ceramics Composites', *Journal of the Ceramic Society of Japan*.

Wang, D., Wang, G., *et al.* (2018) '$BiFeO_3$-$BaTiO_3$: A new generation of lead-free electroceramics', *Journal of Advanced Dielectrics*, 8(6). doi: 10.1142/s2010135x18300049.

Wang, D., Fan, Z., *et al.* (2018) 'High Energy Storage Density and Large Strain in $Bi(Zn_{2/3}Nb_{1/3})O_3$-Doped $BiFeO_3$-$BaTiO_3$ Ceramics', *ACS Applied Energy Materials*, 1(8), pp. 4403–4412. doi: 10.1021/acsaem.8b01099.

Wang, G. *et al.* (2019) 'Ultrahigh energy storage density lead-free multilayers by controlled electrical homogeneity', *Energy and Environmental Science*, 12(2), pp. 582–588. doi: 10.1039/c8ee03287d.

Wang, J. *et al.* (2000) 'Mechanically Activating Nucleation and Growth of Complex Perovskites', *Journal of Solid State Chemistry*, 154(2), pp. 321–328. doi: 10.1006/jssc.2000.8782.

Wang, J. *et al.* (2003) 'Epitaxial $BiFeO_3$ multiferroic thin film heterostructures', *Science*, 299(5613), pp. 1719–1722. doi: 10.1126/science.1080615.

Wang, L. *et al.* (2019) 'High electrostrain with high Curie temperature in $BiFeO_3$-$BaTiO_3$-based ceramics', *Scripta Materialia*, 164, pp. 62–65. doi: 10.1016/j.scriptamat.2019.01.028.

Wang, X. *et al.* (2019) 'Flash sintering of ZnO ceramics at 50 °C under an AC field', *Ceramics International*, 45(18), pp. 24909–24913. doi: 10.1016/j.ceramint.2019.08.142.

Wang, Z. *et al.* (2022) 'Excellent thermal stability and enhanced piezoelectric performance of $Bi(Ni_{2/3}Nb_{1/3})O_3$-modified $BiFeO_3$–$BaTiO_3$ ceramics', *Journal of the American Ceramic Society*, 105(1), pp. 317–326. doi: 10.1111/jace.18049.

Wassel, M. A. B. *et al.* (2019) 'Anisotropic lattice expansion determined during flash sintering of $BiFeO_3$ by in-situ energy-dispersive X-ray diffraction', *Scripta Materialia*, 162, pp. 286–291. doi: 10.1016/j.scriptamat.2018.11.028.

Wei, Y. *et al.* (2013) 'Dielectric, Ferroelectric, and Piezoelectric Properties of $BiFeO_3$–$BaTiO_3$ Ceramics', *Journal of the American Ceramic Society*, 96(10), pp. 3163–3168. doi: 10.1111/jace.12475.

Winseck, M. *et al.* (2016) 'Crystallization kinetics of the phase change material $GeSb_6Te$ measured with dynamic transmission electron microscopy', *Dalton Transactions*, 45(24), pp. 9988–9995. doi: 10.1039/c6dt00298f.

Wu, J. *et al.* (2016) 'Multiferroic bismuth ferrite-based materials for multifunctional applications: Ceramic bulks, thin films and nanostructures', *Progress in Materials Science*, 84, pp. 335–402. doi: 10.1016/j.pmatsci.2016.09.001.

Wu, J. (2020) 'Perovskite lead-free piezoelectric ceramics', *Journal of Applied Physics*, 127(19), p. 190901. doi: 10.1063/5.0006261.

Wu, Y. *et al.* (2020) 'Dense $Na_{0.5}K_{0.5}NbO_3$ ceramics produced by reactive flash sintering of $NaNbO_3$-$KNbO_3$ mixed powders', *Scripta Materialia*, 174, pp. 49–52. doi: 10.1016/j.scriptamat.2019.08.035.

Xun, B. *et al.* (2021) 'Lead-Free $BiFeO_3$-$BaTiO_3$ Ceramics with High Curie Temperature: Fine Compositional Tuning across the Phase Boundary for High Piezoelectric Charge and Strain Coefficients', *ACS Applied Materials and Interfaces*, 13(3), pp. 4192–4202. doi: 10.1021/acsami.0c20381.

Yadav, D. and Raj, R. (2017) 'The onset of the flash transition in single crystals of cubic zirconia as a function of electric field and temperature', *Scripta Materialia*, 134, pp. 123–127. doi: 10.1016/j.scriptamat.2017.02.015.

Yang, B. *et al.* (2022) 'Effects of incubation on microstructure gradient in flash-sintered TiO_2', *Scripta Materialia*, 207, p. 114270. doi: 10.1016/j.scriptamat.2021.114270.

Yang, H. *et al.* (2013) 'Piezoelectric properties and temperature stabilities of Mn- and Cu-modified $BiFeO_3$-$BaTiO_3$ high temperature ceramics', *Journal of the European Ceramic Society*, 33(6), pp. 1177–1183. doi: 10.1016/j.jeurceramsoc.2012.11.019.

Yin, Y. *et al.* (2021) 'Relaxor behaviors enhance piezoelectricity in lead-free $BiFeO_3$-$BaTiO_3$ ceramics incorporated with a tiny amount of $Bi(Mg_{1/2}Ti_{1/2})O_3$ near the morphotropic phase boundary', *Ceramics International*, 47(7), pp. 9486–9494. doi: 10.1016/j.ceramint.2020.12.082.

Yoon, B., Yadav, D., Raj, R., *et al.* (2018) 'Measurement of O and Ti atom displacements in TiO_2 during flash sintering experiments', *Journal of the American Ceramic Society*, 101(5), pp. 1811–1817. doi: 10.1111/jace.15375.

Yoon, B., Yadav, D., Ghose, S., *et al.* (2018) 'Reactive flash sintering: MgO and α-Al_2O_3 transform and sinter into single-phase polycrystals of $MgAl_2O_4$', *Journal of the American Ceramic Society*, 102(5), p. jace.15974. doi: 10.1111/jace.15974.

Yoon, B. *et al.* (2019) 'Reactive flash sintering: MgO and α-Al_2O_3 transform and sinter into single-phase polycrystals of $MgAl_2O_4$', *Journal of the American Ceramic Society*, 102(5), pp. 2294–2303. doi: 10.1111/jace.15974.

Yoon, B. *et al.* (2020) 'Reactive flash sintering of the entropy-stabilized oxide $Mg_{0.2}Ni_{0.2}Co_{0.2}Cu_{0.2}Zn_{0.2}O$', *Scripta Materialia*, 181, pp. 48–52. doi: 10.1016/j.scriptamat.2020.02.006.

Yoon, D.-H. and BurtrandI.Lee (2002) '$BaTiO_3$ properties and powder characteristics for ceramic capacitors', *Journal of Ceramic Processing Research*, 3(2), pp. 41–47.

Yun, S., Wang, X., Shi, J., *et al.* (2009) 'Aging-induced double hysteresis loops in bismuth-doped (Ba,Ca)TiO_3 ferroelectric ceramics', *Journal of Materials Research 2009 24:10*, 24(10), pp. 3073–3077. doi: 10.1557/jmr.2009.0375.

Yun, S., Wang, X., Li, J., *et al.* (2009) 'Investigation of dielectric relaxation mechanism in bismuth doped barium calcium titanate ceramics by dielectric and Raman spectroscopy', *Materials Chemistry and Physics*, 116(2–3), pp. 339–343. doi: 10.1016/j.matchemphys.2009.02.057.

Zapata-Solvas, E. *et al.* (2013) 'Preliminary investigation of flash sintering of SiC', *Journal of the European Ceramic Society*, 33(13–14), pp. 2811–2816. doi: 10.1016/j.jeurceramsoc.2013.04.023.

Zeb, A. and Milne, S. J. (2013) 'Stability of high-temperature dielectric properties for (1-x)$Ba_{0.8}Ca_{0.2}TiO_3$-x$Bi(Mg_{0.5}Ti_{0.5})O_3$ ceramics', *Journal of the American Ceramic Society*, 96(9), pp. 2887–2892. doi: 10.1111/jace.12412.

Zhang, H. *et al.* (2014) 'Compositional dependence of dielectric and ferroelectric properties in $BiFeO_3$-$BaTiO_3$ solid solutions', *Ceramics International*, 40(3), pp. 4759–4765. doi: 10.1016/j.ceramint.2013.09.020.

Zhang, Y. *et al.* (2014) 'Correlation Between Piezoelectric Properties and Phase Coexistence in (Ba,Ca)(Ti,Zr)O_3 Ceramics', *Journal of the American Ceramic Society*, 97(9), pp. 2885–2891. doi: 10.1111/jace.13047.

Zhang, Y., Nie, J. and Luo, J. (2016) 'Effects of phase and doping on flash sintering of TiO_2', *Journal of the Ceramic Society of Japan*, 124(4), pp. 296–300. doi: 10.2109/jcersj2.15255.

Zheng, Q. *et al.* (2014) 'Enhanced ferroelectricity, piezoelectricity, and ferromagnetism in Nd-modified $BiFeO_3$-$BaTiO_3$ lead-free ceramics', *Journal of Applied Physics*, 116(18), p. 184101. doi: 10.1063/1.4901198.

Zhou, C. *et al.* (2012) 'Remarkably high-temperature stable piezoelectric properties of $Bi(Mg_{0.5}Ti_{0.5})O_3$ modified $BiFeO_3$–$BaTiO_3$ ceramics', *Applied Physics Letters*, 101(3), p. 032901. doi: 10.1063/1.4736724.

Zhou, H. *et al.* (2017) 'Giant In^{3+} doping-induced enhancement of the upconversion luminescence of $Ba_{0.85}Ca_{0.15}TiO_3$:Er^{3+}/Yb^{3+} lead-free ferroelectric ceramics', *Materials Letters*, 188, pp. 364–367. doi: 10.1016/j.matlet.2016.11.108.

Zhou, H., Li, X., Huang, R., *et al.* (2021) 'Effect of atmospheric conditions on the onset electric field of ZnO and Y_2O_3 ceramics flash sintering at room temperature', *Ceramics International*, 47(24), pp. 34068–34071. doi: 10.1016/j.ceramint.2021.08.316.

Zhou, H., Li, X., Zhu, Y., *et al.* (2021) 'Review of flash sintering with strong electric field', *High Voltage*. doi: 10.1049/hve2.12080.

Zhu, X. N., Zhang, W. and Chen, X. M. (2013) 'Enhanced dielectric and ferroelectric characteristics in Ca-modified $BaTiO_3$ ceramics', *AIP Advances*, 3(8), p. 082125. doi: 10.1063/1.4819482.

Zhu, Y. *et al.* (2021) 'Electric field-assisted solid-state reaction of $BaCO_3$-TiO_2 system', *Journal of the American Ceramic Society*, 104(12), pp. 6572–6578. doi: 10.1111/jace.18027.